

Dynamic Load Analysis and Optimization of Connecting Rod

This study investigates and compares fatigue behavior of forged steel and powder metal connecting rods and weight and cost reduction opportunities for a production forged steel connecting rod



**American
Iron and Steel
Institute**

A Thesis

entitled

Dynamic Load Analysis and Optimization of Connecting Rod

by

Pravardhan S. Shenoy

Submitted as partial fulfillment of the requirements for

the Master of Science Degree in

Mechanical Engineering

Adviser: Dr. Ali Fatemi

Graduate School

The University of Toledo

May 2004

The University of Toledo

College of Engineering

I HEREBY RECOMMEND THAT THE THESIS PREPARED UNDER MY
SUPERVISION BY Pravaradhan S. Shenoy

ENTITLED Dynamic Load Analysis and Optimization of Connecting Rod

BE ACCEPTED IN PARTIAL FULFILLMENT OF THE REQUIREMENTS FOR THE
DEGREE OF Master of Science in Mechanical Engineering

Thesis Adviser: Dr. Ali Fatemi

Recommendation concurred by:

Dr. Mehdi Pourazady

Committee

on

Dr. Hongyan Zhang

Final Examination

Dean, College of Engineering

ABSTRACT
OF
Dynamic Load Analysis and Optimization of Connecting Rod

Pravardhan S. Shenoy

Submitted as partial fulfillment of the requirements for
the Master of Science Degree in
Mechanical Engineering

The University of Toledo

May 2004

The main objective of this study was to explore weight and cost reduction opportunities for a production forged steel connecting rod. This has entailed performing a detailed load analysis. Therefore, this study has dealt with two subjects, first, dynamic load and quasi-dynamic stress analysis of the connecting rod, and second, optimization for weight and cost.

In the first part of the study, the loads acting on the connecting rod as a function of time were obtained. The relations for obtaining the loads and accelerations for the connecting rod at a given constant speed of the crankshaft were also determined. Quasi-dynamic finite element analysis was performed at several crank angles. The stress-time history for a few locations was obtained. The difference between the static FEA, quasi-dynamic FEA was studied. Based on the observations of the quasi-dynamic FEA, static

FEA and the load analysis results, the load for the optimization study was selected. The results were also used to determine the variation of R-ratio, degree of stress multiaxiality, and the fatigue model to be used for analyzing the fatigue strength. The component was optimized for weight and cost subject to fatigue life and space constraints and manufacturability.

It is the conclusion of this study that the connecting rod can be designed and optimized under a load range comprising tensile load corresponding to 360° crank angle at the maximum engine speed as one extreme load, and compressive load corresponding to the peak gas pressure as the other extreme load. Furthermore, the existing connecting rod can be replaced with a new connecting rod made of C-70 steel that is 10% lighter and 25% less expensive due to the steel's fracture crackability. The fracture crackability feature, facilitates separation of cap from rod without additional machining of the mating surfaces. Yet, the same performance can be expected in terms of component durability.

ACKNOWLEDGEMENTS

I would like to thank my parents (Subhash and Somi), sister (Tejaswini), aunt (Lata) and uncle (Ranganath) for prodding / supporting / inspiring me to pursue higher education that eventually led me to fly across the globe for pursuing this Master's program.

I sincerely appreciate Dr. Ali Fatemi for accepting me as his student and for giving me the opportunity to work on this program. I am also grateful for his support and guidance that have helped me expand my horizons of thought and expression. Dr. Mehdi Pourazady was very helpful in finding solutions to several problems I had during the course of this program. I am grateful to him for his time and patience.

I would like to thank Randy Weiland and John Kessler for providing me with the technical information required for this program. This research program was funded by AISI (American Iron and Steel Institute) and David Anderson played a leading role in facilitating this research.

Thanks to Tom Elmer (MAHLE Engine Components) and Berthold Repgen for helping us find answers to manufacturing and cost issues of the connecting rod related to this program.

I would also like to thank Dr. Masiulaniec Cyril, Russel Chernenkoff and my lab mates Mehrdad Zoroufi, Fengjie Yin, Hui Zhang, Li Bing, and Atousa Plaseied for their helpful discussion relating to various aspects of this work.

TABLE OF CONTENTS

ABSTRACT	ii
ACKNOWLEDGEMENTS	iv
TABLE OF CONTENTS	v
LIST OF TABLES	viii
LIST OF FIGURES	x
NOMENCLATURE	xx
1. INTRODUCTION	1
1.1 BACKGROUND	1
1.2 LITERATURE REVIEW	2
1.3 OBJECTIVES AND OUTLINE	9
2. DYNAMIC LOAD ANALYSIS OF THE CONNECTING ROD	16
2.1 ANALYTICAL VECTOR APPROACH.....	17
2.2 VERIFICATION OF ANALYTICAL APPROACH.....	19
2.3 DYNAMIC ANALYSIS FOR THE ACTUAL CONNECTING ROD.....	21
2.4 FEA WITH DYNAMIC LOADS.....	23
3. FE MODELING OF THE CONNECTING ROD	43
3.1 GEOMETRY OF THE CONNECTING ROD.....	43
3.2 MESH GENERATION.....	44
3.3 BOUNDARY CONDITIONS.....	46

3.3.1	<i>Loading</i>	46
3.3.2	<i>Restraints</i>	51
3.4	VALIDATION OF FEA MODELS	53
4.	RESULTS OF FINITE ELEMENT STRESS ANALYSIS	69
4.1	QUASI-DYNAMIC STRESS ANALYSIS	70
4.2	STATIC AXIAL STRESS ANALYSIS	78
4.3	COMPARISON OF STATIC AND QUASI-DYNAMIC FEA RESULTS	80
4.4	OPTIMIZATION POTENTIAL	84
5.	OPTIMIZATION	103
5.1	OPTIMIZATION STATEMENT	104
5.2	CONSTRAINTS	105
5.2.1	<i>Applied loads</i>	105
5.2.2	<i>Allowable stress</i>	106
5.2.3	<i>Allowable stress amplitude</i>	109
5.2.4	<i>Side constraints</i>	111
5.2.5	<i>Buckling load</i>	112
5.3	OPTIMIZATION UNDER DYNAMIC LOAD	112
5.4	VALIDATION OF THE CRANK END DESIGN	121
5.5	OBSERVATIONS FROM THE OPTIMIZATION EXERCISE	125
5.6	MANUFACTURING ASPECTS	126
5.7	ECONOMIC COST ASPECTS	128
6.	SUMMARY AND CONCLUSIONS	153

REFERENCES.....	156
APPENDIX I	159
APPENDIX II.....	165

LIST OF TABLES

Table 2.1	Details of 'slider-crank mechanism-1' used in ADAMS/View -11.	27
Table 2.2	Configuration of the engine to which the connecting rod belongs.	27
Table 2.3	Inputs for FEA of connecting rod using dynamic analysis results at crankshaft speed of 5700 rev/min.	28
Table 2.4	Inputs for FEA of connecting rod using dynamic analysis results at crankshaft speed of 4000 rev/min.	29
Table 2.5	Inputs for FEA of connecting rod using dynamic analysis results at crankshaft speed of 2000 rev/min.	30
Table 3.1	Properties of connecting rod material.	56
Table 3.2	von Mises stresses in the shank region under tensile and compressive loads.	56
Table 3.3	Measured and predicted strains. Locations of strain gages are shown in Figure 3.16. Measured strain is the average of four gages.	57
Table 4.1	Comparison of static axial stresses under the four FEA model boundary conditions.	86
Table 4.2	von Mises stresses at nodes shown in Figure 4.21.	87
Table 5.1	Summary of mechanical properties of existing forged steel and C-70 steel.	131
Table 5.2	Input for quasi-dynamic FEA of the optimized connecting rod, using load analysis results at crankshaft speed of 5700 rev/min.	132
Table 5.3	Minimum factor of safety for regions I through V, shown in Figure 5.9.	133
Table 5.4	Comparison of the optimized connecting rod based on dynamic load analysis with the existing connecting rod.	134

Table 5.5 Cost split up of forged steel and forged powder metal connecting rods (Clark *et al.*, 1989).

135

LIST OF FIGURES

Figure 1.1	Market shares of powder forged, steel forged, and cast connecting rods in European and North American markets, based on an unpublished market analysis for the year 2000 (Ludenbach, 2002).	13
Figure 1.2	Initial and final designs of a connecting rod wrist pin end (Sarihan and Song, 1990).	13
Figure 1.3	The optimum design obtained by Yoo <i>et al.</i> (1984).	14
Figure 1.4	Design of a PM connecting rod (Sonsino and Esper, 1994).	14
Figure 1.5	Stresses at the bottom of the connecting rod column (Ishida <i>et al.</i> , 1995).	15
Figure 1.6	Stresses at the center of the connecting rod column (Ishida <i>et al.</i> , 1995).	15
Figure 2.1	Vector representation of slider-crank mechanism.	31
Figure 2.2	Free body diagram and vector representation. (a) Free body diagram of connecting rod. (b) Free body diagram of piston.	31
Figure 2.3	Typical input required for performing load analysis on the connecting rod and the expected output.	32
Figure 2.4	Slider-crank mechanism -1.	32
Figure 2.5	Angular velocity of link AB for 'slider-crank mechanism-1'- A comparison of the results obtained by DAP and ADAMS/View-11 at 3000 rev/min crank speed (clockwise).	33
Figure 2.6	Angular acceleration of link AB for 'slider-crank mechanism-1'- A comparison of the results obtained by DAP and ADAMS/View-11 at 3000 rev/min crank speed (clockwise).	33
Figure 2.7	Forces at the joint A, for 'slider-crank mechanism-1'- A comparison of the results obtained by DAP and ADAMS/View-11 at 3000 rev/min crank speed. Fx	34

corresponds to F_{AX} and F_y corresponds to F_{AY} .

Figure 2.8	Forces at the joint B for 'slider-crank mechanism-1'- A comparison of the results obtained by DAP and ADAMS/View-11 at 3000 rev/min crank speed. F_x corresponds to F_{BX} and F_y corresponds to F_{BY} .	34
Figure 2.9	Variation of crank angle with time at 3000 rev/min crank speed in clockwise direction.	35
Figure 2.10	Pressure crank angle diagram used to calculate the forces at the connecting rod ends.	35
Figure 2.11	Variation of angular velocity of the connecting rod over one complete engine cycle at crankshaft speed of 5700 rev/min.	36
Figure 2.12	Variation of angular acceleration of the connecting rod over one complete engine cycle at crankshaft speed of 5700 rev/min.	36
Figure 2.13	Variations of the components of the force over one complete cycle at the crank end of the connecting rod at crankshaft speed of 5700 rev/min. F_x corresponds to F_{AX} and F_y corresponds to F_{AY} .	37
Figure 2.14	Variations of the components of the force over one complete cycle at the piston pin end of the connecting rod at crankshaft speed of 5700 rev/min. F_x corresponds to F_{BX} and F_y corresponds to F_{BY} .	37
Figure 2.15	Axial, normal, and the resultant force at the crank end at crank speed of 5700 rev/min.	38
Figure 2.16	Axial, normal, and the resultant force at the piston-pin end at crank speed of 5700 rev/min.	38
Figure 2.17	Variation of the axial, normal (normal to connecting rod axis), and the resultant force at the crank end at crank speed of 4000 rev/min.	39
Figure 2.18	Variation of the axial, normal (normal to connecting rod axis), and the resultant force at the crank end at crank speed of 2000 rev/min.	39

Figure 2.19	Effect of speed on P-V diagram at constant delivery ratio. Curve 5 is for 900 rev/min, curve 6 for 1200 rev/min, curve 7 for 1500 rev/min, and curve 8 for 1800 rev/min (Ferguson, 1986).	40
Figure 2.20	Loads normal to the connecting rod axis. Note that variations from 0° to 360° repeat from 360° to 720°.	40
Figure 2.21	Variation of the axial load at the crank end and the load normal to connecting rod length at the C.G. at 5700 rev/min crankshaft speed. The 360° to 720° variation has been superimposed on 0° to 360° variation. Plot has been divided into three regions: i, ii and iii.	41
Figure 2.22	Variation of load at the crank end over the portion of the cycle that will need FEA at 5700 rev/min crankshaft speed. Markers on the curve represent crank angles at which FEA has been performed.	42
Figure 3.1	Geometry of the connecting rod generated by the digitizing process.	58
Figure 3.2	Solid model of the connecting rod used for FEA. (a) Isometric view. (b) View showing the features at the crank end.	59
Figure 3.3	Locations on the connecting rod used for checking convergence. (a) Locations on the connecting rod. (b) Location at the oil hole.	60
Figure 3.4	von Mises stress at locations 1 through 10 in Figure 3.3. Note that convergence is achieved at most locations with element length of 1.5 mm. Further local refinement with element length of 1 mm produced convergence at location 9.	61
Figure 3.5	Locations on the connecting rod where the stress variation has been traced over one complete cycle of the engine. (a) Locations shown on the 3D connecting rod. (b) Other symmetric locations.	62
Figure 3.6	Stress along the connecting rod axis in the shank of the connecting rod under dynamic loads as a function of mesh	63

size. Locations 12 and 13 are shown in Figure 3.5.

Figure 3.7	Tensile loading of the connecting rod (Webster <i>et al.</i> 1983).	63
Figure 3.8	Polar co-ordinate system R, Θ , Z used. 't' (not shown) is the thickness of the contact surface normal to the plane of paper.	64
Figure 3.9	Compressive loading of the connecting rod (Webster <i>et al.</i> 1983).	64
Figure 3.10	Pressure crank angle diagram also known as the indicator diagram (supplied by OEM).	65
Figure 3.11	Illustration of the way in which boundary conditions were applied when solving the quasi-dynamic FEA model.	65
Figure 3.12	FEA model of the connecting rod with axial tensile load at the crank end with cosine distribution over 180° and piston pin end restrained over 180°.	66
Figure 3.13	FEA model of the connecting rod with axial compressive load at the crank end uniformly distributed over 120° (as shown in Figure 3.9) and piston pin end restrained over 120°.	66
Figure 3.14	Solid model of the test assembly and the finite element model used for the assembly. The FEM includes the axial compressive load applied to the pin at the piston pin end, the restraints applied to the crank pin, the interference simulated by applying pressure, and contact elements between the pins and the connecting rod.	67
Figure 3.15	Location of nodes used for validation of the FEA model.	67
Figure 3.16	Location of two strain gages attached to the connecting rod. Two other gages are on the opposite side in identical positions.	68
Figure 4.1	Stress variation over the engine cycle at 5700 rev/min at locations 1 and 2. XX is the σ_{xx} component of stress. The stress shown for the static tensile load of 17.7 kN, is the von Mises stress.	88

Figure 4.2	Stress variation over the engine cycle at 5700 rev/min at locations 3 and 4. XX is the σ_{xx} component of stress, YY is the σ_{yy} component of stress and so on. The stress shown for the static tensile load of 9.4 kN is the von Mises stress.	88
Figure 4.3	Stress variation over the engine cycle at 5700 rev/min at locations 5 and 6. XX is the σ_{xx} component of stress, YY is the σ_{yy} component and so on. The stress shown for the static tensile load of 17.7 kN is the von Mises stress.	89
Figure 4.4	Stress variation over the engine cycle at 5700 rev/min at locations 7 and 8. YY is the σ_{yy} component, XY is the σ_{xy} component of stress, and so on. The stress shown for the static tensile load of 17.7 kN is the von Mises stress.	89
Figure 4.5	Stress variation over the engine cycle at 5700 rev/min at location 9. YY is the σ_{yy} component. The stress shown for the static tensile load of 17.7 kN is the von Mises stress.	90
Figure 4.6	Stress variation over the engine cycle at 5700 rev/min at locations 10 and 11. YY is the σ_{yy} component, ZZ is the σ_{zz} component of stress and so on. The stress shown for the static tensile load of 9.4 kN is the von Mises stress.	90
Figure 4.7	Stress variation over the engine cycle at 5700 rev/min at locations 12 and 13. XX is the σ_{xx} component of stress. The stress shown under static tensile load of 9.4 kN is the von Mises stress component.	91
Figure 4.8	Stress variation over the engine cycle at 5700 rev/min at locations 14 and 15. XX is the σ_{xx} component of stress, YY is the σ_{yy} component and so on. The stress shown under the static tensile load of 17.7 kN is the von Mises stress.	91
Figure 4.9	Mean stress, stress amplitude, minimum stress and maximum stress at location 12 (w.r.t. Figure 3.5) on the connecting rod as a function of engine speed.	92
Figure 4.10	Mean stress, stress amplitude, and R ratio of the σ_{xx} component, and the equivalent mean stress and equivalent stress amplitude at R = -1 at engine speed of 5700 rev/min at locations 1 through 15.	92

Figure 4.11	Mean stress, stress amplitude and the R ratio of the σ_{yy} component at engine speed of 5700 rev/min at locations 1 through 15.	93
Figure 4.12	Mean stress, stress amplitude, and the R ratio of the σ_{zz} component at engine speed of 5700 rev/min at locations 1 through 15.	93
Figure 4.13	Mean stress, stress amplitude, and the R ratio of the σ_{xy} component at engine speed of 5700 rev/min at locations 1 through 15.	94
Figure 4.14	Mean stress, stress amplitude, and the R ratio of the σ_{xz} component at engine speed of 5700 rev/min at locations 1 through 15.	94
Figure 4.15	Mean stress, stress amplitude, and the R ratio of the σ_{yz} component at engine speed of 5700 rev/min at locations 1 through 15.	95
Figure 4.16	von Mises stress distribution with static tensile load of 26.7 kN at piston pin end. The crank end was restrained.	95
Figure 4.17	von Mises stress distribution with static tensile load of 26.7 kN at the crank end. The pin end was restrained.	96
Figure 4.18	von Mises stress distribution with static compressive load of 26.7 kN at piston pin end. The crank end was restrained.	96
Figure 4.19	von Mises stress distribution with static compressive load of 26.7 kN at the crank end. The piston pin end was restrained.	97
Figure 4.20	von Mises stress at a few discrete locations on the mid plane labeled on the connecting rod, along the length, for tensile (17.7 kN) and compressive loads (21.8 kN).	97
Figure 4.21	Location of the nodes in the web region near the crank end and the pin end transitions, the stresses at which have been tabulated in Table 4.2.	98
Figure 4.22	Schematic representation of the four loading cases considered for analysis.	99

Figure 4.23	Stress ratios at different locations (shown in Figure 3.5) and for different FEA models. Case-1 is the test assembly FEA, Case-2 is the connecting rod-only FEA (with load range comprising of static tensile and compressive loads for both Case -1 and Case-2), Case-3 is the FEA with overall operating range under service condition, Case-4 is the FEA with operating range at 5700 rev/min under service operating condition. All cases are shown in Figure 4.22.	100
Figure 4.24	Figure shows a comparison of the equivalent stress amplitude at $R = -1$ (MPa) under three cases. Case-2 is the connecting rod-only FEA (with range comprising of static tensile and compressive loads), Case-3 is the FEA with overall operating range under service condition, Case-4 is the FEA with operating range at 5700 rev/min under service operating condition.	100
Figure 4.25	Maximum tensile von Mises stress at different locations on the connecting rod under the two cases. Case-2 is the connecting rod-only FEA (with range comprising of static tensile and compressive loads), and Case-4 is the FEA with operating range at 5700 rev/min under service operating condition.	101
Figure 4.26	The factor of safety, ratio of yield strength to the maximum stress, for locations shown in Figure 3.5 and the maximum von Mises stress in the whole operating range.	101
Figure 4.27	The factor of safety, ratio of the endurance limit to the equivalent stress amplitude at $R = -1$, at the locations shown in Figure 3.5 and the equivalent stress amplitude at $R = -1$ considering the whole operating range.	102
Figure 5.1	Failure Index (FI), defined as the ratio of von Mises stress to the yield strength of 700 MPa, under the dynamic tensile load at 360° crank angle for the existing connecting rod and material. Maximum FI is 0.696.	136
Figure 5.2	Failure Index (FI), defined as the ratio of von Mises stress to the yield strength of 700 MPa, under peak static compressive load for the existing connecting rod and material. Maximum FI is 0.395.	136

Figure 5.3	Failure Index (FI), defined as the ratio of equivalent stress amplitude at $R = -1$ to the endurance limit of 423 MPa, for the existing connecting rod and material. Maximum FI is 0.869.	137
Figure 5.4	Drawing of the connecting rod showing few of the dimensions that are design variables and dimensions that cannot be changed. Dimensions that cannot be changed are boxed.	138
Figure 5.5	The geometry of the optimized connecting rod.	139
Figure 5.6	Failure Index (FI), defined as the ratio of von Mises stress to the yield strength of 574 MPa, under the dynamic tensile load occurring at 360° crank angle at 5700 rev/min for the optimized connecting rod. Maximum FI is 0.684.	139
Figure 5.7	Failure Index (FI), defined as the ratio of von Mises stress to the yield strength of 574 MPa, under the peak compressive gas load for the optimized connecting rod. The maximum FI is 0.457.	140
Figure 5.8	Failure Index (FI), defined as the ratio of equivalent stress amplitude at $R = -1$ to the endurance limit of 339 MPa for the optimized connecting rod. Maximum FI is 0.787.	140
Figure 5.9	The various regions of the connecting rod that were analyzed for Failure Index (FI) or Factor of Safety (FS).	141
Figure 5.10	The existing and the optimized connecting rods superimposed.	141
Figure 5.11	Isometric view of the optimized and existing connecting rod.	142
Figure 5.12	Drawing of the optimized connecting rod (bolt holes not included).	143
Figure 5.13	Modeling of the bolt pretension in the connecting rod assembly.	144
Figure 5.14	FE model of the connecting rod assembly consisting of the cap, rod, bolt and bolt pre-tension. The external load corresponds to the load at 360° crank angle at 5700	144

	rev/min and was applied with cosine distribution. The pin end was totally restrained.	
Figure 5.15	von Mises stress variation and displacements of the connecting rod and cap for a FEA model as shown in Figure 5.14 under tensile load described in Section 5.1. The displacement has been magnified 20 times.	145
Figure 5.16	Connecting rod cap on the left shows the edge and the relocated jig spot. The figure of the cap on the right shows the springs connected between the opposite edges of the cap.	145
Figure 5.17	FE model of the connecting rod assembly consisting of the cap, rod, bolt and bolt pre-tension. The external load which corresponds to the load at 360° crank angle at 5700 rev/min was applied with cosine distribution. The pin end was totally restrained. Springs were introduced to model stiffness of other components (i.e. crankshaft, bearings, etc.).	146
Figure 5.18	von Mises stress variation for FEM shown in Figure 5.17	146
Figure 5.19	FE model of the connecting rod assembly consisting of the cap, rod, bolt and bolt pre-tension. The external load corresponds to the compressive load of 21.8 kN and was applied as a uniform distribution. The pin end was totally restrained.	147
Figure 5.20	von Mises stress distribution under compressive load of 21.8 kN for the FEM shown in Figure 5.19.	147
Figure 5.21	A trial connecting rod that was considered for optimization. Not a feasible solution since punching out of the hole in the shank would cause distortion.	148
Figure 5.22	Steel forged connecting rod manufacturing process flow chart (correspondence with Mr. Tom Elmer from MAHLE Engine Components, Gananoque, ON, Canada). The number in each box is the cost in \$ and the number in the parentheses is the percent of the total cost.	149
Figure 5.23	Powder forged connecting rod manufacturing process flow chart. The number in each box is the cost in \$ and the	150

number in the parentheses is the percent of the total cost.

- Figure 5.24 C-70 connecting rod manufacturing process flow chart (correspondence with Mr. Tom Elmer from MAHLE Engine Components, Gananoque, ON, Canada). The number in each box is the cost in \$ and the number in the parentheses is the percent of the total cost. 151
- Figure 5.25 The fracture splitting process for steel forged connecting rod (Park *et al.*, 2003). 152

NOMENCLATURE

a_A, a_p	Acceleration of point A, piston
a	Absolute acceleration of a point on the connecting rod
$a_{c.gX}, a_{c.gY}$	X, Y components of the acceleration of the C.G. of the connecting rod
E	Modulus of elasticity
e	Offset, the distance from the centerline of the slider path to the crank bearing center
FI, FS	Failure index, factor of safety
F_a	Load amplitude
F_m	Mean load
F_X	Force in X direction on piston
F_{AX}, F_{AY}	X, Y components of the reactions at the crank end
F_{BX}, F_{BY}	X, Y components of the reactions at the piston pin end
I_{ZZ}	Moment of Inertia about Z axis and C.G. of the connecting rod
m	Slope of the modified Goodman line
m_p, m_c	Mass of piston assembly, connecting rod
p	Normal pressure
p_o	Normal pressure constant
P_t, P_c	Tensile, compressive resultant load in the direction of the rod length

R	Transition radius
r	Radius of crankshaft pin
r_1	Radius of crank
r_2	Connecting rod length
r_3	Distance from crankshaft bearing center to slider (piston pin center)
r_o	Outer radius of outer member
r_i	Inner radius of inner member
S_a, S_m	Alternating, mean stress
S_{ax}, S_{ay}, S_{az}	Alternating x, y, z stress
S_{mx}, S_{my}, S_{mz}	Mean x, y, z stress
S_{max}, S_{min}	Maximum, minimum stress
S_{Nf}	Equivalent stress amplitude at $R = -1$
S_{qa}, S_{qm}	Equivalent stress amplitude, equivalent mean stress
S_u	Ultimate tensile strength
t	Thickness of the connecting rod at the loading surface
u	Distance of C.G. of the connecting rod from crank end center
V_p	Slider velocity in X direction
δ	Total radial interference

ρ	Position vector of any point on connecting rod
$\tau_{axy}, \tau_{ayz}, \tau_{azx}$	xy, yz, zx shear stress amplitude
$\sigma_{xx}, \sigma_{yy}, \sigma_{zz}$	x, y, z components of normal stress
$\sigma_{xy}, \sigma_{yz}, \sigma_{zx}$	xy, yz, zx components of shear stress
ω_1	Angular velocity of crankshaft
ω_2	Angular velocity of connecting rod
α_2	Angular acceleration of connecting rod
θ, Θ	Crank angle, angular coordinate of polar coordinate system defined for the contact surface
β	Connecting rod angle with positive direction of X axis
η	$(2\pi-\beta)$

1. INTRODUCTION

1.1 BACKGROUND

The automobile engine connecting rod is a high volume production, critical component. It connects reciprocating piston to rotating crankshaft, transmitting the thrust of the piston to the crankshaft. Every vehicle that uses an internal combustion engine requires at least one connecting rod depending upon the number of cylinders in the engine.

Connecting rods for automotive applications are typically manufactured by forging from either wrought steel or powdered metal. They could also be cast. However, castings could have blow-holes which are detrimental from durability and fatigue points of view. The fact that forgings produce blow-hole-free and better rods gives them an advantage over cast rods (Gupta, 1993). Between the forging processes, powder forged or drop forged, each process has its own pros and cons. Powder metal manufactured blanks have the advantage of being near net shape, reducing material waste. However, the cost of the blank is high due to the high material cost and sophisticated manufacturing techniques (Reppen, 1998). With steel forging, the material is inexpensive and the rough part manufacturing process is cost effective. Bringing the part to final dimensions under tight tolerance results in high expenditure for machining, as the blank usually contains more excess material (Reppen, 1998). A sizeable portion of the US market for connecting

rods is currently consumed by the powder metal forging industry. A comparison of the European and North American connecting rod markets indicates that according to an unpublished market analysis for the year 2000 (Ludenbach, 2002), 78% of the connecting rods in Europe (total annual production: 80 million approximately) are steel forged as opposed to 43% in North America (total annual production: 100 million approximately), as shown in Figure 1.1. In order to recapture the US market, the steel industry has focused on development of production technology and new steels. AISI (American Iron and Steel Institute) funded a research program that had two aspects to address. The first aspect was to investigate and compare fatigue strength of steel forged connecting rods with that of the powder forged connecting rods. The second aspect was to optimize the weight and manufacturing cost of the steel forged connecting rod. The first aspect of this research program has been dealt with in a master's thesis entitled "Fatigue Behavior and Life predictions of Forged Steel and PM Connecting Rods" (Afzal A., 2004). This current thesis deals with the second aspect of the study, the optimization part.

Due to its large volume production, it is only logical that optimization of the connecting rod for its weight or volume will result in large-scale savings. It can also achieve the objective of reducing the weight of the engine component, thus reducing inertia loads, reducing engine weight and improving engine performance and fuel economy.

1.2 LITERATURE REVIEW

The connecting rod is subjected to a complex state of loading. It undergoes high cyclic loads of the order of 10^8 to 10^9 cycles, which range from high compressive loads

due to combustion, to high tensile loads due to inertia. Therefore, durability of this component is of critical importance. Due to these factors, the connecting rod has been the topic of research for different aspects such as production technology, materials, performance simulation, fatigue, etc. For the current study, it was necessary to investigate finite element modeling techniques, optimization techniques, developments in production technology, new materials, fatigue modeling, and manufacturing cost analysis. This brief literature survey reviews some of these aspects.

Webster *et al.* (1983) performed three dimensional finite element analysis of a high-speed diesel engine connecting rod. For this analysis they used the maximum compressive load which was measured experimentally, and the maximum tensile load which is essentially the inertia load of the piston assembly mass. The load distributions on the piston pin end and crank end were determined experimentally. They modeled the connecting rod cap separately, and also modeled the bolt pretension using beam elements and multi point constraint equations.

In a study reported by Repgen (1998), based on fatigue tests carried out on identical components made of powder metal and C-70 steel (fracture splitting steel), he notes that the fatigue strength of the forged steel part is 21% higher than that of the powder metal component. He also notes that using the fracture splitting technology results in a 25% cost reduction over the conventional steel forging process. These factors suggest that a fracture splitting material would be the material of choice for steel forged connecting rods. He also mentions two other steels that are being tested, a modified micro-alloyed steel and a modified carbon steel. Other issues discussed by Repgen are the necessity to avoid jig spots along the parting line of the rod and the cap, need of

consistency in the chemical composition and manufacturing process to reduce variance in microstructure and production of near net shape rough part.

Park *et al.* (2003) investigated microstructural behavior at various forging conditions and recommend fast cooling for finer grain size and lower network ferrite content. From their research they concluded that laser notching exhibited best fracture splitting results, when compared with broached and wire cut notches. They optimized the fracture splitting parameters such as, applied hydraulic pressure, jig set up and geometry of cracking cylinder based on delay time, difference in cracking forces and roundness. They compared fracture splitting high carbon micro-alloyed steel (0.7% C) with carbon steel (0.48% C) using rotary bending fatigue test and concluded that the former has the same or better fatigue strength than the later. From a comparison of the fracture splitting high carbon micro-alloyed steel and powder metal, based on tension-compression fatigue test they noticed that fatigue strength of the former is 18% higher than the later.

Sarihan and Song (1990), for the optimization of the wrist pin end, used a fatigue load cycle consisting of compressive gas load corresponding to maximum torque and tensile load corresponding to maximum inertia load. Evidently, they used the maximum loads in the whole operating range of the engine. To design for fatigue, modified Goodman equation with alternating octahedral shear stress and mean octahedral shear stress was used. For optimization, they generated an approximate design surface, and performed optimization of this design surface. The objective and constraint functions were updated to obtain precise values. This process was repeated till convergence was achieved. They also included constraints to avoid fretting fatigue. The mean and the alternating components of the stress were calculated using maximum and minimum

values of octahedral shear stress. Their exercise reduced the connecting rod weight by nearly 27%. The initial and final connecting rod wrist pin end designs are shown in Figure 1.2.

Yoo *et al.* (1984) used variational equations of elasticity, material derivative idea of continuum mechanics and an adjoint variable technique to calculate shape design sensitivities of stress. The results were used in an iterative optimization algorithm, steepest descent algorithm, to numerically solve an optimal design problem. The focus was on shape design sensitivity analysis with application to the example of a connecting rod. The stress constraints were imposed on principal stresses of inertia and firing loads. But fatigue strength was not addressed. The other constraint was the one on thickness to bound it away from zero. They could obtain 20% weight reduction in the neck region of the connecting rod. The optimum design is shown in Figure 1.3.

Hippoliti (1993) reported design methodology in use at Piaggio for connecting rod design, which incorporates an optimization session. However, neither the details of optimization nor the load under which optimization was performed were discussed. Two parametric FE procedures using 2D plane stress and 3D approach developed by the author were compared with experimental results and shown to have good agreements. The optimization procedure they developed was based on the 2D approach.

El-Sayed and Lund (1990) presented a method to consider fatigue life as a constraint in optimal design of structures. They also demonstrated the concept on a SAE key hole specimen. In this approach a routine calculates the life and in addition to the stress limit, limits are imposed on the life of the component as calculated using FEA results.

Pai (1996) presented an approach to optimize shape of connecting rod subjected to a load cycle, consisting of the inertia load deducted from gas load as one extreme and peak inertia load exerted by the piston assembly mass as the other extreme, with fatigue life constraint. Fatigue life defined as the sum of the crack initiation and crack growth lives, was obtained using fracture mechanics principles. The approach used finite element routine to first calculate the displacements and stresses in the rod; these were then used in a separate routine to calculate the total life. The stresses and the life were used in an optimization routine to evaluate the objective function and constraints. The new search direction was determined using finite difference approximation with design sensitivity analysis. The author was able to reduce the weight by 28%, when compared with the original component.

Sonsino and Esper (1994) have discussed the fatigue design of sintered connecting rods. They did not perform optimization of the connecting rod. They designed a connecting rod with a load amplitude $F_a = 19.2$ kN and with different regions being designed for different load ratios (R), such as, in the stem $F_m = -2.2$ kN and $R = -1.26$, at the piston pin end $F_m = -5.5$ kN and $R = -1.82$, at the crank end $F_m = 7.8$ kN and $R = -0.42$. They performed preliminary FEA followed by production of a prototype. Fatigue tests and experimental stress analysis were performed on this prototype based on the results of which they proposed a final shape, shown in Figure 1.4. In order to verify that the design was sufficient for fatigue, they computed the allowable stress amplitude at critical locations, taking the R-ratio, the stress concentration, and statistical safety factors into account, and ensured that maximum stress amplitudes were below the allowable stress amplitude.

For their optimization study, Serag *et al.* (1989) developed approximate mathematical formulae to define connecting rod weight and cost as objective functions and also the constraints. The optimization was achieved using a Geometric Programming technique. Constraints were imposed on the compression stress, the bearing pressure at the crank and the piston pin ends. Fatigue was not addressed. The cost function was expressed in some exponential form with the geometric parameters.

Folgar *et al.* (1987) developed a fiber FP/Metal matrix composite connecting rod with the aid of FEA, and loads obtained from kinematic analysis. Fatigue was not addressed at the design stage. However, prototypes were fatigue tested. The investigators identified design loads in terms of maximum engine speed, and loads at the crank and piston pin ends. They performed static tests in which the crank end and the piston pin end failed at different loads. Clearly, the two ends were designed to withstand different loads.

Balasubramaniam *et al.* (1991) reported computational strategy used in Mercedes-Benz using examples of engine components. In their opinion, 2D FE models can be used to obtain rapid trend statements, and 3D FE models for more accurate investigation. The various individual loads acting on the connecting rod were used for performing simulation and actual stress distribution was obtained by superposition. The loads included inertia load, firing load, the press fit of the bearing shell, and the bolt forces. No discussions on the optimization or fatigue, in particular, were presented.

Ishida *et al.* (1995) measured the stress variation at the column center and column bottom of the connecting rod, as well as the bending stress at the column center. The plots, shown in Figures 1.5 and 1.6 indicate that at the higher engine speeds, the peak tensile stress does not occur at 360° crank angle or top dead center. It was also observed

that the R ratio varies with location, and at a given location it also varies with the engine speed. The maximum bending stress magnitude over the entire cycle (0° to 720° crank angle) at 12000 rev/min, at the column center was found to be about 25% of the peak tensile stress over the same cycle.

Athavale and Sajanpawar (1991) modeled the inertia load in their finite element model. An interface software was developed to apply the acceleration load to elements on the connecting rod depending upon their location, since acceleration varies in magnitude and direction with location on the connecting rod. They fixed the ends of the connecting rod, to determine the deflection and stresses. This, however, may not be representative of the pin joints that exist in the connecting rod. The results of the detailed analysis were not discussed, rather, only the modeling technique was discussed. The connecting rod was separately analyzed for the tensile load due to the piston assembly mass (piston inertia), and for the compressive load due to the gas pressure. The effect of inertia load due to the connecting rod, mentioned above, was analyzed separately.

While investigating a connecting rod failure that led to a disastrous failure of an engine, Rabb (1996) performed a detailed FEA of the connecting rod. He modeled the threads of the connecting rod, the threads of connecting rod screws, the prestress in the screws, the diametral interference between the bearing sleeve and the crank end of the connecting rod, the diametral clearance between the crank and the crank bearing, the inertia load acting on the connecting rod, and the combustion pressure. The analysis clearly indicated the failure location at the thread root of the connecting rod, caused by improper screw thread profile. The connecting rod failed at the location indicated by the FEA. An axisymmetric model was initially used to obtain the stress concentration factors

at the thread root. These were used to obtain nominal mean and alternating stresses in the screw. A detailed FEA including all the factors mentioned above was performed by also including a plasticity model and strain hardening. Based on the comparison of the mean stress and stress amplitude at the threads obtained from this analysis with the endurance limits obtained from specimen fatigue tests, the adequacy of a new design was checked. Load cycling was also used in inelastic FEA to obtain steady state situation.

In a published SAE case study (1997), a replacement connecting rod with 14% weight savings was designed by removing material from areas that showed high factor of safety. Factor of safety with respect to fatigue strength was obtained by performing FEA with applied loads including bolt tightening load, piston pin interference load, compressive gas load and tensile inertia load. The study lays down certain guidelines regarding the use of the fatigue limit of the material and its reduction by a certain factor to account for the as-forged surface. The study also indicates that buckling and bending stiffness are important design factors that must be taken into account during the design process. On the basis of the stress and strain measurements performed on the connecting rod, close agreement was found with loads predicted by inertia theory. The study also concludes that stresses due to bending loads are substantial and should always be taken into account during any design exercise.

1.3 OBJECTIVES AND OUTLINE

The objective of this work was to optimize the forged steel connecting rod for its weight and cost. The optimized forged steel connecting rod is intended to be a more

attractive option for auto manufacturers to consider, as compared with its powder-forged counterpart.

Optimization begins with identifying the correct load conditions and magnitudes. Overestimating the loads will simply raise the safety factors. The idea behind optimizing is to retain just as much strength as is needed. Commercial softwares such as I-DEAS and ADAMS-View can be used to obtain the variation of quantities such as angular velocity, angular acceleration, and load. However, usually the worst case load is considered in the design process. Literature review suggests that investigators use maximum inertia load, inertia load, or inertia load of the piston assembly mass as one extreme load corresponding to the tensile load, and firing load or compressive gas load corresponding to maximum torque as the other extreme design load corresponding to the compressive load. Inertia load is a time varying quantity and can refer to the inertia load of the piston, or of the connecting rod. In most cases, in the literature the investigators have not clarified the definition of inertia load - whether it means only the inertia of the piston, or whether it includes the inertia of the connecting rod as well. Questions are naturally raised in light of such complex structural behavior, such as: Does the peak load at the ends of the connecting rod represent the worst case loading? Under the effect of bending and axial loads, can one expect higher stresses than that experienced under axial load alone? Moreover, very little information is available in the literature on the bending stiffness requirements, or on the magnitude of bending stress. From the study of Ishida *et al.* (1995) reviewed in Section 1.2, it is clear that the maximum stress at the connecting rod column bottom does not occur at the TDC, and the maximum bending stress at the column center is about 25% of the maximum stress at that location. However, to obtain

the bending stress variation over the connecting rod length, or to know the stress at critical locations such as the transition regions of the connecting rod, a detailed analysis is needed. As a result, for the forged steel connecting rod investigated, a detailed load analysis under service operating conditions was performed, followed by a quasi-dynamic FEA to capture the stress variation over the cycle of operation.

Logically, any optimization should be preceded by stress analysis of the existing component, which should be performed at the correct operating loads. Consequently, the load analysis is addressed in Chapter 2, followed by a discussion of the finite element modeling issues in Chapter 3, and the results of FEA in Chapter 4. Chapter 3 discusses such issues as mesh convergence, details of how loads and restraints have been applied, and validation of the FE model for three cases - static FEA, quasi-dynamic FEA, and test assembly FEA. Chapter 4 discusses the stress-time history, R ratio and multiaxiality of stresses for various locations on the connecting rod under service operating conditions. This indicates the extent of weight reduction to expect through optimization, identifies the regions from which material can be removed, or regions that need to be redesigned. This chapter also discusses the static FEA results and makes a comparison between the static FEA, quasi-dynamic FEA, and results from test assembly FEA. Optimization of the connecting rod is addressed in Chapter 5. Optimization was performed to reduce the mass and manufacturing cost of the connecting rod, subject to fatigue life and yielding constraints. The material was changed to C-70 fracture splittable steel to reduce manufacturing cost by elimination of machining of mating surfaces of the connecting rod and its cap. S-N approach was used for the fatigue model during the optimization, as the connecting rod operates in the elastic range (i.e. high cycle fatigue life region). A

comparison between the various manufacturing processes and their costs is also presented.

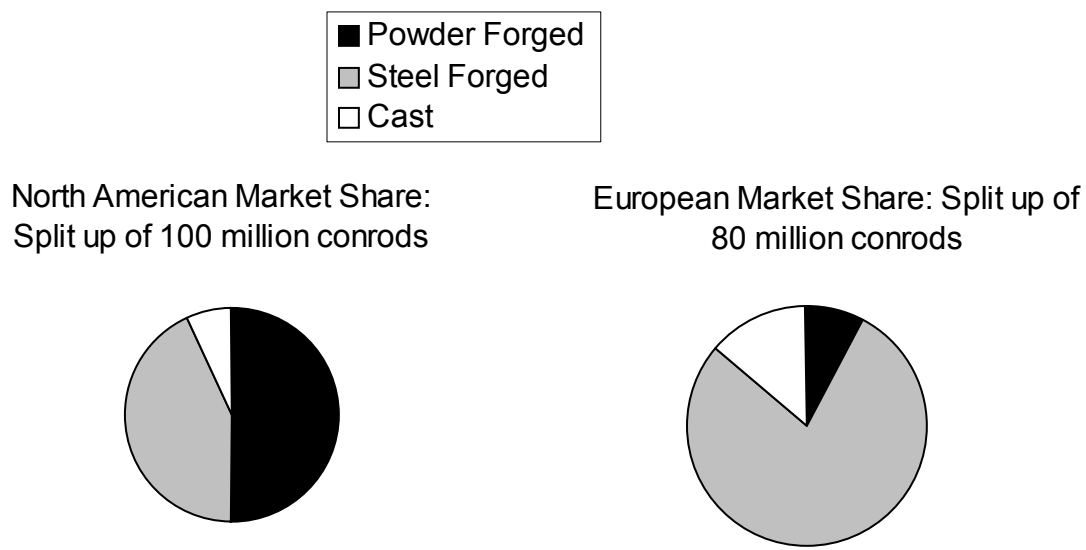


Figure 1.1: Market shares of powder forged, steel forged and cast connecting rods in European and North American markets, based on an unpublished market analysis for the year 2000 (Ludenbach, 2002).

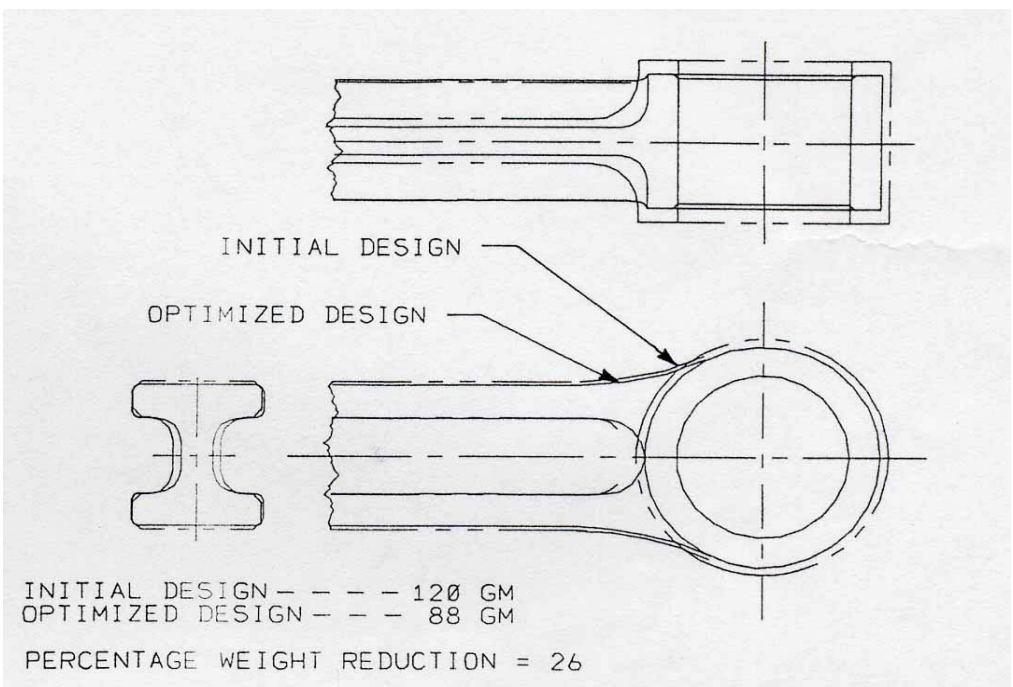


Figure 1.2: Initial and final designs of a connecting rod wrist pin end (Sarihan and Song, 1990).

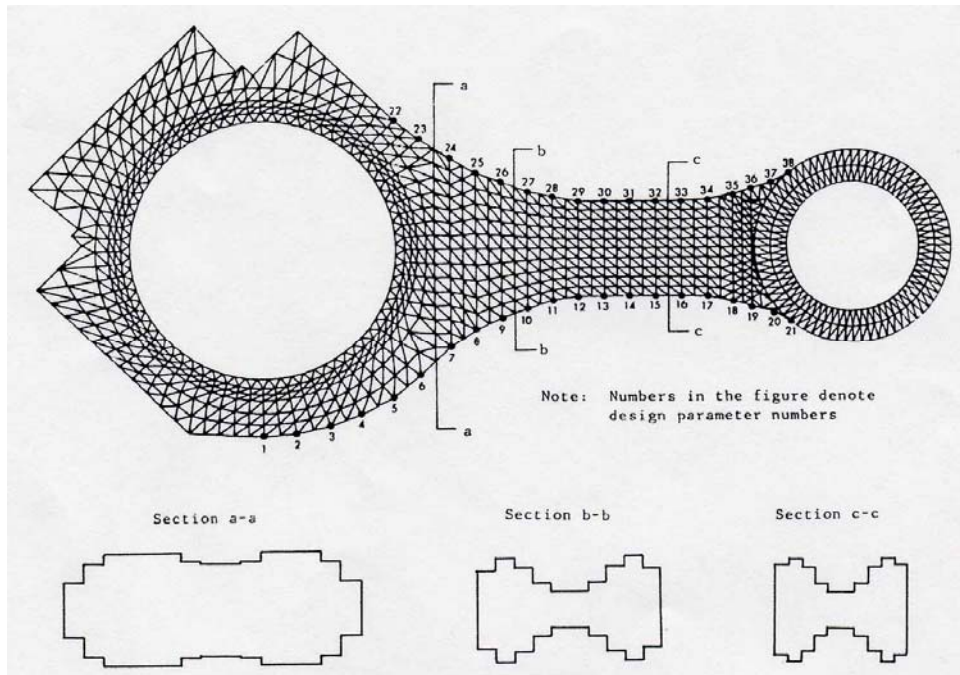


Figure 1.3: The optimum design obtained by Yoo *et al.* (1984).

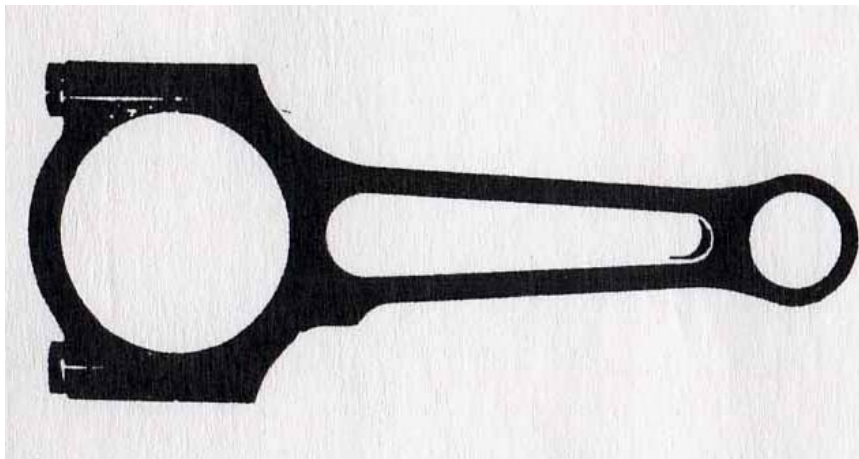


Figure 1.4: Design of a PM connecting rod (Sonsino and Esper, 1994).

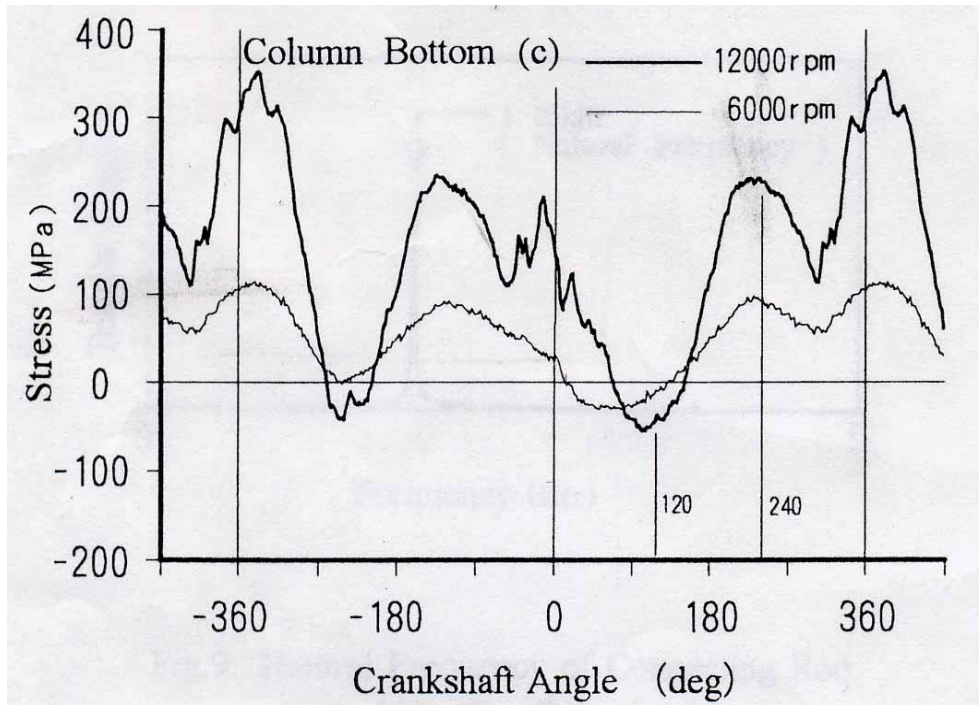


Figure 1.5: Stresses at the bottom of the connecting rod column (Ishida *et al.*, 1995).

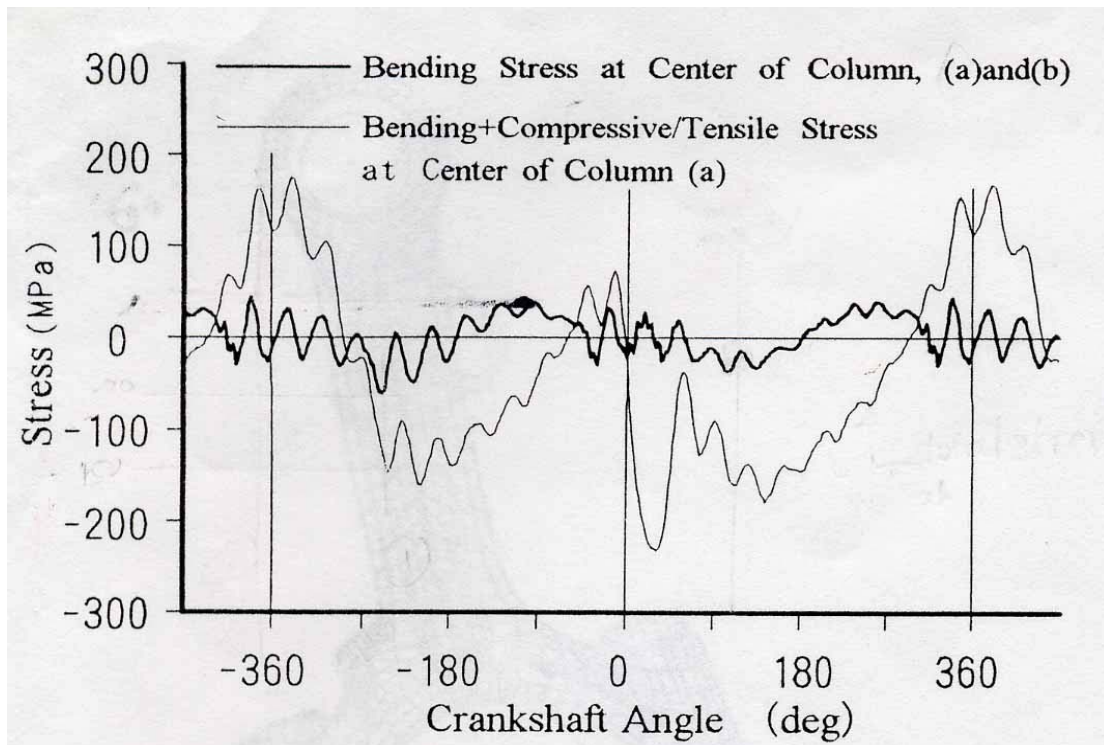


Figure 1.6: Stresses at the center of the connecting rod column (Ishida *et al.*, 1995).

2. DYNAMIC LOAD ANALYSIS OF THE CONNECTING ROD

The connecting rod undergoes a complex motion, which is characterized by inertia loads that induce bending stresses. In view of the objective of this study, which is optimization of the connecting rod, it is essential to determine the magnitude of the loads acting on the connecting rod. In addition, significance of bending stresses caused by inertia loads needs to be determined, so that we know whether it should be taken into account or neglected during the optimization. Nevertheless, a proper picture of the stress variation during a loading cycle is essential from fatigue point of view and this will require FEA over the entire engine cycle.

The objective of this chapter is to determine these loads that act on the connecting rod in an engine so that they may be used in FEA. The details of the analytical vector approach to determine the inertia loads and the reactions are presented in Appendix I. This approach is explained by Wilson and Sadler (1993). The equations are further simplified so that they can be used in a spreadsheet format. The results of the analytical vector approach have been enumerated in this chapter.

This work serves two purposes. It can be used for determining the inertia loads and reactions for any combination of engine speed, crank radius, pressure-crank angle diagram, piston diameter, piston assembly mass, connecting rod length, connecting rod mass, connecting rod moment of inertia, and direction of engine rotation. Secondly, it serves as a means of verifying that the results from ADAMS/View-11 are interpreted in

the right manner. However, for reasons of convenience of reading and transferring data the analytical work was used as the basis and the commercial software was used as a verification tool.

In summary, this chapter enumerates the results of the analytical vector approach used for developing a spread sheet in MS EXCEL (hereafter referred to as DAP-Dynamic Analysis Program), verifies this DAP by using a simple model in ADAMS, uses DAP for dynamic analysis of the forged steel connecting rod, and discusses how the output from DAP is used in FEA. It is to be noted that this analysis assumes the crank rotates at a constant angular velocity. Therefore, angular acceleration of the crank is not included in this analysis. However, in a comparison of the forces at the ends of the connecting rod under conditions of acceleration and deceleration (acceleration of 6000 rev/s² and deceleration of 714 rev/sec² based on approximate measurements) with the forces under constant speed, the difference was observed to be less than 1%. The comparison was done for an engine configuration similar to the one considered in this study.

2.1 ANALYTICAL VECTOR APPROACH

The analytical vector approach (Wilson and Sadler, 1993) has been discussed in detail in Appendix I. With reference to Figure 2.1, for the case of zero offset ($e = 0$), for any given crank angle θ , the orientation of the connecting rod is given by:

$$\beta = \sin^{-1}\{-r_1 \sin\theta / r_2\} \quad (2.1)$$

Angular velocity of the connecting rod is given by the expression:

$$\boldsymbol{\omega}_2 = \omega_2 \mathbf{k} \quad (2.2)$$

$$\omega_2 = -\omega_1 \cos\theta / [(r_2/r_1)^2 - \sin^2\theta]^{0.5} \quad (2.3)$$

Note that bold letters represent vector quantities. The angular acceleration of the connecting rod is given by:

$$\mathbf{\alpha}_2 = \alpha_2 \mathbf{k} \quad (2.4)$$

$$\alpha_2 = (1/\cos\beta) [\omega_1^2 (r_1/r_2) \sin\theta - \omega_2^2 \sin\beta] \quad (2.5)$$

Absolute acceleration of any point on the connecting rod is given by the following equation:

$$\begin{aligned} \mathbf{a} = & (-r_1 \omega_1^2 \cos\theta - \omega_2^2 u \cos\beta - \alpha_2 u \sin\beta) \mathbf{i} \\ & + (-r_1 \omega_1^2 \sin\theta - \omega_2^2 u \sin\beta + \alpha_2 u \cos\beta) \mathbf{j} \end{aligned} \quad (2.6)$$

Acceleration of the piston is given by:

$$\begin{aligned} \mathbf{a}_p = & (-\omega_1^2 r_1 \cos\theta - \omega_2^2 r_2 \cos\beta - \alpha_2 r_2 \sin\beta) \mathbf{i} \\ & + (-\omega_1^2 r_1 \sin\theta - \omega_2^2 r_2 \sin\beta + \alpha_2 r_2 \cos\beta) \mathbf{j} \end{aligned} \quad (2.7)$$

Forces acting on the connecting rod and the piston are shown in Figure 2.2. Neglecting the effect of friction and of gravity, equations to obtain these forces are listed below. Note that m_p is the mass of the piston assembly and m_c is the mass of the connecting rod. Forces at the piston pin and crank ends in X and Y directions are given by:

$$F_{BX} = -(m_p a_p + \text{Gas Load}) \quad (2.8)$$

$$F_{AX} = m_c a_{c.gX} - F_{BX} \quad (2.9)$$

$$F_{BY} = [m_c a_{c.gY} u \cos\beta - m_c a_{c.gX} u \sin\beta + I_{zz} \alpha_2 + F_{BX} r_2 \sin\beta] / (r_2 \cos\beta) \quad (2.10)$$

$$F_{AY} = m_c a_{c.gY} - F_{BY} \quad (2.11)$$

These equations have been used in an EXCEL spreadsheet, referred to earlier in this chapter as DAP (Dynamic Analysis Program). This program provides values of angular velocity and angular acceleration of the connecting rod, linear acceleration of the

crank end center, and forces at the crank and piston pin ends. These results were used in the FE model while performing quasi-dynamic FEA. An advantage of this program is that with the availability of the input as shown in Figure 2.3, the output could be generated in a matter of minutes. This is a small fraction of the time required when using commercial softwares. When performing optimization, this is advantageous since the reactions or the loads at the connecting rod ends changed with the changing mass of the connecting rod. The loads required to perform FEA were obtained relatively quickly using this program. A snap shot of the spread sheet is shown in Appendix II.

2.2 VERIFICATION OF ANALYTICAL APPROACH

The analytical approach used in this study was verified with the results obtained from ADAMS/View -11. A simple slider crank mechanism as shown in Figure 2.4 was used in ADAMS. This mechanism will be referred to as ‘slider-crank mechanism-1’ and its details have been tabulated in Table 2.1. The crank OA rotates about point O and the end B of the (connecting rod) link AB slides along the line OB. The material density used is 7801.0 kg/m^3 ($7.801\text{E-}006 \text{ kg/mm}^3$). Crank OA rotational speed is 3000 rev/min clockwise.

All these details were input to the DAP. Results were generated for the clockwise crank rotation of the ‘slider crank mechanism-1’. It is to be noted that the gas load is not included here since the purpose is just to verify the DAP. However, it is just a matter of superimposing the gas load with the load at the piston pin end in DAP, when it is used for the actual connecting rod analysis.

For a 2D mechanism such as a slider crank mechanism, we can expect forces only in the plane of motion. Forces in Z direction will be zero. There will also be no moments since there are pin joints at both the ends of the connecting rod. The results of the dynamic analysis for 'slider-crank mechanism-1' using DAP have been plotted in Figures 2.5 through 2.8. The results from ADAMS have also been plotted in these Figures. Figure 2.5 shows the variation of the angular velocity of link AB over one complete rotation of the crank as obtained by both the DAP and ADAMS. At the above-mentioned speed of 3000 rev/min the crank completes one complete rotation in 0.02 sec, which is the time over which the angular velocity has been plotted. The two curves coincide indicating agreement of the results from DAP with the results from ADAMS/View-11. Similarly, Figure 2.6 shows the variation of angular acceleration of link AB, Figure 2.7 shows the variation of the forces at joint A, and Figure 2.8 shows the variation of forces at joint B. In all these figures since the curves of DAP and ADAMS/View-11 coincide, it can be concluded that there is perfect agreement of the results from DAP with the results from ADAMS/View-11. These results verify correctness of the DAP. For each of the quantities plotted the variation will repeat itself for subsequent rotations of the crank. The variation of the crank angle with time is shown in Figure 2.9. It needs to be mentioned here that ADAMS or I-DEAS provides all of the required parameters or quantities. DAP was, however, used for this study, essentially due to its simplicity as compared to either I-DEAS or ADAMS. These softwares require generation of the entire mechanism, which is relatively time consuming.

2.3 DYNAMIC ANALYSIS FOR THE ACTUAL CONNECTING ROD

Now that the DAP has been verified, it can be used to generate the required quantities for the actual connecting rod which is being analyzed. The engine configuration considered has been tabulated in Table 2.2. The pressure crank angle diagram used is shown in Figure 2.10 obtained from a different OEM engine (5.4 liter, V8 with compression ratio 9, at speed of 4500 rev/min). These data are input to the DAP, and results consisting of the angular velocity and angular acceleration of the connecting rod, linear acceleration of the connecting rod crank end center and of the center of gravity, and forces at the ends are generated for a few engine speeds.

Results for this connecting rod at the maximum engine speed of 5700 rev/min have been plotted in Figures 2.11 through 2.14. Figure 2.11 shows the variation of the angular velocity over one complete engine cycle at crankshaft speed of 5700 rev/min. Figure 2.12 shows the variation of angular acceleration at the same crankshaft speed. Note that the variation of angular velocity and angular acceleration from 0° to 360° is identical to its variation from 360° to 720° . Figure 2.13 shows the variation of the force acting at the crank end. Two components of the force are plotted, one along the direction of the slider motion, F_x , and the other normal to it, F_y . These two components can be used to obtain crank end force in any direction. Figure 2.14 shows similar components of load at the piston pin end. It would be particularly beneficial if components of these forces were obtained along the length of the connecting rod and normal to it. These components are shown in Figure 2.15 for the crank end and Figure 2.16 for the piston pin end.

At any point in time the forces calculated at the ends form the external loads, while the inertia load forms the internal load acting on the connecting rod. These result in a set of completely equilibrated external and internal loads. A similar analysis was performed at other engine speeds (i.e. 4000 rev/min and 2000 rev/min). The variation of the forces at the crank end at the above mentioned speeds are shown in Figures 2.17 and 2.18, respectively. Note from these figures that as the speed increases the tensile load increases whereas the maximum compressive load at the crank end decreases. Based on the axial load variation at the crank end, the load ratio changes from -11.83 at 2000 rev/min to -1.65 at 4000 rev/min. The load amplitude increases slightly and the mean load tends to become tensile. The positive axial load is the compressive load in these figures due to the co-ordinate system used (shown in the inset in these figures). The pressure-crank angle diagram changes with speed. The actual change will be unique to an engine. The pressure-crank angle diagram for different speeds for the engine under consideration was not available. Therefore, the same diagram was used for different engine speeds. However, from a plot showing the effect of speed on P-V diagram at constant delivery ratio, Figure 2.19 (Ferguson, 1986), barely any change in the peak gas pressure is seen at different speeds, though, a change of nearly 10% is visible at lower pressures. Delivery ratio is the ratio of entering or delivered air mass to the ideal air mass at ambient density. However, note that the speeds for which these have been plotted are much lower than the maximum speed for this engine.

2.4 FEA WITH DYNAMIC LOADS

Once the components of forces at the connecting rod ends in the X and Y directions are obtained, they can be resolved into components along the connecting rod length and normal to it. The components of the inertia load acting at the center of gravity can also be resolved into similar components. It is neither efficient nor necessary to perform FEA of the connecting rod over the entire cycle and for each and every crank angle. Therefore, a few positions of the crank were selected depending upon the magnitudes of the forces acting on the connecting rod, at which FEA was performed. The justification used in selecting these crank positions is as follows:

The stress at a point on the connecting rod as it undergoes a cycle consists of two components, the bending stress component and the axial stress component. The bending stress depends on the bending moment, which is a function of the load at the C.G. normal to the connecting rod axis, as well as angular acceleration and linear acceleration component normal to the connecting rod axis. The variation of each of these three quantities over 0° – 360° is identical to the variation over 360° – 720° . This can be seen from Figure 2.20 for the normal load at the connecting rod ends and at the center of gravity. In addition, Figure 2.12 shows identical variation of angular acceleration over 0° – 360° and 360° – 720° . Therefore, for any given point on the connecting rod the bending moment varies in an identical fashion from 0° – 360° crank angle as it varies from 360° – 720° crank angle.

The axial load variation, however, does not follow this repetitive pattern. (i.e one cycle of axial load variation consists of the entire 720°). This is due to the variation in the

gas load, one cycle of which consists of 720° . However, the variation over 0° – 360° can be superimposed with the variation over 360° – 720° and this plot can be used to determine the worst of the two cycles of 0° – 360° and 360° – 720° to perform FEA, as shown in Figure 2.21. In this figure, a point on the “Axial: 360-720” curve, say at 20° crank angle, actually represents $360^\circ + 20^\circ$ or 380° crank angle.

The axial load at the crank end and at the piston pin end are not generally identical at any point in time. They differ due to the inertia load acting on the connecting rod. The load at either end could be used as a basis for deciding points at which to perform FEA. The load at the crank end was used in this work.

In order to decide the crank angles at which to perform the FEA and to narrow down the crank angle range, the axial load at the crank end from 0° – 360° was compared with axial load at the crank end from 360° – 720° . Positive load at the crank end in Figure 2.21 indicates compressive load and negative load indicates tensile load on the connecting rod. This is due to the co-ordinate system which has been shown in the figure in the inset. The plot in Figure 2.21 can be divided into 3 regions: i, ii & iii, as shown in this figure.

Region ii shows two curves ‘b’ and ‘e’. Curve ‘b’ is higher than curve ‘e’ for most of the region. So curve ‘e’ was not analyzed. FEA at one crank angle on the curve ‘e’ was performed to ensure that the stresses are in fact lower on this curve. Region iii shows curves ‘c’ and ‘f’. Since curve ‘c’ represents a higher load than curve ‘f’, curve ‘f’ was not analyzed.

Eliminating the ‘e’ and ‘f’ portions of the curves leaves curves ‘a’, ‘b’, ‘c’, and ‘d’ to be analyzed in the range 0° – 431° . Over this range, FEA had to be performed at

adequate crank angles so as to pick up the stress variation as accurately as possible. What was discussed above was based on the load at the crank end. A similar trend was observed for the load at the piston pin end. Figure 2.22 shows the variation of load from 0° to 431° crank angle at the crank end. From this diagram, the following crank angles based on peaks and valleys were picked for FEA: 0° , 24° (crank angle close to the peak gas pressure), 60° , 126° , 180° , 243° , 288° , 336° , 360° (peak tensile load), 396° , and 432° . These crank angles are shown in Figure 2.22. In addition, FEA was performed for crank angles of 486° and 696° to validate the premise on which curves 'e' and 'f' were eliminated.

The above discussion was for crank speed of 5700 rev/min. In order to study effect of engine speed (rev/min) FEA was performed at other crankshaft speeds viz, 4000 rev/min and 2000 rev/min. Figures 2.17 and 2.18 show the variation in the loads at these engine speeds respectively. FEA was performed at the following crank angles: 24° , 126° , and 360° at each of the above-mentioned speeds. In addition, FEA was also performed at the crank angle of 22° , at which compressive load is maximum and at 371° at which tensile load is maximum at 2000 rev/min. At 4000 rev/min maximum compressive load occurs at 23° and maximum tensile load occurs at 362° . As the engine is cranked, the engine speed is very low and the connecting rod experiences axial load of 21838 N, which constitutes all of the gas load. The stress at any point on the connecting rod at this axial load can be interpolated from the axial stress analysis results. Results of the FEA are discussed in Chapter 4. Tables 2.3, 2.4, and 2.5 list the crank angles at which FEA was performed at 5700 rev/min, 4000 rev/min, and 2000 rev/min, respectively. Parameters that are needed to perform FEA using I-DEAS are also listed in these tables.

These include angular velocity, angular acceleration, linear acceleration of the crank end center, and directions and magnitudes of the loads acting at the connecting rod ends. The pressure constants listed in the tables are the constants defined in Chapter 3 in Equation 3.3 for the cosine distribution of the load, and in Equation 3.6 for uniformly distributed load (UDL). As discussed in Chapter 3, if the axial component of the load at the crank end or pin end was tensile the load was applied with a cosine distribution, while if the axial component of the load was compressive the load was applied with uniform distribution.

Table 2.1: Details of 'slider-crank mechanism-1' used in ADAMS/View –11.

	Crank OA	Connecting Rod AB	Slider B
Calculated Mass (kg)	0.0243	0.0477	0.0156
Calculated Volume (mm ³)	3116	6116	2000
I_{XX} (kg-mm ²)	0.12	0.24	0.26
I_{YY} (kg-mm ²)	21.9	165.4	0.65
I_{ZZ} (kg-mm ²)	21.9	165.4	0.65
I_{XY} (kg-mm ²)	0	0	0
I_{ZX} (kg-mm ²)	0	0	0
I_{YZ} (kg-mm ²)	0	0	0
Length (mm)	100	200	20
Width (mm)	5	5	10
Depth (mm)	6	6	10

Table 2.2: Configuration of the engine to which the connecting rod belongs.

Crankshaft radius	48.5 mm
Connecting rod length	141.014 mm
Piston diameter	86 mm
Mass of the piston assembly	0.434 kg
Mass of the connecting rod	0.439 kg
I_{zz} about the center of gravity	0.00144 kg m ²
Distance of C.G. from crank end center	36.44 mm
Maximum gas pressure	37.29 Bar

Table 2.3: Inputs for FEA of connecting rod using dynamic analysis results at crankshaft speed of 5700 rev/min.

Crank Angle	Ang. Velocity	Ang. Accln	Crank End Load				Piston Pin End Load				Pressure Constant for UDL -(MPa)		Pressure Constant for Cosine Load-(MPa)	
			F _{AX}	F _{AY}	Resultant	Direction	F _{BX}	F _{BY}	Resultant	Direction	Crank End	Pin End	Crank End	Pin End*
deg	rev/s	rev/s ²	N	N	N	deg	N	N	N	deg				
0	-32.7	0	-6832	0	6832	0.0	-1447	0	1447	0.0		3.8	10.6	
24	-30.1	7205	5330	-3698	6487	-34.8	-12744	1405	12821	-6.3	9.1	33.6		
60	-17.1	17119	2174	-6254	6621	-70.8	-5639	1371	5803	-13.7	9.3	15.2		
126	20.0	15699	12736	-7121	14592	-29.2	-8070	2559	8466	-17.6	20.6	22.2		
180	32.7	0	13856	0	13856	0.0	-6929	0	6929	0.0	19.5	18.2		
243	15.6	-17765	9891	7189	12228	36.0	-6037	-2166	6414	19.7	17.2	16.8		
288	-10.7	-19380	-815	5470	5530	-81.5	-964	-107	970	6.3	7.8	2.5		
336	-30.1	-7205	-14997	826	15020	-3.2	7584	1467	7724	10.9			23.4	23.2
360	-32.7	0	-17683	0	17683	0.0	9404	0	9404	0.0			27.5	28.3
396	-32.3	2702	-17485	-212	17487	0.7	9330	-670	9354	-4.1			27.2	28.1
432	-10.7	19380	-1585	-5203	5439	73.1	-194	-159	251	39.4	7.7	0.7		
486	20.0	15699	10275	-6408	12109	-31.9	-5609	1846	5905	-18.2	17.1	15.5		
696	-30.1	-7205	-9625	1585	9755	-9.4	2211	708	2322	17.8			15.2	7.0

Acceleration at the crank end center is 17,280,197 mm/s².

Pressure constant for UDL as defined by Equation 3.6.

Pressure constant for cosine load as defined by Equation 3.3.

* The pressure constants in this column have been corrected for the oil hole.

Table 2.4: Inputs for FEA of connecting rod using dynamic analysis results at crankshaft speed of 4000 rev/min.

Crank Angle	Ang. Velocity	Ang. Accln	Crank End				Piston Pin End				Pressure Constant for UDL -(MPa)		Pressure Constant for Cosine Load-(MPa)	
			F _{AX}	F _{AY}	Resultant	Direction	F _{BX}	F _{BY}	Resultant	Direction	Crank End	Pin End	Crank End	Pin End*
deg	rev/s	rev/s ²	N	N	N	deg	N	N	N	deg				
23	-21.3	3401	13579	-3237	13960	-13.4	-17265	2152	17398	-7.1	19.69	45.60		
24	-21.2	3548	13477	-3354	13888	-14.0	-17128	2225	17272	-7.4	19.59	45.27		
126	14.0	7731	7749	-3934	8691	-26.9	-5451	1688	5707	-17.2	12.26	14.96		
360	-22.9	0	-8366	0	8366	0.0	4289	0	4289	0.0			13.01	12.88
362	-22.9	296	-8406	-26	8406	0.2	4332	-71	4333	-0.9			13.07	13.01

Acceleration at the crank end center is 8,509,792 mm/s².

Pressure constant for UDL as defined by Equation 3.6.

Pressure constant for cosine load as defined by Equation 3.3.

* The pressure constants in this column have been corrected for the oil hole.

Table 2.5: Inputs for FEA of connecting rod using dynamic analysis results at crankshaft speed of 2000 rev/min.

Crank Angle	Ang. Velocity	Ang. Accln	Crank End				Piston Pin End				Pressure Constant for UDL -(MPa)		Pressure Constant for Cosine Load-(MPa)	
			F _{AX}	F _{AY}	Resultant	Direction	F _{BX}	F _{BY}	Resultant	Direction	Crank End	Pin End	Crank End	Pin End*
deg	rev/s	rev/s ²	N	N	N	deg	N	N	N	deg				
22	-10.7	813	19636	-2886	19847	-8.4	-20565	2626	20732	-7.3	27.99	54.34		
24	-10.6	887	19405	-3104	19652	-9.1	-20318	2822	20513	-7.9	27.72	53.77		
126	7.0	1933	4120	-1616	4425	-21.4	-3545	1054	3699	-16.6	6.24	9.69		
360	-11.5	0	-1586	0	1586	0.0	566	0	566	0.0			2.47	1.70
371	-11.3	407	-1684	-62	1685	2.1	687	-70	691	-5.8			2.62	2.07

Acceleration at the crank end center is 2,127,448 mm/s².

Pressure constant for UDL as defined by Equation 3.6.

Pressure constant for cosine load as defined by Equation 3.3.

* The pressure constants in this column have been corrected for the oil hole.

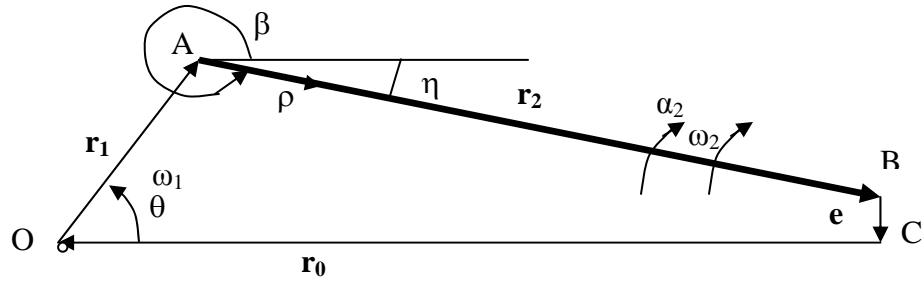
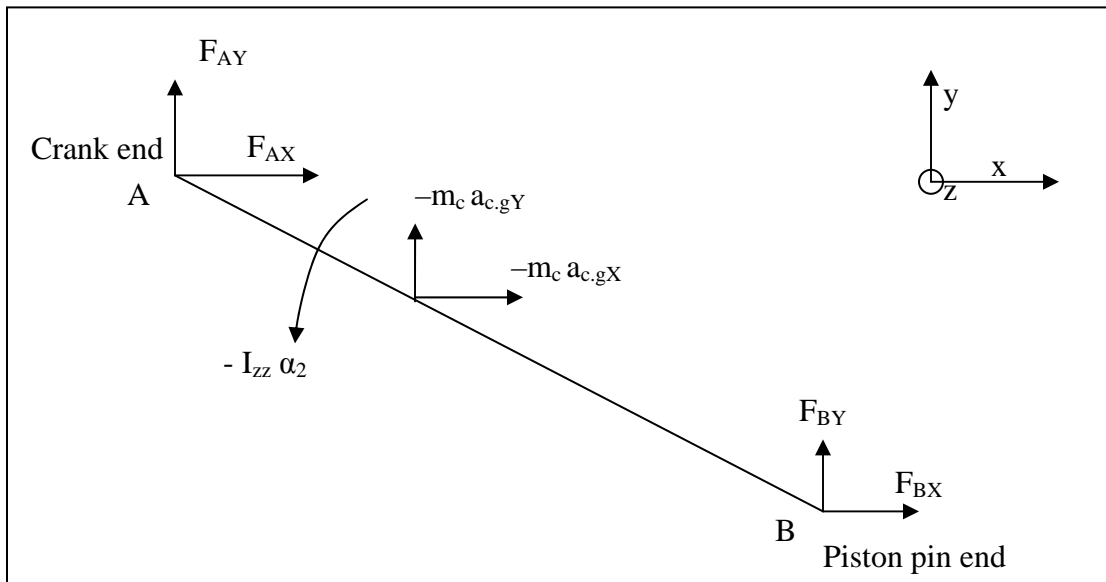
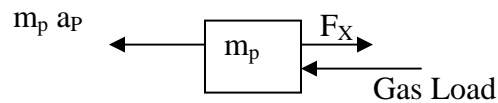


Figure 2.1: Vector representation of slider-crank mechanism.



(a)



(b)

Figure 2.2: Free body diagram and vector representation. (a) Free body diagram of connecting rod. (b) Free body diagram of piston.

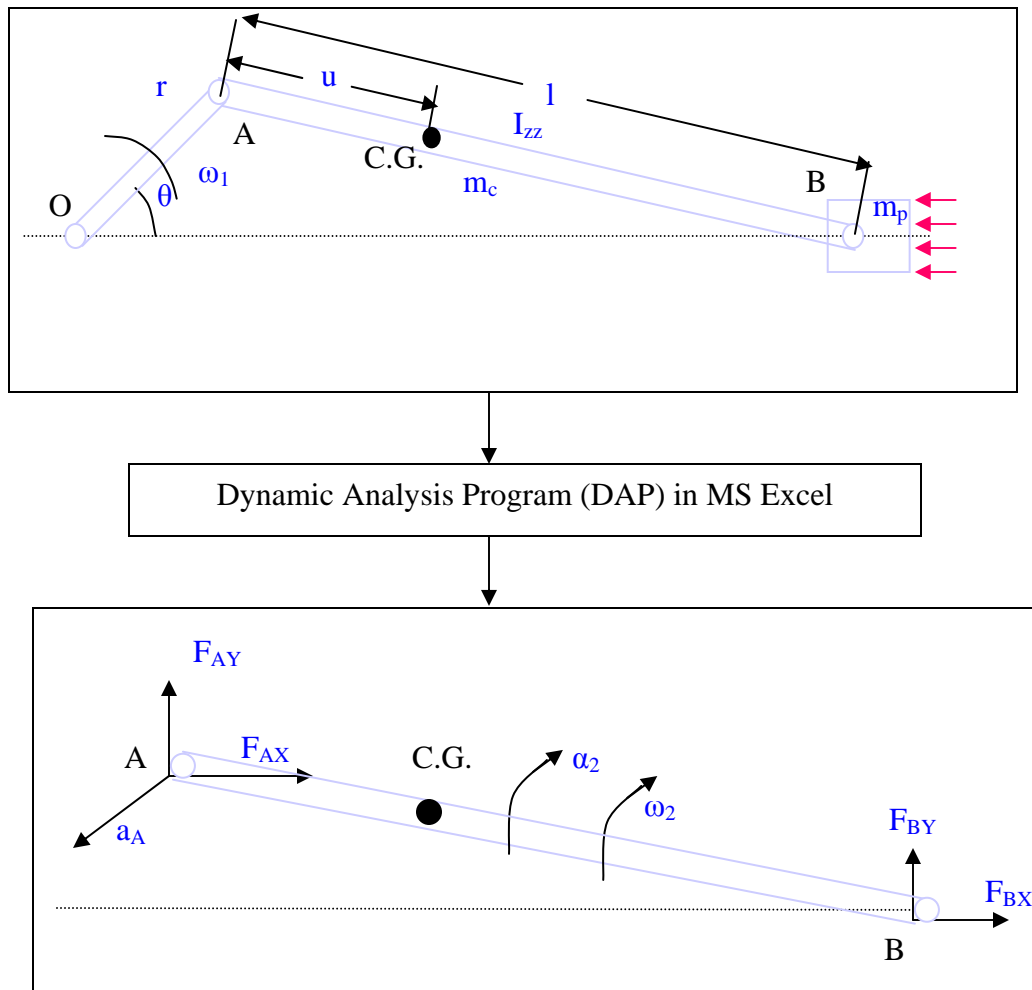


Figure 2.3: Typical input required for performing load analysis on the connecting rod and the expected output.

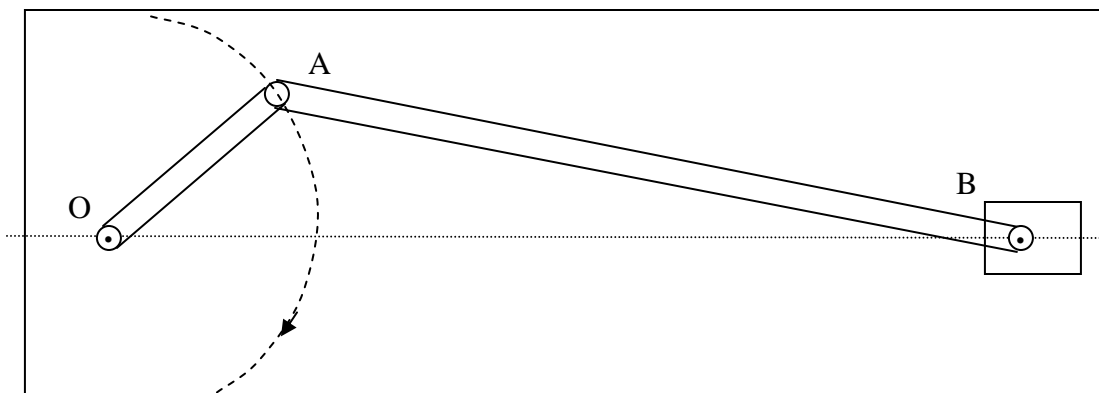


Figure 2.4: 'Slider-crank mechanism -1'.

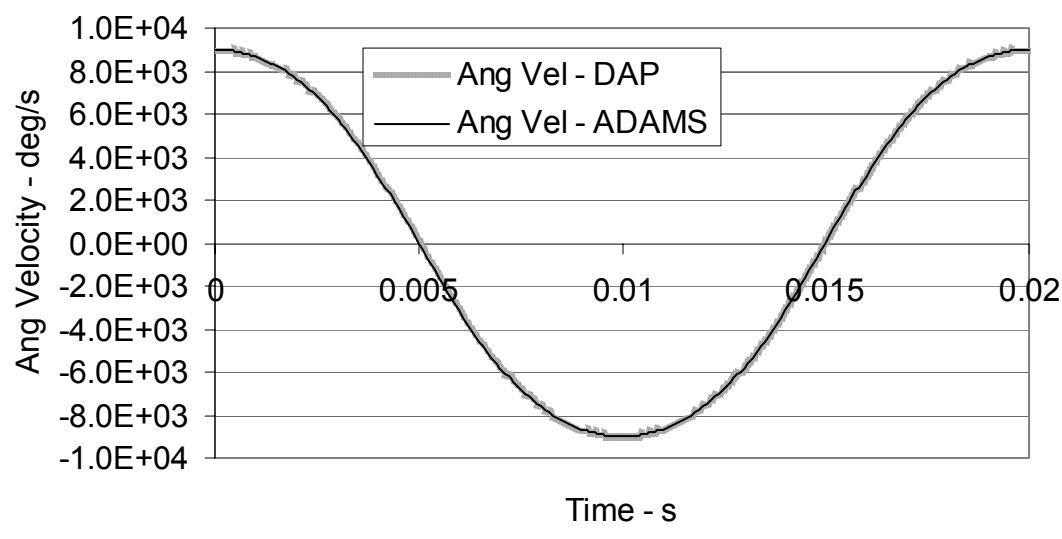


Figure 2.5: Angular velocity of link AB for 'slider-crank mechanism-1'- A comparison of the results obtained by DAP and ADAMS/View-11 at 3000 rev/min crank speed (clockwise).

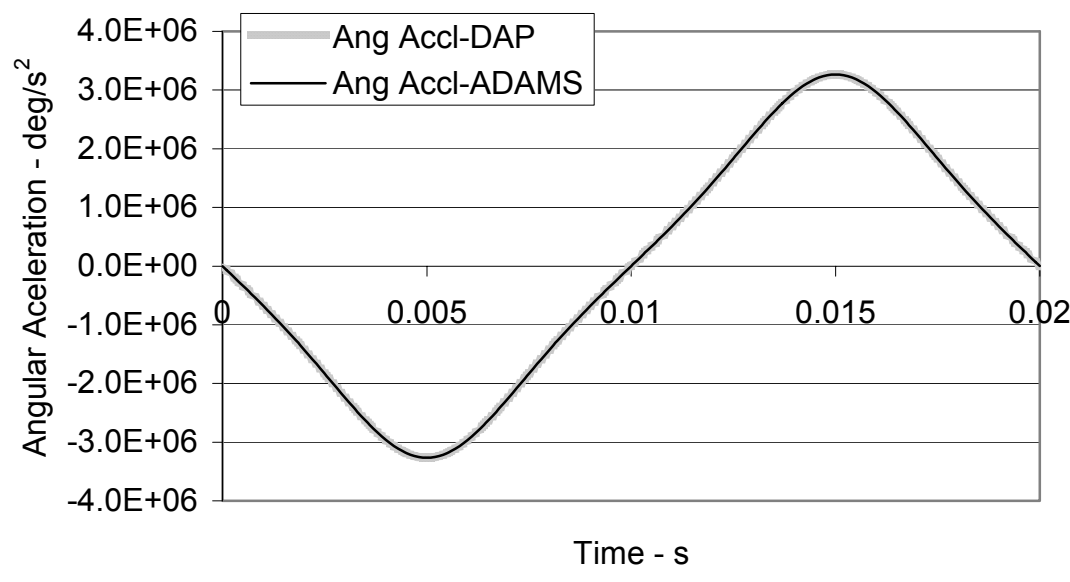


Figure 2.6: Angular acceleration of link AB for 'slider-crank mechanism-1'- A comparison of the results obtained by DAP and ADAMS/View-11 at 3000 rev/min crank speed (clockwise).

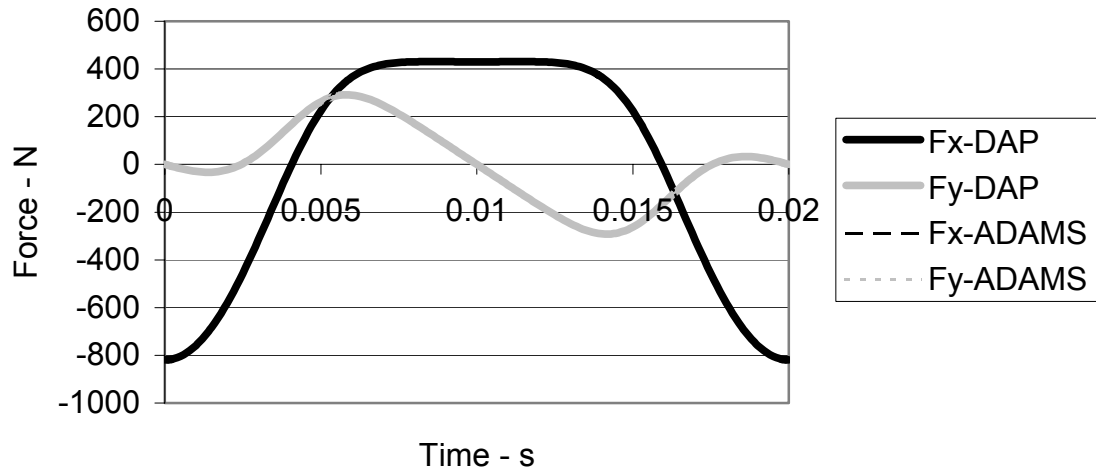


Figure 2.7: Forces at the joint A, for 'slider-crank mechanism-1'- A comparison of the results obtained by DAP and ADAMS/View-11 at 3000 rev/min crank speed. Fx corresponds to F_{AX} and Fy corresponds to F_{AY} .

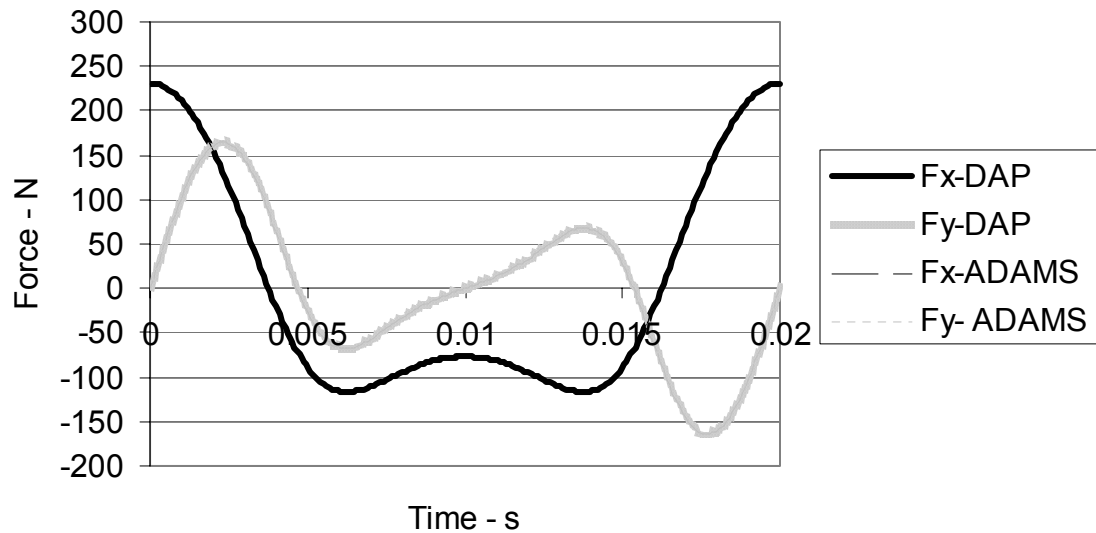


Figure 2.8: Forces at the joint B for 'slider-crank mechanism-1'- A comparison of the results obtained by DAP and ADAMS/View-11 at 3000 rev/min crank speed. Fx corresponds to F_{BX} and Fy corresponds to F_{BY} .

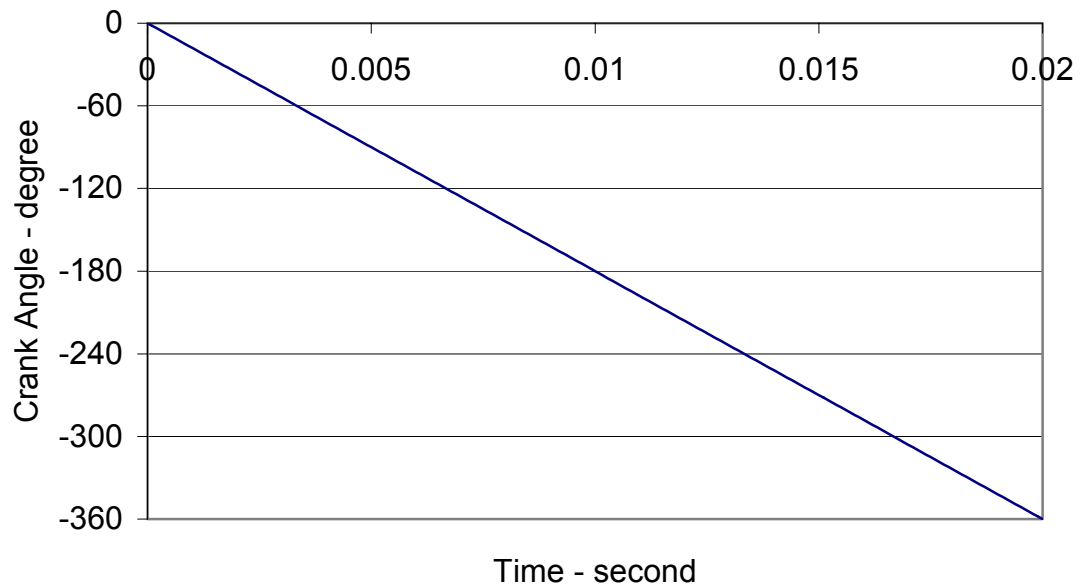


Figure 2.9: Variation of crank angle with time at 3000 rev/min crank speed in clockwise direction.

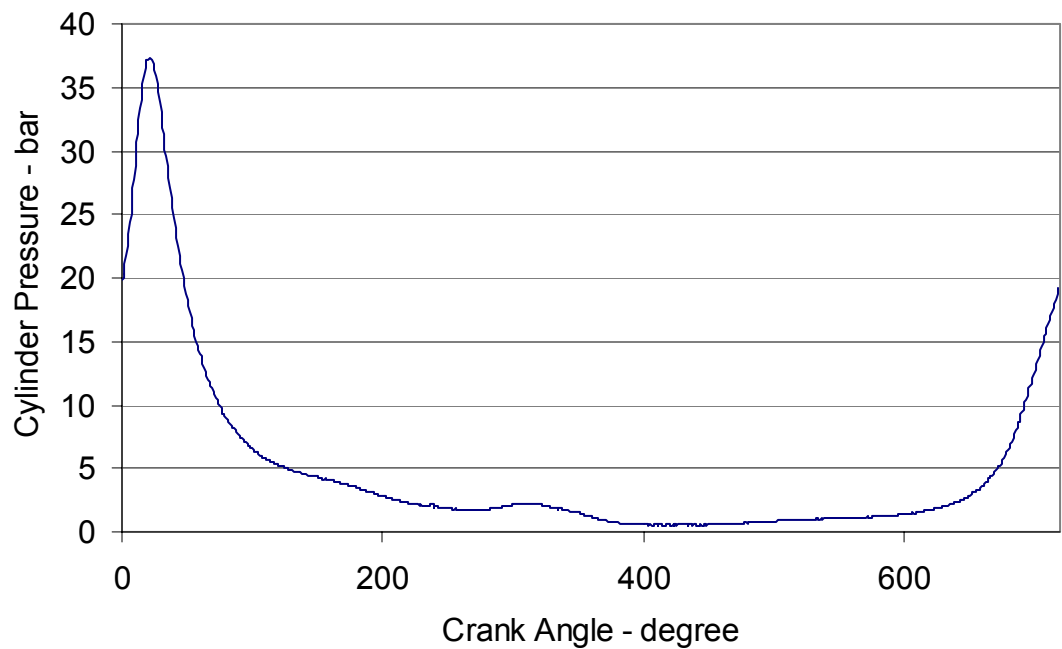


Figure 2.10: Pressure crank angle diagram used to calculate the forces at the connecting rod ends.

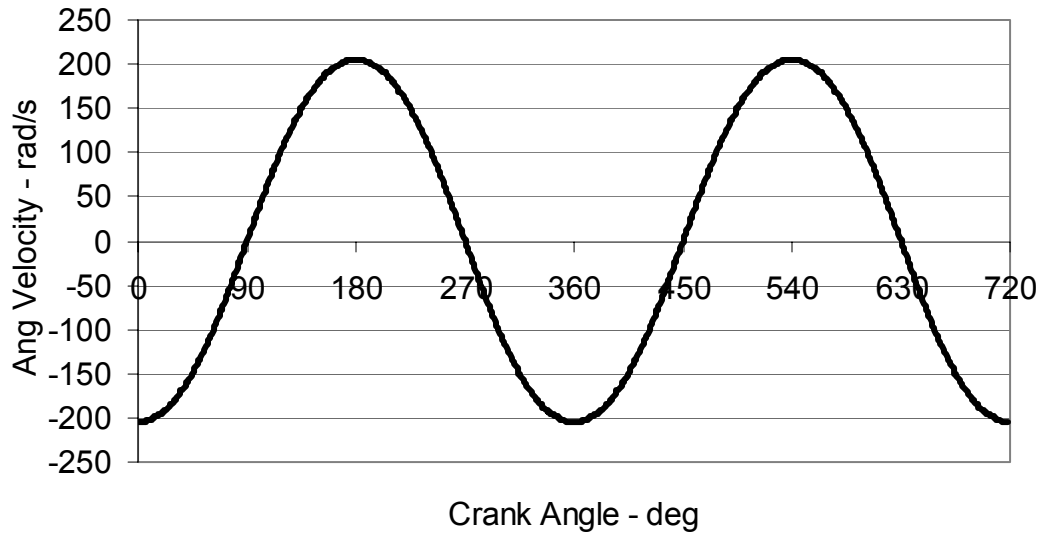


Figure 2.11: Variation of angular velocity of the connecting rod over one complete engine cycle at crankshaft speed of 5700 rev/min.

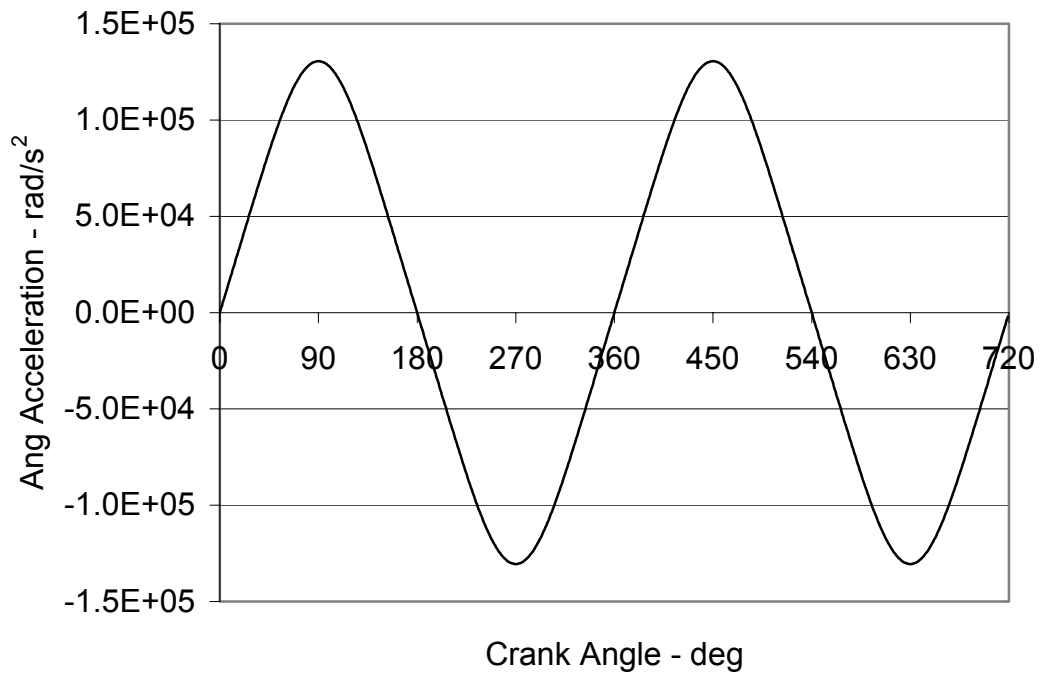


Figure 2.12: Variation of angular acceleration of the connecting rod over one complete engine cycle at crankshaft speed of 5700 rev/min.

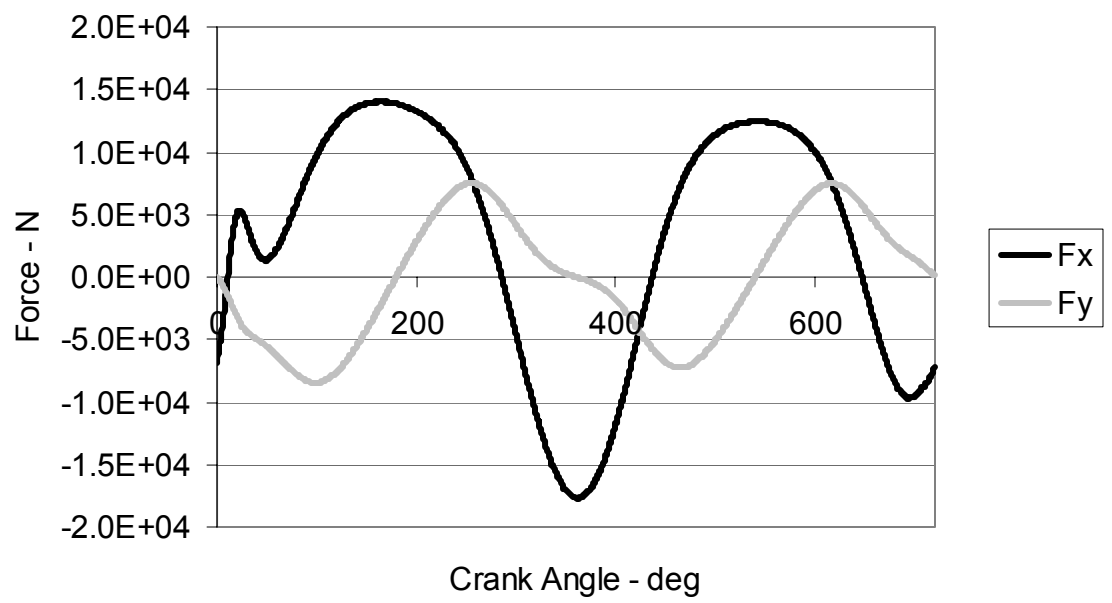


Figure 2.13: Variations of the components of the force over one complete cycle at the crank end of the connecting rod at crankshaft speed of 5700 rev/min. Fx corresponds to F_{AX} and Fy corresponds to F_{AY} .

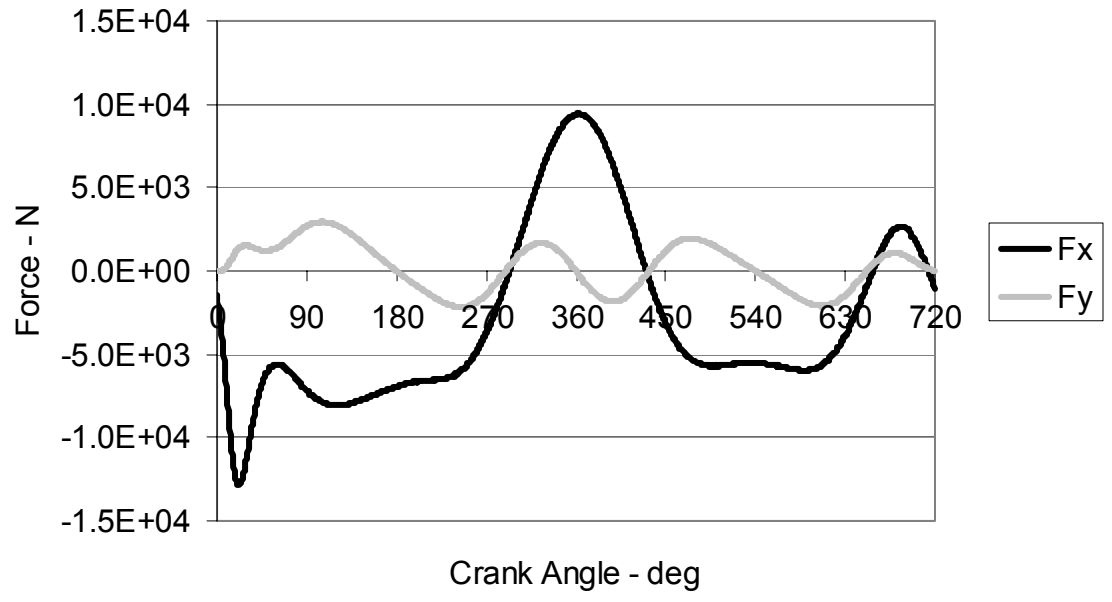


Figure 2.14: Variations of the components of the force over one complete cycle at the piston pin end of the connecting rod at crankshaft speed of 5700 rev/min. Fx corresponds to F_{BX} and Fy corresponds to F_{BY} .

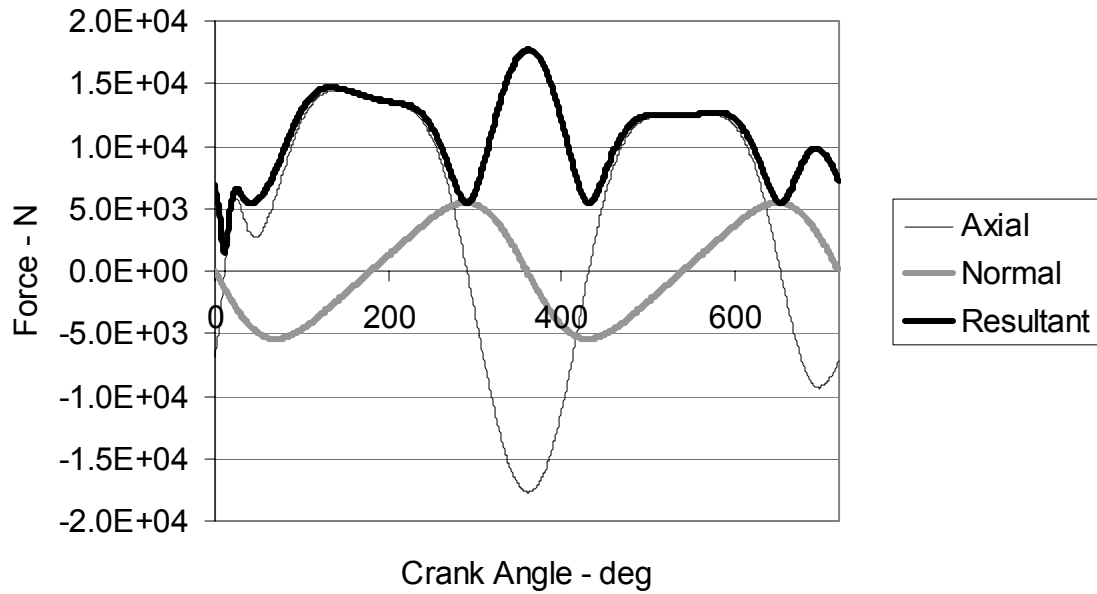


Figure 2.15: Axial, normal, and the resultant force at the crank end at crank speed of 5700 rev/min.

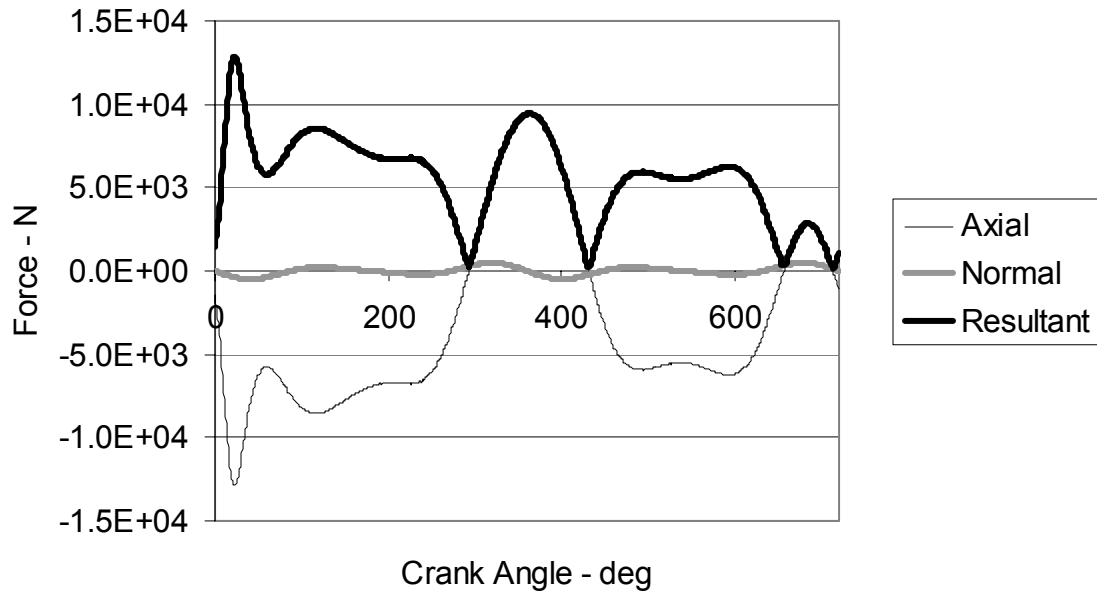


Figure 2.16: Axial, normal, and the resultant force at the piston-pin end at crank speed of 5700 rev/min.

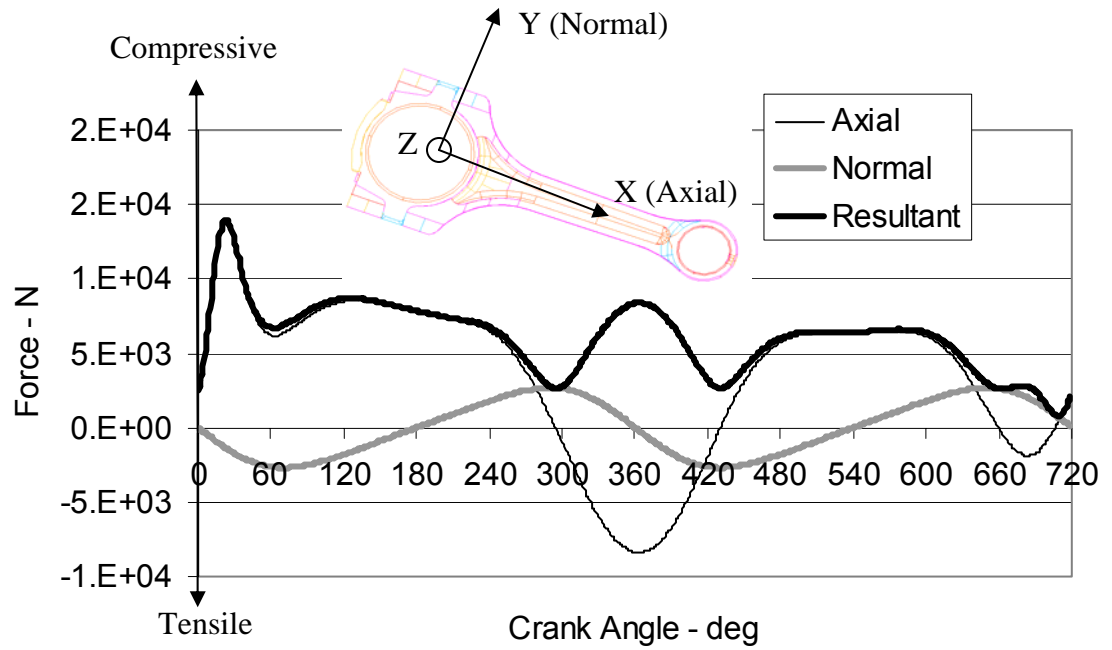


Figure 2.17: Variation of the axial, normal (normal to connecting rod axis), and the resultant force at the crank end at crank speed of 4000 rev/min.

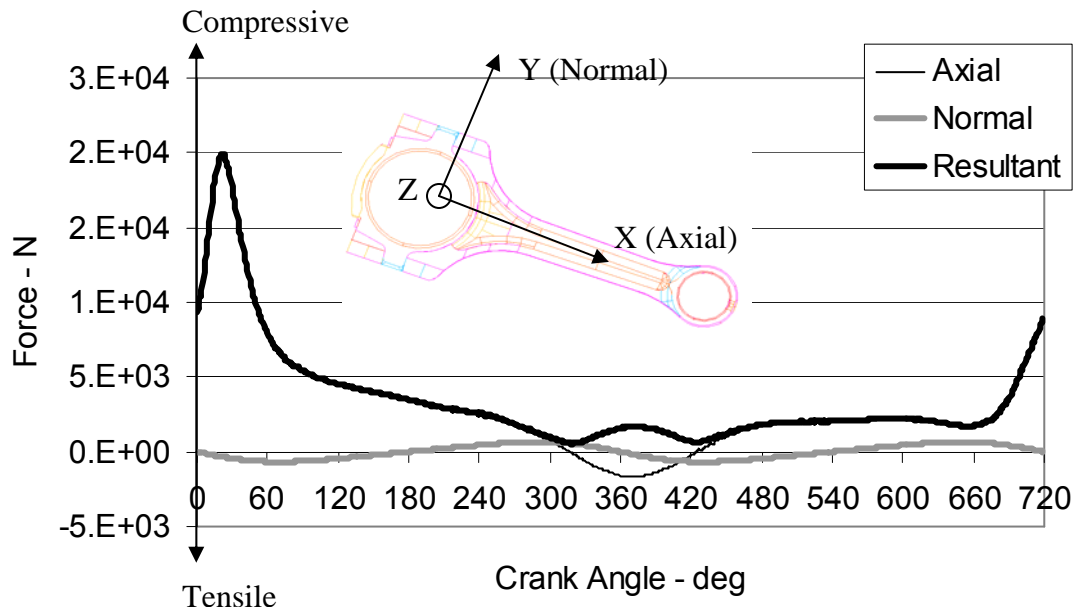


Figure 2.18: Variation of the axial, normal (normal to connecting rod axis), and the resultant force at the crank end at crank speed of 2000 rev/min.

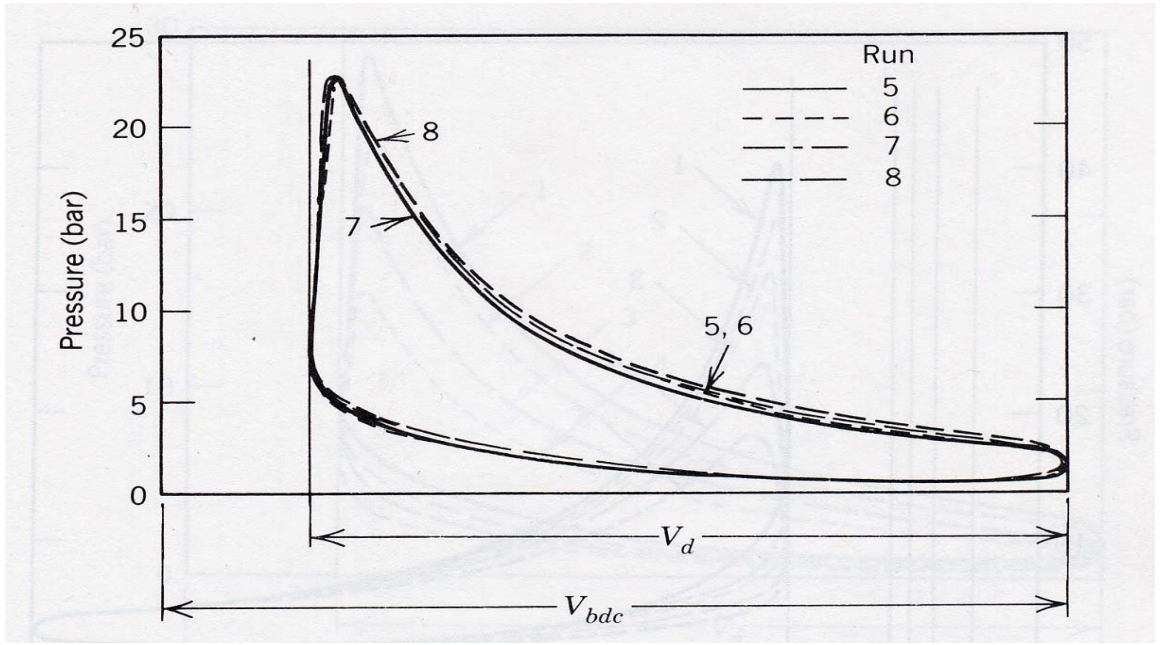


Figure 2.19: Effect of speed on P-V diagram at constant delivery ratio. Curve 5 is for 900 rev/min, curve 6 for 1200 rev/min, curve 7 for 1500 rev/min, and curve 8 for 1800 rev/min (Ferguson, 1986).

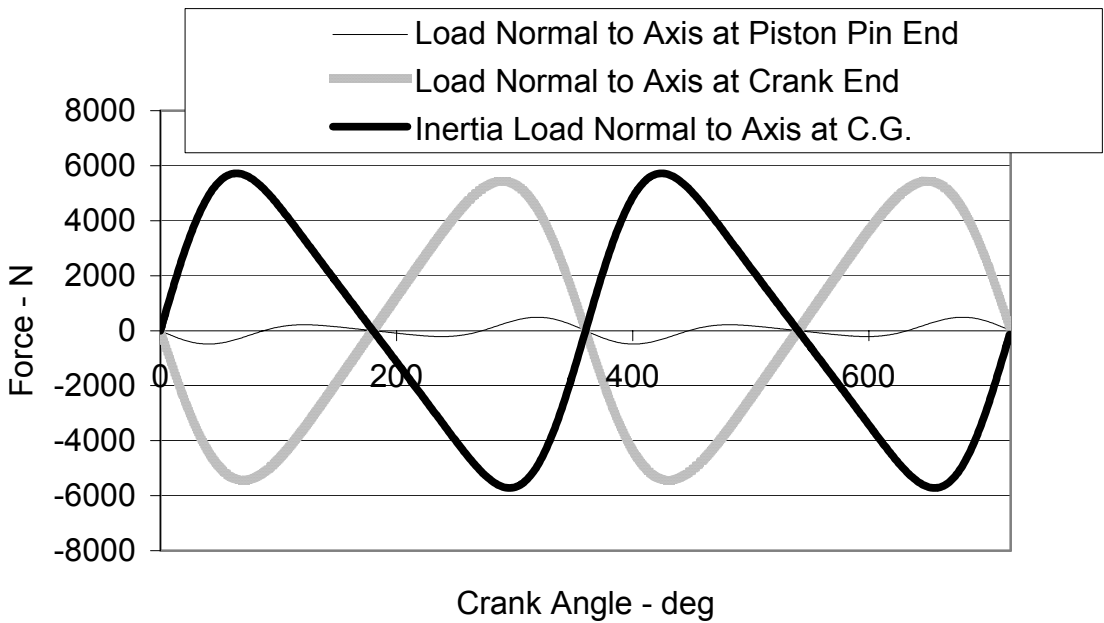


Figure 2.20: Loads normal to the connecting rod axis. Note that variations from 0° to 360° repeat from 360° to 720°.

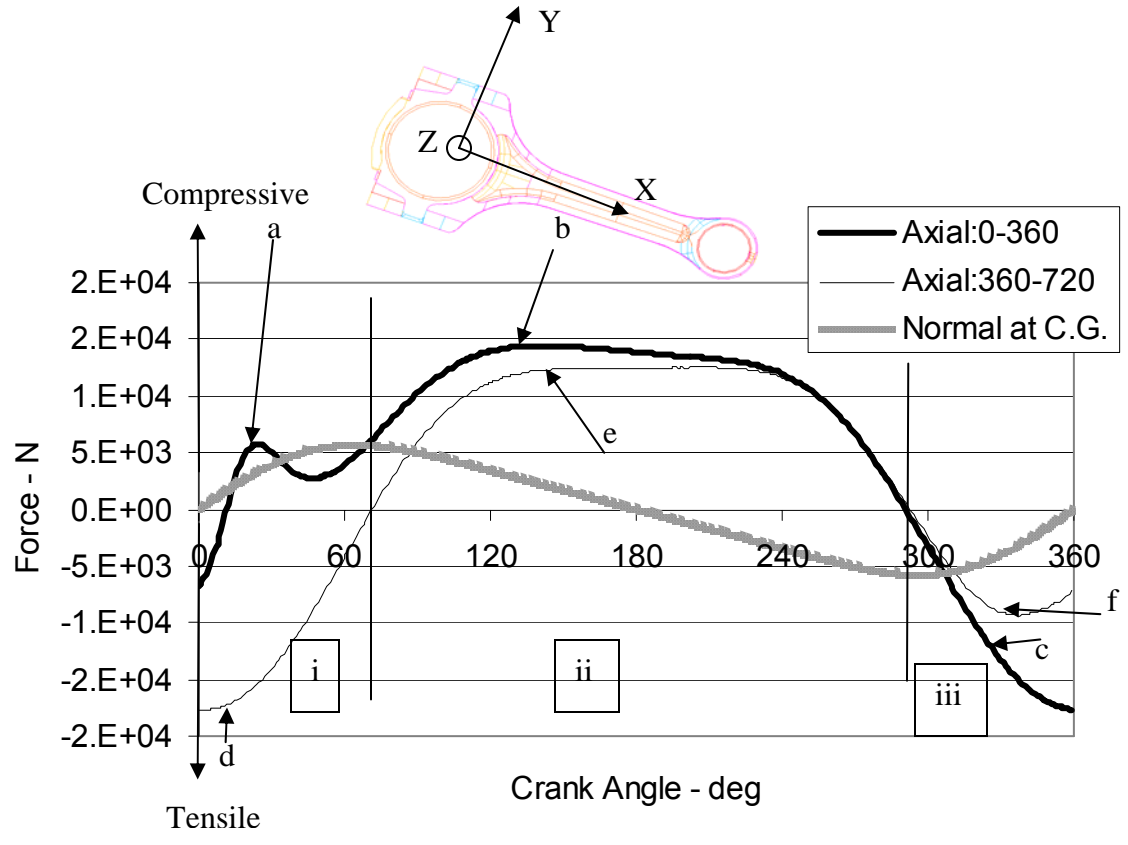


Figure 2.21: Variation of the axial load at the crank end and the load normal to connecting rod length at the C.G. at 5700 rev/min crankshaft speed. The 360° to 720° variation has been superimposed on 0° to 360° variation. Plot has been divided into three regions: i, ii and iii.

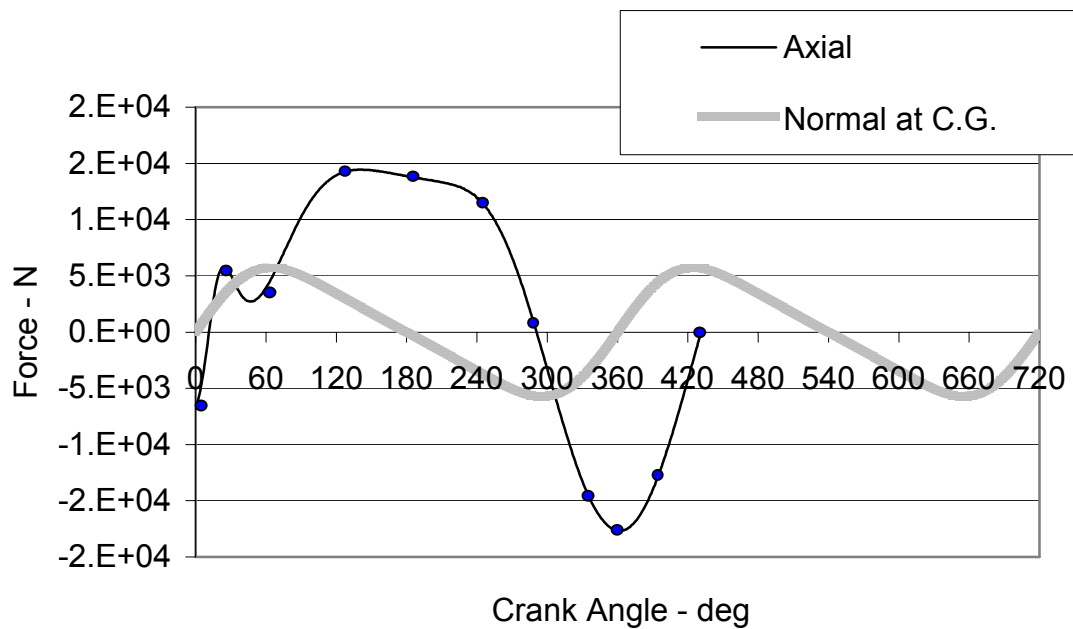


Figure 2.22: Variation of load at the crank end over the portion of the cycle that will need FEA at 5700 rev/min crankshaft speed. Markers on the curve represent crank angles at which FEA has been performed.

3. FE MODELING OF THE CONNECTING ROD

This chapter discusses geometry of connecting rod used for FEA, its generation, simplifications and accuracy. Mesh generation and its convergence is discussed. The load application, particularly the distribution at the contact area, factors that decide load distribution, the calculation of the pressure constants depending on the magnitude of the resultant force, application of the restraints and validation of the FEA model are also discussed. Three FEM were used to determine structural behavior under three different conditions, namely, static load condition (static FEA), service operating condition (quasi-dynamic FEA) and test condition (test assembly FEA). These finite element models are also discussed in this chapter.

3.1 GEOMETRY OF THE CONNECTING ROD

The connecting rod was digitized using a coordinate measuring machine. A solid model of the connecting rod, as shown in Figure 3.1, was generated using I-DEAS Master Modeler. For FEA, the flash along the entire connecting rod length including the one at the oil hole was eliminated in order to reduce the model size. The flash runs along the length of the connecting rod and hence does not cause stress concentration under axial loading. The flash is a maximum of about 0.15 mm thick. Even under bending load the flash can be eliminated especially when we consider the fact that the solution time will increase drastically if we do model this feature, and very little increase in strength can be

expected. This is due to the fact that the flash being 0.15 mm thick will drastically increase the model size, if it is modeled. The connecting rod geometry used for FEA can be seen in Figure 3.2. Note that the flash and the bolt-holes have been eliminated. The cross section of the connecting rod from failed components reveals that the connecting rod, as manufactured, is not perfectly symmetric. In the case of one connecting rod, the degree of non-symmetry in the shank region, when comparing the areas on either side of the axis of symmetry perpendicular to the connecting rod length and along the web, was about 5%. This non-symmetry is not the design intent and is produced as a manufacturing variation. Therefore, the connecting rod has been modeled as a symmetric component.

The connecting rod weight as measured on a weighing scale is 465.9 grams. The difference in weight between the weight of the solid model used for FEA and the actual component when corrected for bolt head weight is less than 1%. This is an indication of the accuracy of the solid model.

3.2 MESH GENERATION

Static FEA

Finite element mesh was generated using parabolic tetrahedral elements with various element lengths of 2.5 mm (20719 elements), 2 mm (37373 elements), 1.5 mm (77316 elements), and 1 mm (226409 elements). The von Mises stress was checked for convergence at ten locations, as shown in Figure 3.3. The results are plotted in Figure 3.4. For most areas on the connecting rod convergence has been achieved with 1.5 mm uniform element length. This is evident for all locations, except 9, in Figure 3.4. Therefore, a finite element mesh was generated with a uniform global element length of

1.5 mm, and at locations with chamfers a local element length of 1 mm was used. This resulted in a mesh with 104471 elements. Further refinement was done locally by using element length of 0.8 mm (128954 elements). It can be seen that convergence has been achieved with 1 mm local mesh size. The maximum percentage difference between the stress values observed between the last two models (the one with 104471 elements and the one with 128954 elements) is 2.3%, which is small. Hence, the mesh with 104471 elements was used for FEA.

Quasi-Dynamic FEA

The same mesh that was used for static FEA, as presented in the section above, was also used for quasi-dynamic FEA. Convergence was checked at locations where high bending stresses are expected. In this case they were checked at locations 12 and 13, about 87.6 mm from crank end center, as shown in Figure 3.5. As discussed in Chapter 4, locations 12 and 13 (with reference to Figure 3.5) experience considerably high bending stresses. Figure 3.6 indicates that convergence of stress σ_{xx} was achieved with a mesh that uses 1.5 mm uniform global element length and 1 mm local element length.

Test Assembly FEA

The mesh used for static FEA used 1.5 mm global element length and 1 mm local element length at chamfers. The mesh used for assembly FEA was even finer. The mesh was generated with an element length of 1 mm between the ends of the connecting rod and 1.5 mm at the cap. Since convergence was checked for the mesh used in static FEA

and the mesh used in this case was finer, there was no need to check the convergence again.

3.3 BOUNDARY CONDITIONS

3.3.1 Loading

Static FEA

The crank and piston pin ends are assumed to have a sinusoidal distributed loading over the contact surface area, under tensile loading, as shown in the Figure 3.7. This is based on experimental results (Webster *et al.* 1983). The normal pressure on the contact surface is given by:

$$p = p_o \cos \Theta \quad (3.1)$$

The load is distributed over an angle of 180° . The total resultant load is given by:

$$P_t = \int_{-\pi/2}^{\pi/2} p_o (\cos^2 \Theta) r t d\Theta = p_o r t \pi / 2 \quad (3.2)$$

Figure 3.8 describes r , t and Θ . The normal pressure constant p_o is, therefore, given by:

$$p_o = P_t / (r t \pi / 2) \quad (3.3)$$

The tensile load acting on the connecting rod, P_t , can be obtained using the expression from the force analysis of the slider crank mechanism. This is discussed in detail in Chapter 2.

For compressive loading of the connecting rod, the crank and the piston pin ends are assumed to have a uniformly distributed loading through 120° contact surface, as shown in Figure 3.9 (Webster *et al.* 1983). The normal pressure is given by:

$$p = p_o \quad (3.4)$$

The total resultant load is given by:

$$P_c = \int_{-\pi/3}^{\pi/3} p_o (\cos \Theta) r t d\Theta = p_o r t \sqrt{3} \quad (3.5)$$

The normal pressure constant is then given by:

$$p_o = P_c / (r t \sqrt{3}) \quad (3.6)$$

P_c can be obtained from the indicator diagram, such as the one shown in Figure 3.10, of an engine.

In this study four finite element models were analyzed. FEA for both tensile and compressive loads were conducted. Two cases were analyzed for each case, one with load applied at the crank end and restrained at the piston pin end, and the other with load applied at the piston pin end and restrained at the crank end. In the analysis carried out, the axial load was 26.7 kN (6 kips) in both tension and compression. The pressure constants for 26.7 kN are as follows:

Compressive Loading:

$$\text{Crank End: } p_o = 26700 / (24 \times 17.056 \times \sqrt{3}) = 37.66 \text{ MPa}$$

$$\text{Piston pin End: } p_o = 26700 / (11.97 \times 18.402 \times \sqrt{3}) = 69.98 \text{ MPa}$$

Tensile Loading:

$$\text{Crank End: } p_o = 26700 / [24 \times 17.056 \times (\pi/2)] = 41.5 \text{ MPa}$$

$$\text{Piston pin End: } p_o = 26700 / [11.97 \times 18.402 \times (\pi/2)] = 77.17 \text{ MPa}$$

Since the analysis is linear elastic, for static analysis the stress, displacement and strain are proportional to the magnitude of the load. Therefore, the obtained results from FEA readily apply to other elastic load cases by using proportional scaling factor.

Quasi-Dynamic FEA

While performing quasi-dynamic FEA of the connecting rod, the external loads consisting of reactions or the loads computed at the connecting rod ends in the previous chapter, were applied to both crank end and the piston pin end of the connecting rod. The angular velocity, angular acceleration, and linear acceleration were specified in both magnitude and direction for the connecting rod. All the above-mentioned quantities are for the crank angle of interest. The center of rotation about which they were calculated was also specified. The inertia and dynamic loads were calculated and applied internally by the software (I-DEAS) based on these inputs. This ensures that the loads applied form a set of completely equilibrated internal and external loads.

While applying the loads, the manner in which loads were applied for axial static FEA was extended to the case of quasi-dynamic FEA. If the component of the resultant force along the connecting rod length suggested a tensile load to act on the connecting rod, the resultant load was applied with cosine distribution. The cosine distribution was applied 90° on either side of the direction of the resultant load, totally 180° . But if the component of the resultant force along the connecting rod length suggested a compressive load to act on the connecting rod, the resultant load was applied with uniform distribution. The uniformly distributed load was applied 60° on either side of the direction of the resultant load, totally 120° . The results at the regions near the ends of the connecting rod are sensitive to the type of load distribution used (uniformly distributed or cosine distribution). At the crank end transition, however, the stresses differed only by 7% at the crank angle of 432° , when the load distribution was changed from cosine to

UDL. Detailed investigation of the actual load distribution was beyond the scope of this work. Therefore, the method of load distribution suggested by Webster *et al.* (1983) was used.

An example will clarify the boundary conditions further. From Table 2.3, consider crank angle 432° as an example. The application of boundary condition at this crank angle has been illustrated in Figure 3.11. The computed direction of the resultant load at the crank end is 73.1° . Therefore, 120° of the surface of the crank end (60° on either side of this direction) carried a uniformly distributed load with a pressure of 7.7 MPa. Since the axial components of the load are compressive, loads were applied with uniform distribution. The resultant of this uniformly distributed compressive load is 5439 N. The direction of the resultant load at the piston pin end is 39.4° . Therefore, 120° of the surface of the pin end (60° on either side of this direction) will carry a uniformly distributed load with a pressure of 0.7 MPa. The resultant of this uniformly distributed compressive load is 251 N. To account for the dynamic motion of the connecting rod and the resulting inertia loads, the acceleration boundary conditions are imposed. The translational acceleration of $17,280,197 \text{ mm/s}^2$ in the direction of the crank towards the crank center, angular velocity of -10.7 rev/s (units used in I-DEAS), and angular acceleration of $19,380 \text{ rev/s}^2$ (vector direction normal to the connecting rod plane) are imposed on the connecting rod. The crank end center is specified as the center of rotation.

As a second example, consider the crank angle 396° from Table 2.3. The axial components of the loads at both the crank and pin ends are tensile. Therefore, the load was applied with cosine distribution at both the ends. At the crank end, 90° on either side of the direction of 0.7° (totally 180°) carried the load with a pressure of 27.2 MPa

distributed as a cosine function. The resultant of this load was 17487 N. Similarly, at the pin end, 90° on either side of the direction of -4.1° (totally 180°) carried the load with a pressure of 28.1 MPa distributed as a cosine function. The resultant of the load was 9354 N. In addition, to account for the dynamic motion of the connecting rod and the resulting inertia loads, the acceleration boundary conditions were imposed. The translational acceleration of $17,280,197 \text{ mm/s}^2$, angular velocity of -32.3 rev/s and angular acceleration of 2702 rev/s^2 are imposed on the connecting rod. The crank end center is specified as the center of rotation.

Test Assembly FEA

This FEA was carried out to simulate the fatigue test conditions. The testing was carried out at $R = -1.25$ where $R = P_{\min} / P_{\max}$, at three load levels. The tensile load used in this FEA was 44.5 kN, which was applied in the direction along the length of the connecting rod. This load was applied directly to the pins attached to the connecting rod at the piston pin end, as a uniformly distributed load. The compressive load used, 55.6 kN, was also applied in the direction along the length of the connecting rod. Contact elements were used between the connecting rod and the pins. Friction between the pins and the connecting rod was also taken into account (coefficient of friction = 0.42). The pins were press fitted into the connecting rod with no bearings being used, while testing. The diametral interference between the pins and the connecting rod was $1/1000^{\text{th}}$ of an inch i.e 0.0254 mm. The interference between the connecting rod and pins was also taken into account in the finite element model. The interference was approximated by applying the pressure on the surface of the connecting rod crank end and pin end bores. The

pressure is computed using the press fit theory of machine design (Shigley and Mischke, 1989). The pressure was however not applied to the interface region of pins, as the stress distribution in the pins is not of interest. Assuming the pin to be of the same material as the connecting rod (i.e. both steel) the contact pressure is given by:

$$p = \frac{E\delta(r_o^2 - R^2)(R^2 - r_i^2)}{2R^3(r_o^2 - r_i^2)} \quad (3.7)$$

At the crank end $R = 24$ mm, $r_i = 0$, $r_o = 28.55$ mm (approximation), $E = 206700$ MPa, and $\delta = 0.0254/2 = 0.0127$ mm. Using these values in Equation 3.7, the contact pressure is 16.04 MPa. At the pin end $R = 11.97$ mm, $r_i = 0$, $r_o = 15.32$ mm (approximation), $E = 206700$ MPa, and $\delta = 0.0127$ mm. Using these values the contact pressure is 42.69 MPa.

3.3.2 Restraints

Static FEA

As already mentioned, four FEA models were solved. Figure 3.12 shows a FEA model in which tensile load is applied at the crank end and the piston pin end is restrained. Note that half of the piston pin inner surface (180°) is completely restrained (180° of contact surface area is totally restrained, i.e X, Y, Z translations of all the nodes on this surface are set to zero if the connecting rod is in tension).

Similarly, when the connecting rod is under axial compressive load, 120° of contact surface area is totally restrained. Figure 3.13 shows FEA model in which compressive load is applied at the crank end and piston pin end is completely restrained.

Quasi-Dynamic FEA

If restraints and forces are both applied to a surface, force will not be transmitted in the direction in which the restraints are applied. This presents a problem in simulating a pin joint. A way to simulate the pin joint is to apply all the loads acting on the connecting rod that keep the connecting rod in dynamic equilibrium at the instant under consideration (i.e. at a specific crank angle) and then solve the model. Therefore, no restraints were applied to the model while solving for the case of quasi-dynamic FEA. The finite element model was solved by eliminating the rigid body motion, achieved by specifying kinematic degrees of freedom and specifying elimination of rigid body motion while solving, as opposed to applying restraints. Not applying restraints and using loads at both ends of the connecting rod permits better representation of the loads transferred through the pin joints.

Test Assembly FEA

The restraints were applied to the pin at the crank end. All degrees of freedom were restrained. The FEA model is shown in Figure 3.14. Since the restraints were applied to the pin rather than the connecting rod, the structural behaviour at even the crank end of the connecting rod predicted by this FE model can be expected to be accurate.

3.4 VALIDATION OF FEA MODELS

Static FEA

The properties of the material used for linear elastic finite element analysis are listed in Table 3.1. In order to validate the FEA model, the stresses in the shank region half way along the length of the connecting rod were compared under two conditions of compressive load application. First, a 26.7 kN uniformly distributed load was applied at the piston pin end, while the crank end was restrained. Second, a 26.7 kN uniformly distributed load was applied at the crank end, while the piston pin end was restrained. Since the magnitude of the loads are identical under the two conditions, we can expect the stresses to be same at a location away from the loading and restraints (i.e mid-span) under the two conditions. A similar comparison was also made for tensile load application. However, in this case the load distribution on the surface was cosine. The results are tabulated in Table 3.2. There is very good agreement for the compressive load. Under tensile load conditions, the stresses differ by a maximum of 2.7% at the same locations. Two nodes were picked from the flanges and one on the web of the connecting rod. The locations of the nodes are shown in Figure 3.15. The fact that stresses are identical at nodes 37478 and 32302, see Table 3.2, also validates the FEA model since these are nodes symmetric in their position on the flange, with respect to the connecting rod axis.

Strain gage measurements were also made on a connecting rod under tensile as well as compressive loads. A comparison of the FEA predictions with the strain gage measurements is in order. At a distance of 57.8 mm as shown in Figure 3.16, the location

of the strain gages, the average strain gage reading from four strain gages was -486 microstrain under a compressive load of 3000 lbs, and 473 microstrain under a tensile load of 3000 lbs. The results are tabulated in Table 3.3.

Two sets of FEA results are tabulated, FEA-I and FEA-II. FEA-I used a FE model that included the connecting rod, the pins at the crank and piston pin ends, the interference fit between pins and the connecting rod, and contact elements. This model is referred to in this thesis as ‘test assembly FEA’. This model very much simulated the testing condition. Testing has been described by Afzal (2004). FEA-II used a FE model that included only the connecting rod. The loads and restraints were applied as described in Sections 3.3.1 and 3.3.2 for static FEA. The theoretically predicted strain is also tabulated, calculated as $\epsilon_{xx} = (F/AE) * 10^6$. The cross sectional area at 57.8 mm from crank end center is 133.7 mm^2 . Note that the strain gages are located at the fatigue critical location, near the crank end transition.

From Table 3.3, it is clear that the differences are small and there is very good agreement between the experimental results and FEA results. This verifies the accuracy of the modeled geometry, as well as the convergence of the FE mesh. In addition, it indicates that in the shank region the structural behavior of the connecting rod is independent of the way the load is applied at the ends. The two FE models differed in the way the load was applied. FEA-I load was applied through the pins, and FEA-II load was applied directly on the inner bore of the ends.

Quasi-Dynamic FEA

After solving the quasi-dynamic FEA model in I-DEAS, the “.lis” file for this model lists the loads as follows:

“NET APPLIED LOAD:

$FX = -0.33 \text{ N}$, $FY = -0.29 \text{ N}$, $FZ = 0 \text{ N}$

$MX = 0 \text{ N-mm}$, $MY = 0 \text{ N-mm}$, $MZ = -125.8 \text{ N-mm}$ ”

Here, FX, FY and FZ represent net applied loads (sum of all the loads) in X, Y and Z directions, respectively, and MX, MY, MZ represent moments about X, Y, and Z directions, respectively. FX and FY are very small as compared to the applied loads and so is MZ. They are not zero due to round off errors. This indicates that the connecting rod is in fact in static equilibrium under the effect of the applied loads. This validates the FEA model. This kind of validation was done for every quasi-dynamic FEA model solved.

Test Assembly FEA

The section discussing the validation of static FEA model also discussed validation of test assembly FEA, with reference to the results in Table 3.3. As indicated, there is very good agreement between the FEA results and the strain gage measurements.

Table 3.1: Properties of connecting rod material.

Material Property	Unit	Scalar Value
Modulus of Elasticity	GPa	206.7
Poisson's Ratio	Unitless	0.30
Mass Density	kg/m ³	7820

Table 3.2: von Mises stresses in the shank region under tensile and compressive loads.

Tensile Load = 26.7 kN				Compressive Load = 26.7 kN		
NL	Load at Crank End	Load at Piston End	%Diff	Load at Crank End	Load at Piston End	%Diff
	von Mises Stress (MPa)	von Mises Stress (MPa)		von Mises Stress (MPa)	von Mises Stress (MPa)	
37478	196.5	192.9	1.8	197.1	197.3	-0.1
5613	205.0	199.4	2.7	202.9	202.0	0.4
32302	196.5	192.9	1.8	197.1	197.3	-0.1

NL: Node label. Nodes are shown in Figure 3.15.

Table 3.3: Measured and predicted strains. Locations of strain gages are shown in Figure 3.16. Measured strain is the average of four gages.

Load	Measured Strain (μ strain)	FEA-I Prediction-Test Assembly* (μ strain)	FEA-II prediction-Connecting Rod Alone** (μ strain)	Theoretical Strain*** (μ strain)	Diff. Measured vs. FEA-I (%)	Diff. Measured vs. FEA-II (%)	Diff. Measured vs. Theoretical (%)
3000 lbs Tensile load	473	467	477	483	1.2	-0.8	-2.1
3000 lbs Compressive load	-486	-480	-480	-483	1.2	1.2	0.6

* FE model included the connecting rod, the pins at the ends, interference fit, axial load and restraints

** FE model included only the connecting rod with the load, applied as uniformly distributed in compression or a cosine distribution in tension, and restraints

*** Theoretical strain calculated from: $\epsilon_{xx} = \frac{F}{AE} * 10^6$

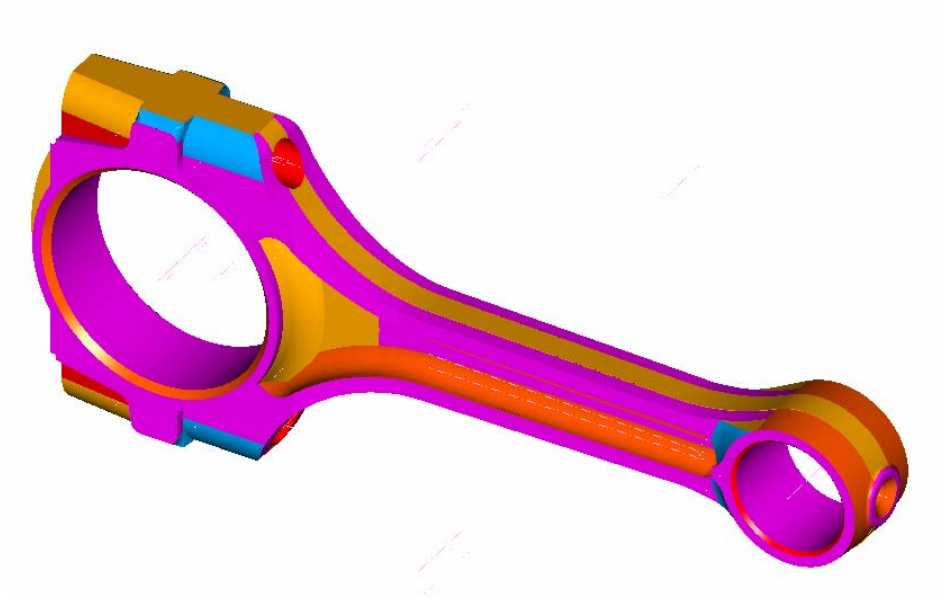
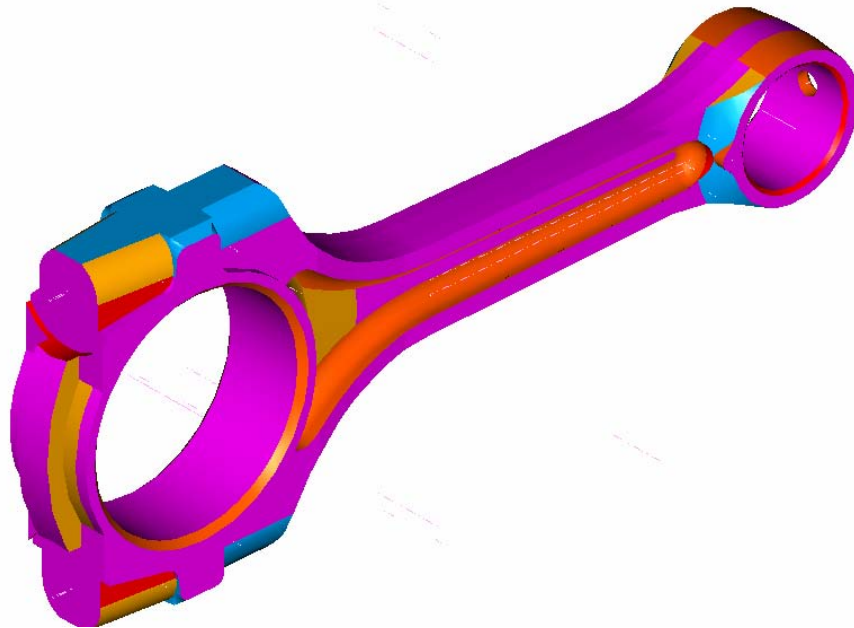


Figure 3.1: Geometry of the connecting rod generated by the digitizing process.



(a)



(b)

Figure 3.2: Solid model of the connecting rod used for FEA. (a) Isometric view. (b) View showing the features at the crank end.

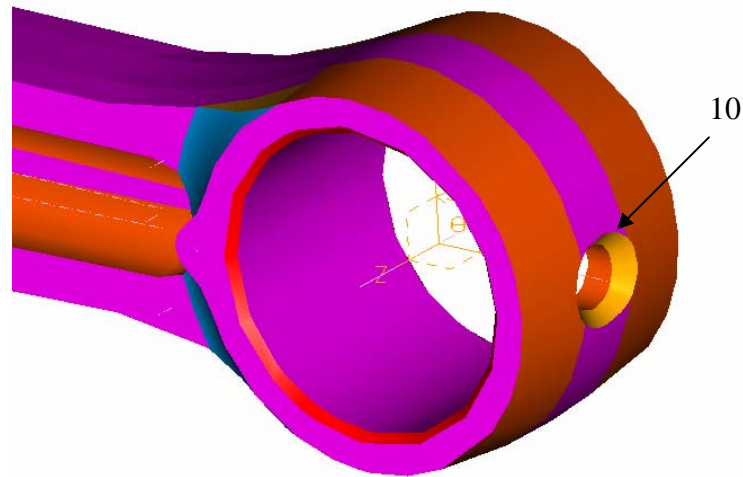
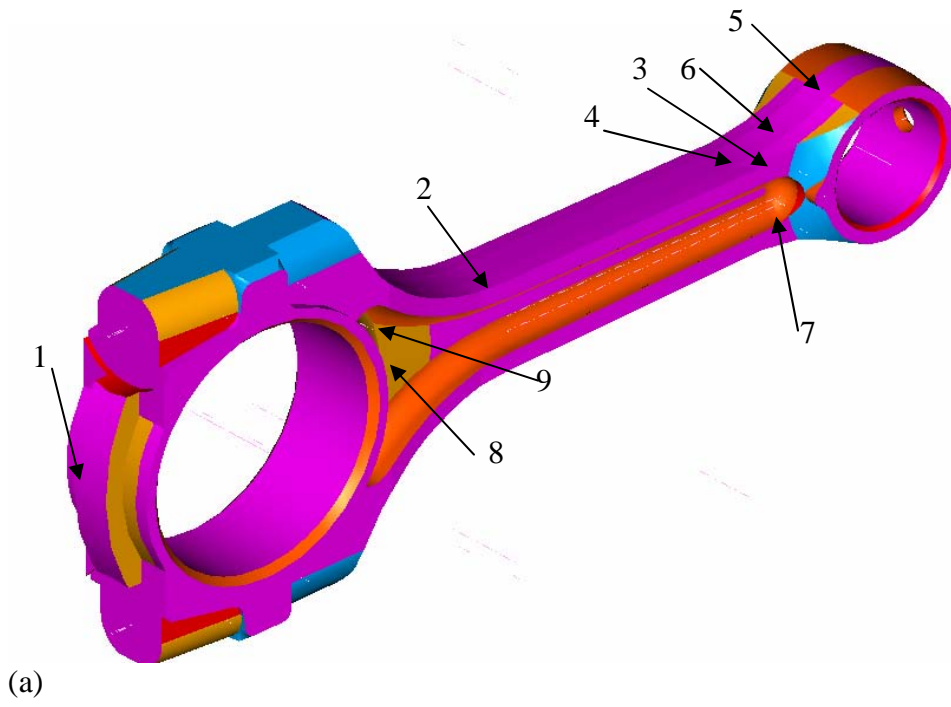


Figure 3.3: Locations on the connecting rod used for checking convergence. (a) Locations on the connecting rod. (b) Location at the oil hole.

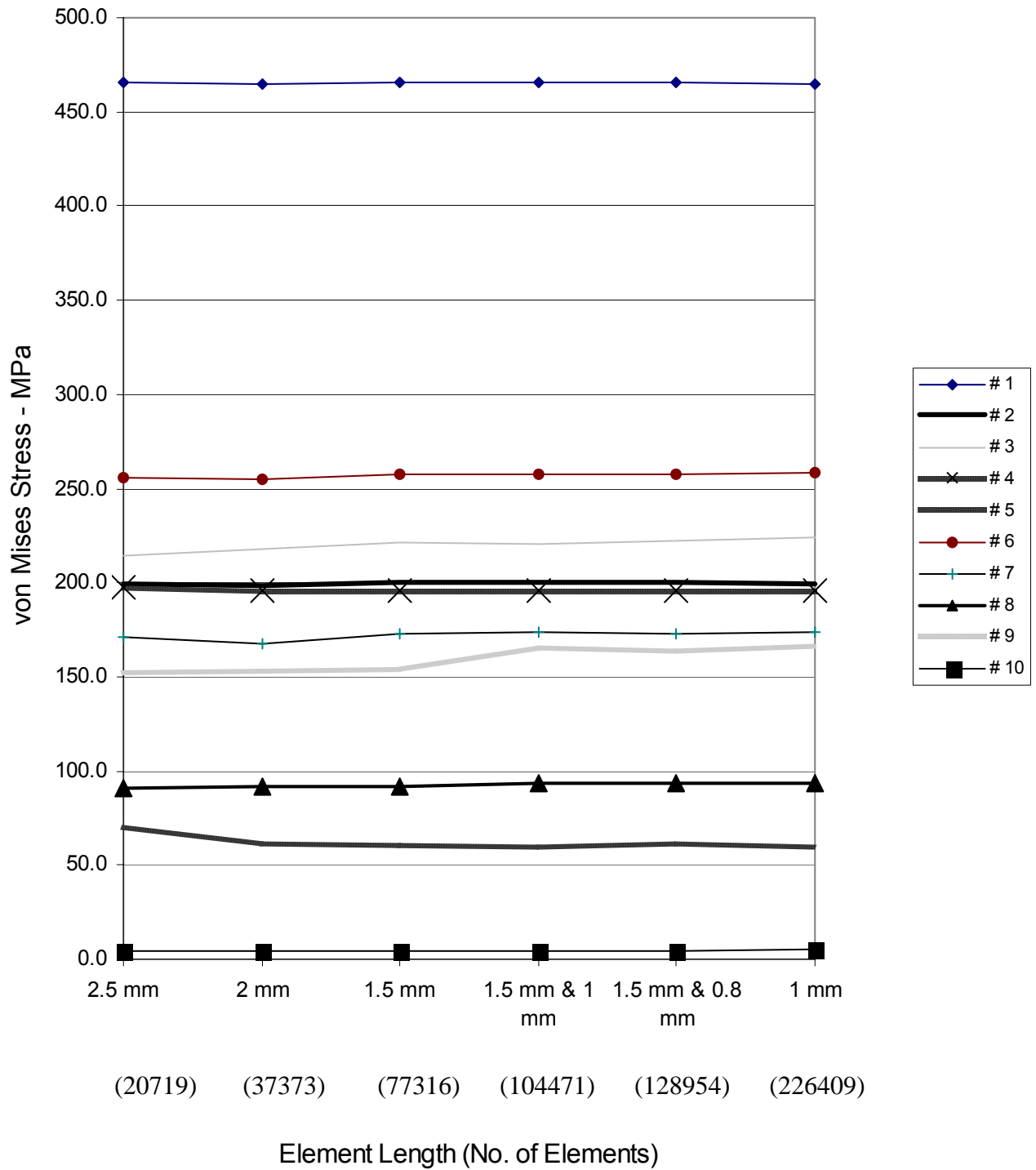
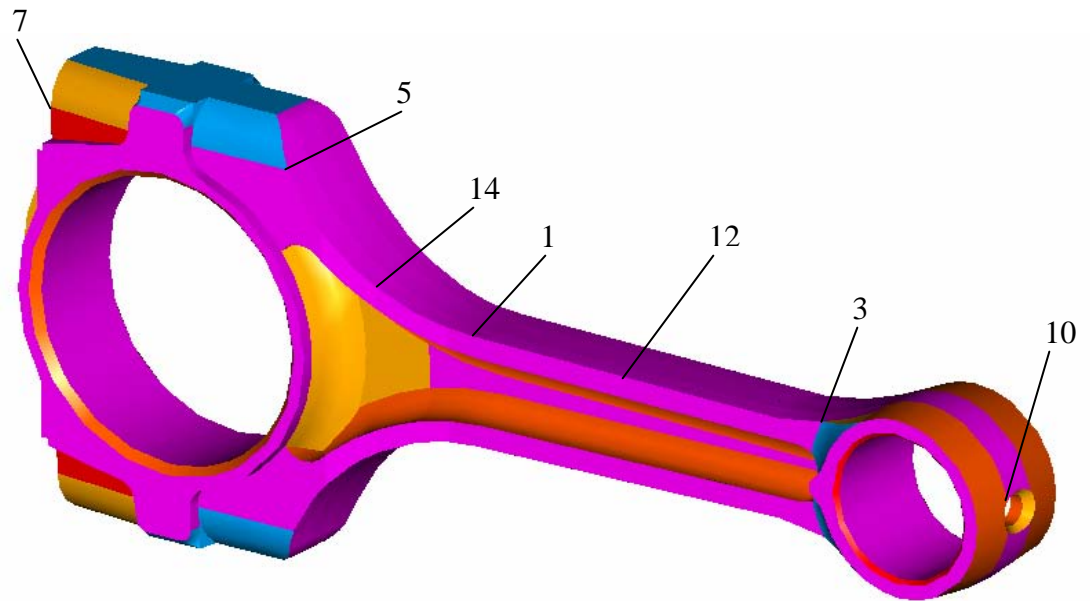
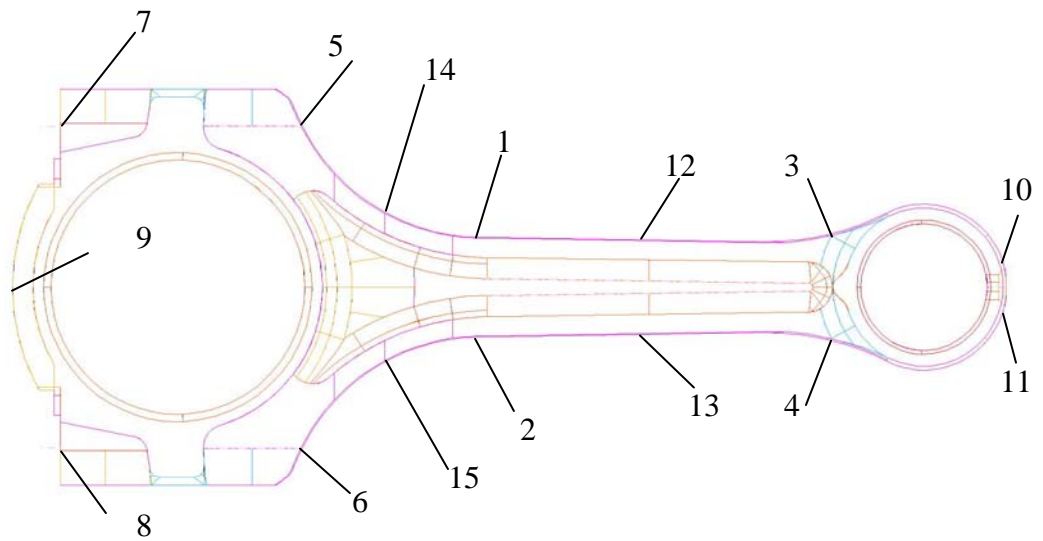


Figure 3.4: von Mises stress at locations 1 through 10 in Figure 3.3. Note that convergence is achieved at most locations with element length of 1.5 mm. Further local refinement with element length of 1 mm produced convergence at location 9.



(a)



(b)

Figure 3.5: Locations on the connecting rod where the stress variation has been traced over one complete cycle of the engine. (a) Locations shown on the 3D connecting rod. (b) Other symmetric locations.

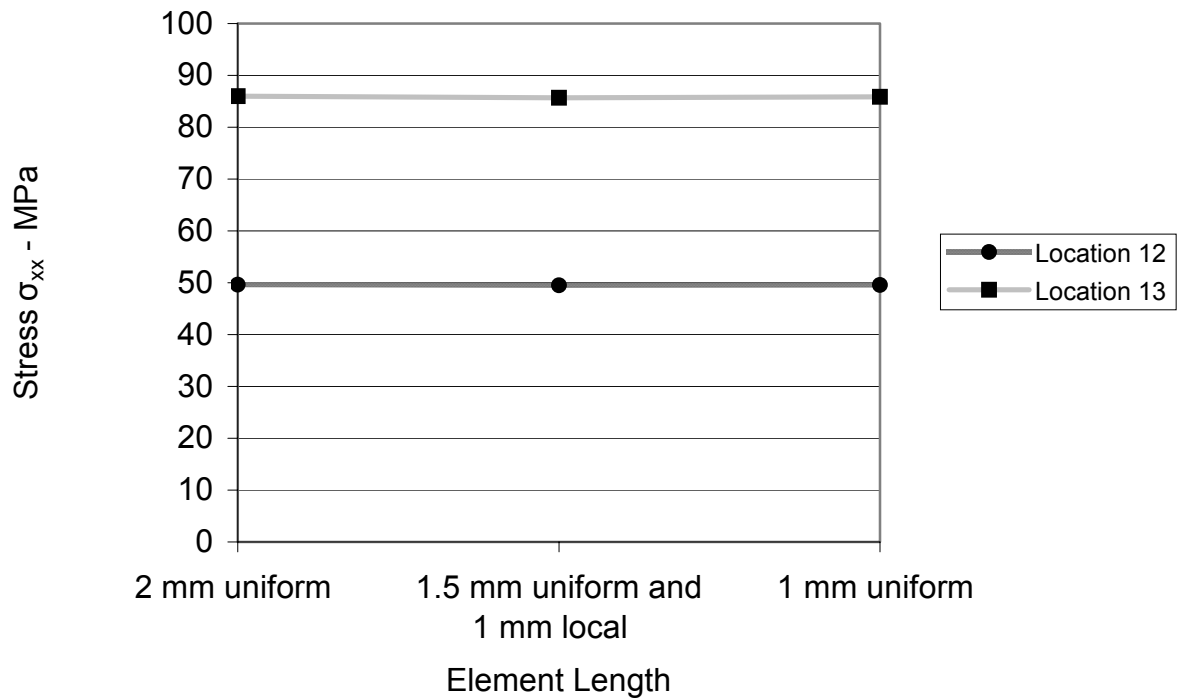


Figure 3.6: Stress along the connecting rod axis in the shank of the connecting rod under dynamic loads as a function of mesh size. Locations 12 and 13 are shown in Figure 3.5.

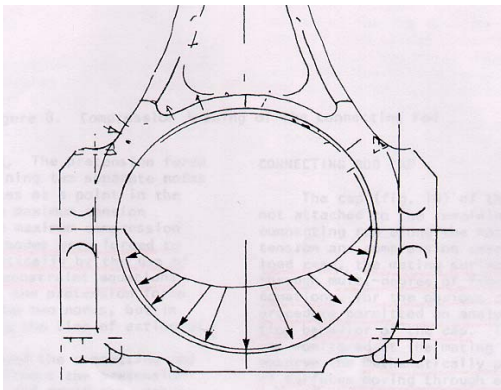


Figure 3.7: Tensile loading of the connecting rod (Webster *et al.* 1983).

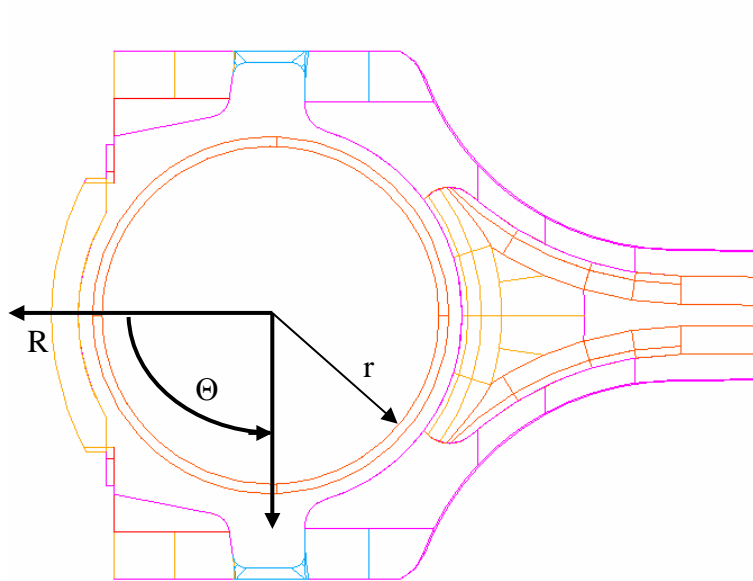


Figure 3.8: Polar co-ordinate system R , Θ , Z used. 't' (not shown) is the thickness of the contact surface normal to the plane of paper.

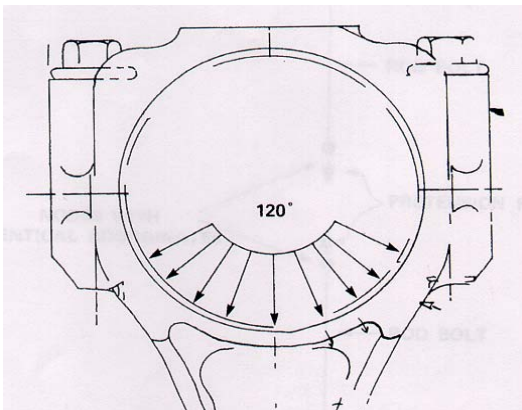


Figure 3.9: Compressive loading of the connecting rod (Webster *et al.* 1983).

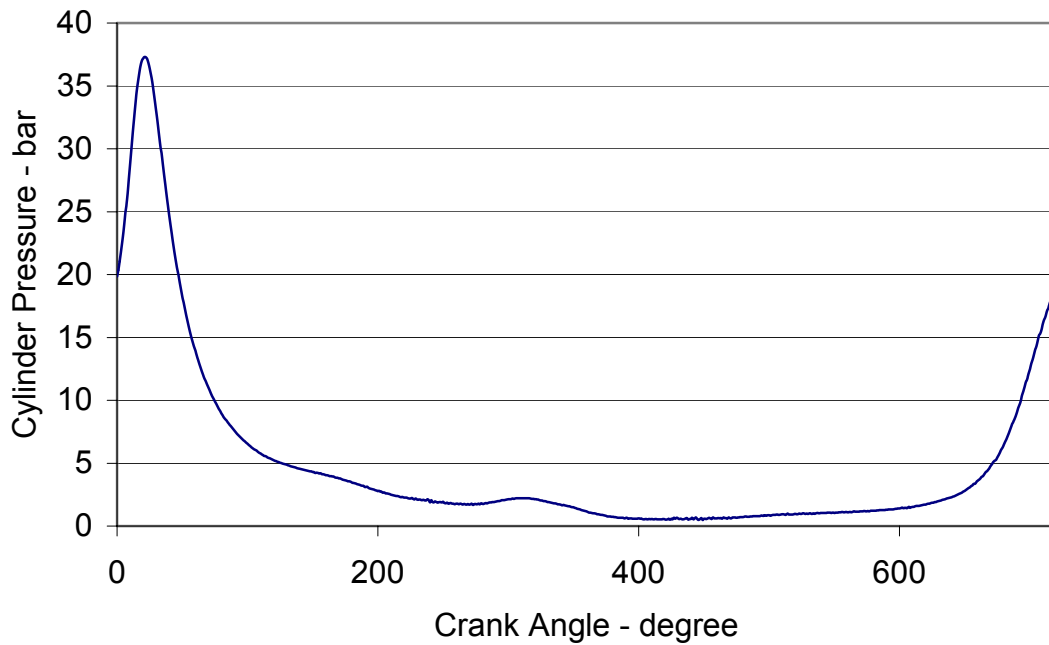


Figure 3.10: Pressure crank angle diagram also known as the indicator diagram (supplied by OEM).

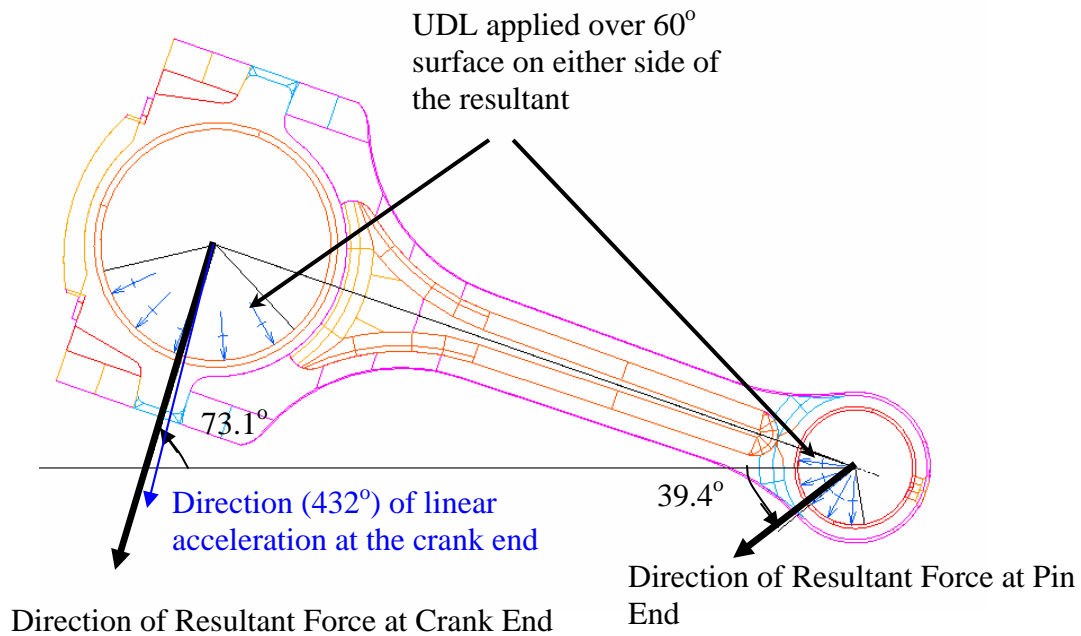


Figure 3.11: Illustration of the way in which boundary conditions were applied when solving the quasi-dynamic FEA model.

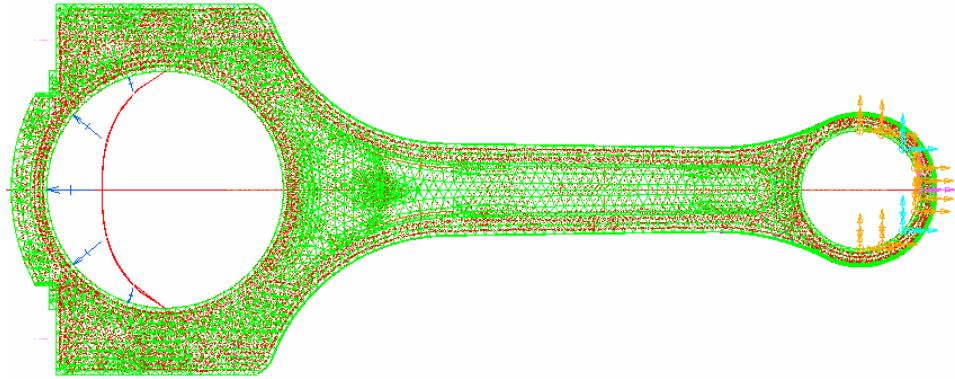


Figure 3.12: FEA model of the connecting rod with axial tensile load at the crank end with cosine distribution over 180° and piston pin end restrained over 180° .

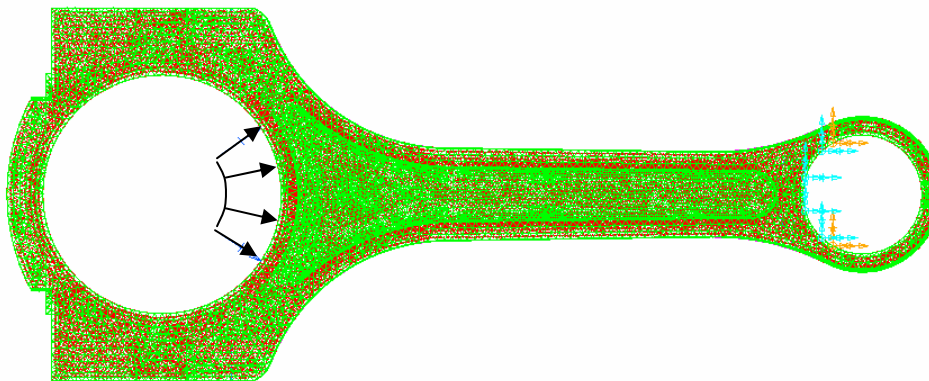


Figure 3.13: FEA model of the connecting rod with axial compressive load at the crank end uniformly distributed over 120° (as shown in Figure 3.9) and piston pin end restrained over 120° .

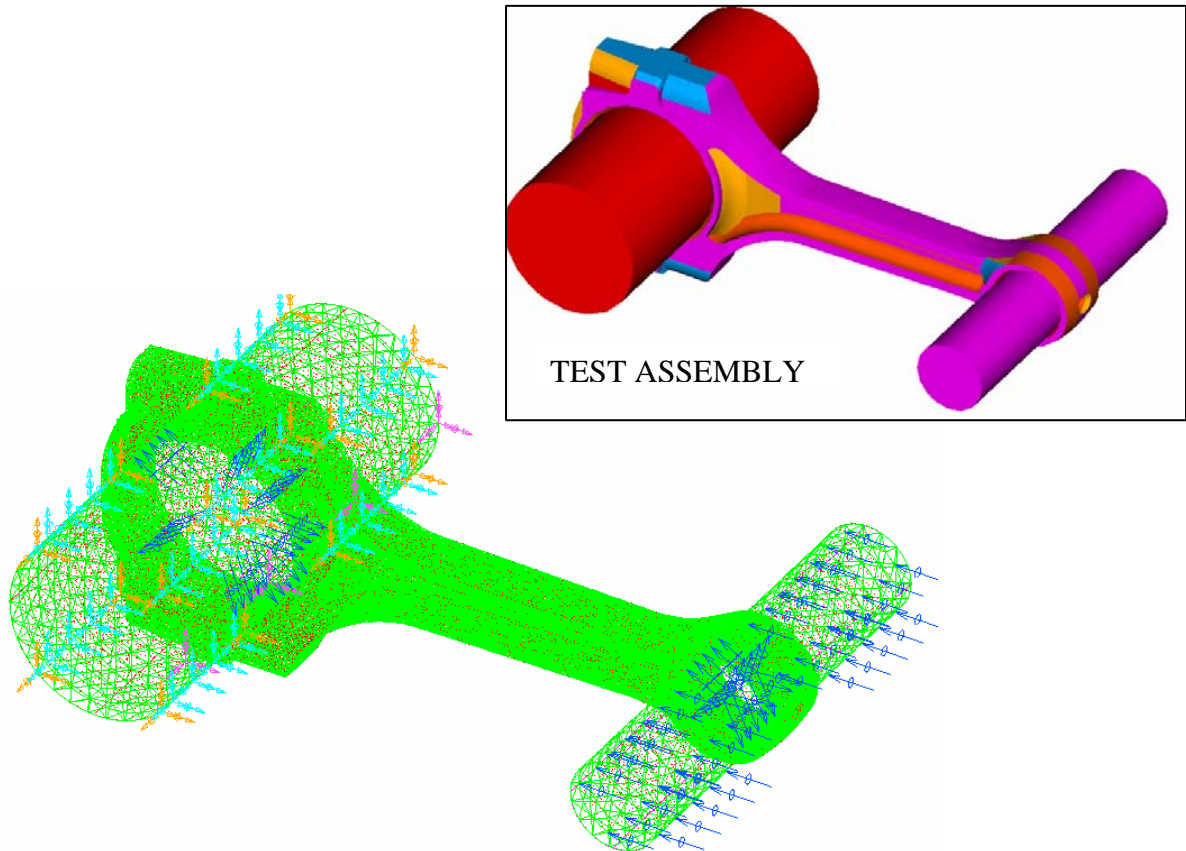


Figure 3.14: Solid model of the test assembly and the finite element model used for the assembly. The FEM includes the axial compressive load applied to the pin at the piston pin end, the restraints applied to the crank pin, the interference simulated by applying pressure, and contact elements between the pins and the connecting rod.

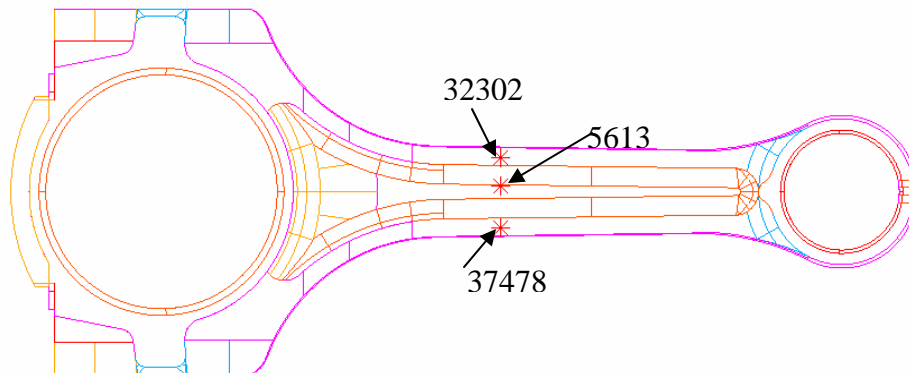


Figure 3.15: Location of nodes used for validation of the FEA model.

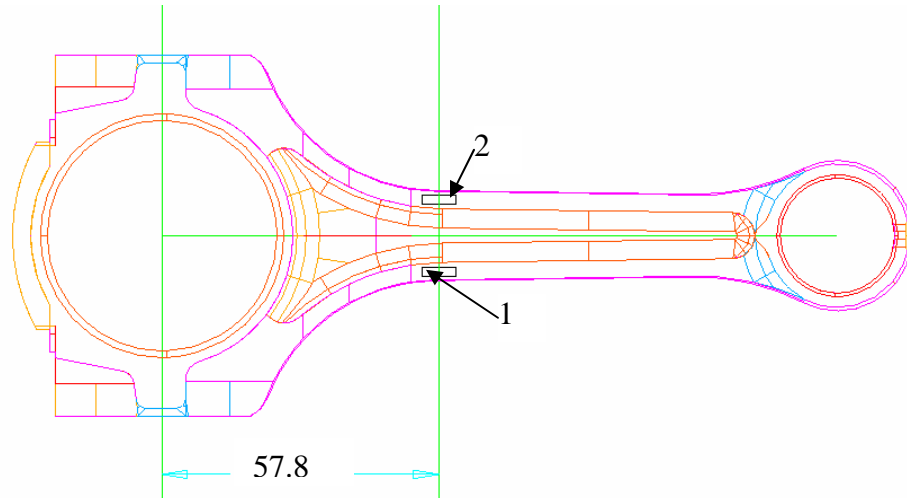


Figure 3.16: Location of two strain gages attached to the connecting rod. Two other gages are on the opposite side in identical positions.

4. RESULTS OF FINITE ELEMENT STRESS ANALYSIS

The load analysis was carried out to obtain the loads acting on the connecting rod at any given time in the loading cycle and to perform FEA. Most investigators have used static axial loads for the design and analysis of connecting rods. However, lately, some investigators have used inertia loads (axial load varying along the length) during the design process. A comparison between the two is needed and is discussed in this chapter.

Connecting rods are predominantly tested under axial fatigue loading, as it was the case for the connecting rod investigated in this project (Afzal, 2004). The maximum and minimum static loads can simulate the fatigue testing range. As a result, FEA was carried out under axial static load with no dynamic/inertia loads. In order to capture the structural behavior of the connecting rod under service operating condition, quasi-dynamic FEA was also performed. Quasi-dynamic FEA results differ from the static FEA results due to time varying inertia load of the connecting rod which is responsible for inducing bending stresses and varying axial load along the length.

The results of the above mentioned analyses are presented and discussed in this chapter with a view to use them for optimization. This chapter discusses the stress-time history at critical locations, selection of load or the loads under which the connecting rod should be optimized, comparison of the quasi-dynamic with static stress analysis results and obtaining the bending stress magnitude and load ratios.

4.1 QUASI-DYNAMIC STRESS ANALYSIS

A few geometric locations were identified on the connecting rod at which the stresses were traced over the entire load cycle to obtain the stress-time history. These locations are shown in Figure 3.5.

Static FEA results showed high stresses in the regions of the transitions to the shank at the crank end and piston pin end, the oil hole, and the cap. From these regions, representative locations were selected at which stresses could be traced. Locations 1, 3, 9, 10 and 14 in Figure 3.5 are such that a node would be created at these locations and could be identified for any orientation of the connecting rod. It must be borne in mind that with auto-mesh used here for meshing, it is difficult to control generation of a node at a specific location within the interior of a surface or a volume. However, a node is created and clearly identified at a vertex. Locations 1, 3, 9, 10 and 14 in Figure 3.5 are such vertices (generated by intersection of surfaces) on the geometry and representative of those regions. Locations 2, 4, 11 and 15 are symmetrically located, from locations 1, 3, 10, 14, respectively with respect to the centerline of the connecting rod. Locations 12 and 13 were selected to capture the behavior of the shank. Locations 5, 6, 7 and 8 cannot be termed critical locations, but nevertheless were selected as representative locations for the crank end region. Location 9 is located on the mid plane. One might argue that the stresses at the mid plane are usually higher than the stresses at the edge of the component and that all the chosen locations should be on the mid plane. However, making such a choice would not have altered the conclusions or observations made in the following paragraphs. Further references have been made to this effect, where appropriate. Figures 4.1 through 4.8 show the stress-time histories for these locations at a crank speed of 5700

rev/min. Also superimposed on these plots is the von Mises stress at these locations under a static load. The static load used for obtaining the stress is either the maximum load at the crank end or the maximum load at the pin end, depending on whether the location in question is closer to the crank end or the pin end. For example, since locations 1 and 2 are closer to the crank end, the static load used was the maximum load at the crank end (17.7 kN). However, since locations 3 and 4 are closer to the pin end, the static load used was the maximum load at the pin end (9.4 kN). In addition to the static von Mises stress, von Mises stress variation under service operating condition is also plotted. The signed von Mises stress is used in this case. The von Mises stress carries the sign of the principal stress that has the maximum absolute value.

One of the objectives of performing the quasi-dynamic FEA was to determine the design loads for optimization. The maximum compressive load that could act on the connecting rod is the load corresponding to the peak gas pressure. Figure 2.10 indicates that the peak gas pressure occurs at about 22° crank angle. The axial component of this load is 21.8 kN, which is the design compressive load for the connecting rod. This is essentially a static load (where the loads at the crank and pin ends are the same). This compressive load acts in the region of the connecting rod between the centers of the crank end and piston pin end. Virtually no load acts on the crank end cap under the compressive load.

The other extreme load that acts on the connecting rod is the tensile load, which increases as the engine speed increases, as evident from Figure 4.9. Figure 4.9 shows a plot of stress variation with engine speed and indicates that tensile stress increases as the speed increases, due to an increase in the tensile load. This can be anticipated due to the

fact that as the engine speed is raised the inertia load due to the piston mass increases, thus increasing the tensile load on the connecting rod. Maximum tensile load on the connecting rod is attained at the maximum engine speed. Therefore, the tensile design load for the connecting rod is a load at the maximum engine speed of 5700 rev/min, as specified by the OEM. It should be noted that the tensile design load consists of both structural load and acceleration load. Also notice from Figure 4.9 that the mean stress increases with increasing engine speed, while the stress amplitude is almost independent of speed.

Figure 2.15, which shows load variation at 5700 rev/min, indicates that the peak tensile load (the resultant of the x and y components) at the crank end occurs at 362° . Figure 2.16, which shows load variation at the pin end, also indicates that the peak tensile load at the pin end occurs at 362° . This suggests that the load corresponding to 362° crank angle should be used as the tensile design load. However, before the load at this crank angle could be used as the design load, it should be verified that this is in fact the worst case loading. Figure 1.5 shows that the peak stress (not load) at the column bottom occurs at close to 382° and far from 360° . The stress-time history at location 2 for this connecting rod (Figure 4.1), indicates a peak at 348° , and far from 360° . Note that locations 1 and 2 are both right at the transition to the crank end, and therefore, a critical region. In light of these facts, it is essential to verify that the load corresponding to 362° crank angle is the worst case loading. Due to symmetry of the load and simplicity of generating the FEA model, FEA was performed at 360° rather than at 362° . The external loads (loads at the ends) at 360° crank angle differ from the loads at 362° crank angle by less than 0.4%.

The stress-time histories, Figures 4.1 through 4.8, for all the locations except 5 and 6 indicate peak tensile stress in the neighborhood of 360° crank angle. At locations 2 and 13 (Figures 4.1 and 4.7) the maximum stress occurs at crank angle of 348° (among the crank angles at which FEA was performed). At locations 3, 4, 7, 8, 9, 10, 11, 14 and 15 the maximum stress does occur at 360° crank angle (among the crank angles at which FEA has been performed). At locations 5 and 6 the stresses are very low. Clearly, not one instant of time can be identified as the time at which all the points on the connecting rod experience the maximum state of stress. However, on the basis of the load analysis and because most of the critical locations undergo maximum tensile stress at crank angles near 360° , the load corresponding to this crank angle has been considered as the tensile design load. The load at 362° is higher than that at 360° by just about 0.2% at the crank end and 0.4% at the pin end. The benefit of using the load corresponding to 360° crank angle is simplicity and symmetry of the FE model. The following paragraph further clarifies the reasons for using the load at 360° crank angle at 5700 rev/min as the tensile design load.

Under tensile load, the critical regions are at the transitions to the crank end and to the pin end, such as regions near locations 14, 15, 3 and 4 in Figure 3.5. Under compressive load the critical region is shifted to right where the transition begins, such as regions near locations 1 and 2. This is evident by comparing Figures 4.1 and 4.8. The peak von Mises stress at location 2 is 94 MPa (at 348° crank angle) and that at location 14 is 162 MPa (at 360° crank angle). So in the crank end region, under tensile load the critical region is near location 14, where the peak stress does in fact occur at crank angle of 360° . Under compressive load, location 2 (maximum stress of about 100 MPa)

becomes more critical, in comparison to location 14 (maximum stress of less than 100 MPa). At the pin end transition (locations 3 and 4), the maximum stress occurs at 360° crank angle anyway.

The design of the shank region near location 12, for this particular connecting rod, where peak stress occurs at 348° crank angle is dependent upon the compressive load and not on the tensile load, since the compressive load is higher in magnitude than the tensile load. With the requirements of buckling strengths, and the minimum web and rib dimensions in place, which will keep the stresses low due to higher cross-sectional area, there is very little likelihood that this region will violate any stress constraints at crank angles near 360° .

It should be noted that none of the abovementioned observations would change if the locations chosen had been on the mid-plane of the connecting rod or a location that experienced higher stress, but in the vicinity of the location evaluated.

In summary, the design load range for optimization consists of the peak compressive gas load (static load) of 21.8 kN, and the tensile load at 360° crank angle at 5700 rev/min (dynamic load).

With regards to the load ratio for the connecting rod, at the crank end the load ratio is -1.23 and at the piston pin end the load ratio is -2.31. The load ratio at the crank end is based on the peak compressive load of 21.8 kN and peak tensile load of 17.7 kN (from Figure 2.15). The load ratio at the piston pin end is based on the peak compressive load of 21.8 kN and peak tensile load of 9.4 kN (from Figure 2.16). The maximum loads are nearly axial, and for this reason the above ratios are based on axial loads. For this

reason, fatigue testing at different load ratios is often conducted in order to test different regions of the connecting rod (such as in Sonsino and Esper, 1994).

For fatigue design some investigators used the overall operating load range of the connecting rod (Sarihan and Song, 1990), while some used the load range at the maximum power output (Pai, 1996). With reference to Figure 4.9, for location 12 the overall operating stress range is 244 MPa (i.e. -160 MPa to 84 MPa). This stress range is obtained using the overall load range. The stress range at the maximum speed for this location is 157 MPa (i.e. -73 MPa to 84 MPa), a 36% decrease (when compared with 244 MPa) in the operating stress range. A 36% change in the stress amplitude can result in more than an order of magnitude change in the fatigue life. Evidently, using the overall operating range will lead to a very conservative design of the component. Yet, the overall operating range of the component has been used for fatigue design (Sarihan and Song, 1990).

An aspect of dynamic loads is the bending stresses they produce and their significance. All of the locations specified in Figure 3.5 are symmetric with respect to the centerline of the component. A difference between the stresses of the symmetric locations in the plots showing stress-time histories indicate presence of bending stress, the magnitude of which is equal to half the difference. Under static axial load the stress at the symmetric locations will be the same. One way to evaluate the significance of the bending stress is to obtain the maximum bending stress that a section will experience and express it as a percentage of the maximum stress experienced at that section. The maximum bending stress is 26% of the maximum stress at the section through location 12 (Figure 4.7), 22% of the maximum stress at the section through location 1 (Figure 4.1),

6% at the section through location 3 (Figure 4.2), and 7% at the section through location 15 (Figure 4.8). This suggests that bending stiffness needs to be adequate to take care of these bending loads. Note that the SAE case study (1997), referred to in Chapter 1, also indicates that bending stiffness is an important design factor. The plot in Figure 4.7 also highlights the significance of the bending stresses. The resultant loads at either ends of the connecting rod are lower at 348°, when compared with the loads at 360° crank angle. Yet, due to the bending stresses, the stress at location 13 in Figure 4.7 is higher at 348° than at 360° crank angle.

A few observations can be drawn about the state of stress from the stress-time histories in Figures 4.1 through 4.8. Locations 1, 2, 12, and 13 have a uniaxial state of stress. Locations 3 and 4 have predominantly uniaxial state of stress. Locations 5, 6, 10, 11, 14 and 15 have a multiaxial, in-phase state of stress (confirmed by using principal stresses). Locations 7, 8 and 9 have Y components of stress as the significant stresses and have a predominantly uniaxial state of stress. Since some regions have multiaxial state of stress, it is essential to determine if the multiaxiality is significant enough to justify using multiaxial fatigue models. Figure 4.8 indicates that at critical locations 14 and 15 the stress σ_{yy} is as high as 30% of the stress σ_{xx} at crank angle of 360°. This is quite significant. This justifies the need to use multiaxial fatigue models. It is to be noted that the multiaxiality results from stress concentration, such as at locations 14 and 15.

The equivalent stress approach based on von Mises criterion is commonly used for multiaxial proportional loading. The equivalent stress amplitude was calculated based on von Mises criterion, as follows:

$$S_{qa} = \sqrt{\frac{(S_{ax} - S_{ay})^2 + (S_{ay} - S_{az})^2 + (S_{az} - S_{ax})^2 + 6(\tau_{axy}^2 + \tau_{ayz}^2 + \tau_{azx}^2)}{2}} \quad (4.1)$$

The equivalent stress amplitude as calculated using Equation 4.1 and as obtained from the signed von Mises stress curves in Figures 4.1 through 4.8 were observed to be equal, as expected.

The equivalent mean stress was calculated as follows:

$$S_{qm} = S_{mx} + S_{my} + S_{mz} \quad (4.2)$$

Sines had observed that mean shear stress had no effect on cyclic bending or cyclic torsion fatigue limits (Socie and Marquis, 2000). As a result using Equation 4.2 (which does not take the mean shear stress into account) to compute the mean stress is justified. Moreover, it captures the beneficial effect of compressive mean stress, which equivalent mean stress calculated based on von Mises criterion does not.

After obtaining the equivalent mean stress and stress amplitude, the equivalent stress amplitude at $R = -1$ (corresponds to S_{Nf}) was obtained by using the commonly used modified Goodman equation:

$$\frac{S_{qa}}{S_{Nf}} + \frac{S_{qm}}{S_u} = 1 \quad (4.3)$$

It was also noticed that the R ratio varies with location on the connecting rod and engine speed. Figure 4.9 indicates that mean stress varies with engine speed, whereas the stress amplitude is nearly constant at location 12. The R ratio for location 12 changes from -18.8 at 2000 rev/min to -0.86 at 5700 rev/min. It also varies with the location on the connecting rod. This is discussed in Section 4.3 while discussing comparison with other FEA models. The mean stress and stress amplitude at the speed of 5700 rev/min are

shown in Figures 4.10 through 4.15 for the locations identified in Figure 3.5. The combination of mean stress and stress amplitude results in higher fatigue damage at locations such as 2, 4, and 13, as compared with symmetric locations 1, 3, and 12, respectively.

4.2 STATIC AXIAL STRESS ANALYSIS

Figures 4.16 through 4.19 show the von Mises stress distribution of the connecting rod under static axial loading. Figure 4.16 shows the von Mises stress distribution with tensile load at the piston pin end, while the crank end is restrained. Figure 4.17 shows the von Mises stress distribution with tensile load at the crank end, while piston pin end is restrained. Figure 4.18 shows the von Mises stress distribution with compressive load at the piston pin end, while crank end is restrained. Figure 4.19 shows the von Mises stress distribution with compressive load at the crank end, while piston pin end is restrained. The load is 26.7 kN in all the cases.

The differences between the four FEA models are now discussed. In order to do so, the connecting rod has been divided into five regions and nodes were identified for comparison, as shown in the inset in Figure 4.16. Stresses at the nodes shown in the Figure 4.16 are compared in Table 4.1. Under tensile load all the five regions must be compared. Large difference exists between the results of region I, and nodes 3, 4, 5 of regions II, IV, and V, between FEM-1 and FEM-2. The stress values from the two FEM's are very close at nodes 6 and 7 in regions II and node 8 in region III. In FEM-1, the crank end was completely (all degrees of freedom) restrained, while in FEM-2 the pin end was completely restrained. The restraints discussed in Section 3.3.2 are representative of a

fixed end rather than a pin joint. Therefore, results for regions I and II from FEM-1 and for regions IV and V from FEM-2 cannot be considered to predict the structural behavior accurately. A similar argument holds for the case of compressive load (i.e. FEM-3 and FEM-4). Notice that at nodes 6, 7, 8, and 9, the differences between the stresses predicted by FEM-3 and FEM-4 are small.

After considering the appropriate regions of the connecting rod, under the tensile loading, the critical regions in the order of decreasing stress intensity are the oil hole, the surface of the pin end bore, the piston pin end transition, the extreme end of the cap and the crank end transition of the connecting rod. Stress distributions at critical regions under tensile loading have been enlarged in Figures 4.16 and 4.17. Also, the web of the connecting rod in the transition region shown by the red circle in Figure 4.17 is a critical region. Under compressive load, the critical regions are the crank end transition and the pin end transition. Also, the web at the crank end shown in Figure 4.17 has a high stress region (Figure 4.19).

Figure 4.20 shows the von Mises stress at a few discrete locations at the midplane along the length of the connecting rod. This plot gives a general idea of the stress variation along the length of the connecting rod. The static loads for which these stresses are plotted, are a tensile load of 17.68 kN (load at the crank end at 360° crank angle and at 5700 rev/min), and a compressive load of 21.8 kN.

The crank end region in Figure 4.20, especially the region near the bolt holes, shows very low stresses. The highest von Mises stress in the region is about 141 MPa. However, it should be noted that the bolt hole and the bolt pre-tension are not included in the finite element model. The bolt pre-tension will induce compressive stresses in this

region, which will be beneficial to fatigue life. If this region is to be optimized, the bolt-hole and the bolt pre-tension should be modeled and considered during the optimization.

Figure 4.20 indicates that the stresses at the small end transition are in the neighborhood of 400 MPa. Table 4.2 tabulates the von Mises stresses in this region and the nodes that have been used are shown in Figure 4.21. Table 4.2 also tabulates the von Mises stresses at the nodes from the web near the crank end of the connecting rod. The stresses at nodes in this web region, baring node 247, are below 150 MPa. The oil hole is a region that experiences very high local stresses in tension. FEA results indicate locations with local stresses in excess of the yield strength (700 MPa). However, it should be noted that the stresses at the oil hole may not be accurate. This is because the oil hole is very close to the boundary condition (loading). Moreover, during fatigue testing of the connecting rod, no failures were observed in the oil hole region (Afzal, 2004).

4.3 COMPARISON OF STATIC AND QUASI-DYNAMIC FEA RESULTS

The maximum load of 17.72 kN at the crank end from the dynamic load analysis (Figure 2.15) occurs at the crank angle of 362° . The load at the crank end at the crank angle of 360° is 17.68 kN, a difference of 0.2%. In Figure 4.5 the von Mises stress at location 9 under a static load of 17.7 kN (the load at 360° crank angle) is superimposed with the stress variation under dynamic loads (service operating condition). Similar plots are provided for locations 5, 6, 7, and 8 (Figures 4.3 and 4.4). Evidently, FEA under static load predicts higher stresses by about 10% at location 9 (compare maximum stress from quasi-dynamic FEA with static stress), which is one of the critical locations. Similar trend is observed for locations 5, 6, 7, and 8 in Figures 4.3 and 4.4.

The maximum tensile load at the pin end from the dynamic load analysis (Figure 2.16) is 9.44 kN at 362° . At 360° the load (from dynamic analysis) is 9.40 kN. They differ by about 0.4%. In Figure 4.6 the von Mises stress at location 10 under a static load of 9.40 kN (the load at 360° crank angle) is superimposed with the stress variation of locations 10 and 11 under dynamic loads (service operating condition). A similar superimposed plot is provided for locations 3 and 4 (Figure 4.2). Though no significant difference is observed between the static and the maximum quasi-dynamic stresses for locations 10 and 11, a difference is observed for locations 3 and 4. As mentioned earlier, however, locations 10 and 11 are very close to the loading region and the stress values may not be accurate.

The purpose of the above comparison was to compare load range comprising static tensile and compressive loads versus a load range comprising dynamic tensile load and static compressive load. Clearly, the latter is more accurate. So, the dynamic loads, which simulate the service operating condition, should be incorporated directly into the design or the optimization process. The cyclic stresses have been discussed in Section 4.4.

As already mentioned in Chapter 3, FE model of the test set up was built up (i.e. test assembly FEA) and used to verify the strain gage measurements. The axial loads in the FE model were 44.5 kN tensile load and 55.6 kN compressive load. These are the loads under which the connecting rod was fatigue tested in the laboratory under $R = -1.25$ load ratio. Due to the contact problem involved in this FEM, the exact loads were used, though the analysis was linear elastic. The results from this analysis are presented here for comparison with other FEA models. Four cases can be identified here for comparison.

All the four cases have been diagrammatically represented in Figure 4.22. The first, Case-1, is the test condition (load ratio $R = -1.25$) in which the pins at both the ends of the connecting rod were modeled and connected by contact elements to the connecting rod. The interference was also modeled and loads and restraints were applied to the pins (the FE model is also referred to as ‘test assembly FEA’). Second, Case-2, component FEA with static tensile and compressive loads (load ratio $R = -1.25$) applied as mentioned in Section 3.3.1- Static FEA. The third case, Case-3, is the FEA under service condition considering the overall operating load range of the connecting rod (quasi-dynamic FEA model used). The fourth case, Case-4, is the FEA under service operating condition, considering the load range at a constant maximum engine speed of 5700 rev/min (quasi-dynamic FEA model used). Figure 4.23 compares the R ratios for locations 1, 2, 3, 4, 9, 12, 13, 14, and 15 (locations shown in Figure 3.5) for the four cases mentioned above. This figure brings out the differences in R ratio under the different cases.

The stresses at locations 5, 6, 7 and 8 are low and, therefore, are not included in Figure 4.23. The stresses at the oil hole and its vicinity exceeded the yield strength by a significant margin with the linear elastic FEA at the tensile load of 44.5 kN. However, no failure was observed in this region during component testing carried out. Evidently the stresses in this region are not accurate, due to the analysis being linear and the region being very close to the boundary condition. Therefore, stresses at locations 10 and 11 are not discussed. However, the other locations considered are at a considerable distance from the oil hole and stresses are lower than the yield strength of the material. One of the most prominent observations from the above figure is that the R ratio at these locations under Case-1 is higher than the R ratio under the overall operating range, Case-3, and less

than the operating range at the maximum speed, Case-4 (except for locations 9 and 4). Connecting rods are also tested in the engine with the load sequence typically consisting of different engine speeds (Sonsino and Esper, 1994). Notice the difference in R ratio at location 9 between Case-1 and Case-2.

Figure 4.24 compares the equivalent stress amplitude at $R = -1$ at the fifteen different locations under three different cases. The connecting rod was tested under $R = -1.25$ load ratio (Afzal, 2004). In order to compare the maximum stress and the stress amplitude under load ratio of $R = -1.25$ at loads that are within the operating range of the connecting rod, the results of Case-2 were scaled for the load of 17.4 kN (the tensile load at $R = -1.25$) and compressive load of 21.8 kN

Case-3 and Case-4 are as described in the previous paragraph. Notice that the equivalent stress amplitude at $R = -1$ for Case-2 is higher for all the critical locations. Also the equivalent stress amplitude at $R = -1$ considering the overall load range is higher than that at 5700 rev/min constant engine speed. This suggests that axial fatigue testing is more damaging than engine testing (for all locations, except 5, 6, 7, and 8 which are not critical locations and the stresses are very low at these locations).

Using the results of FEA in Case-2, Figure 4.25 compares the von Mises stress under static tensile load of 17.4 kN and maximum positive von Mises stress under engine operating condition at 5700 rev/min. Figure 4.25 reveals the extent to which the component will have a higher stress under tensile load (responsible for fatigue damage) under axial fatigue loading when compared to the service operating condition.

4.4 OPTIMIZATION POTENTIAL

Figure 4.26 shows the factor of safety (FS), the ratio of yield strength to maximum von Mises stress under service operating condition at the fifteen locations shown in Figure 3.5, over the entire operating load range of the connecting rod. The von Mises stress used is not the signed von Mises stress. The factor of safety used by the OEM for the considered connecting rod design is not known, though the FS used for this connecting rod can be determined.

Figure 4.27 shows the factor of safety, and the ratio of the endurance limit to the equivalent stress amplitude at $R = -1$. The FS is 4 or higher in Figure 4.26, and 2.7 or higher in Figure 4.27 at locations 1, 2, 12, 13, 14 and 15. This clearly shows the large margins that exist for material removal at these locations. Depending upon the FS used for optimization, scope for material removal may or may not exist in regions near locations 3, 4, 9, 10 and 11.

While performing axial fatigue testing of the connecting rods (Afzal, 2004), the applied load range was much higher than the operational load range. Yet, most connecting rods failed near the crank end transition. This is an evidence of the extent to which the connecting rod pin end has been over-designed. Since forces at the pin end are lower in comparison to the forces at the crank end, the strength of the pin end region should ideally be lower, in comparison to the strength at the crank end region for optimum material utilization.

The choice of different locations will definitely show a different picture in terms of available scope for weight reduction. Stresses at these locations still give a general

idea of the scope and direction for optimization. While performing optimization, the stresses at all the nodes are taken into account rather than stresses at just a few locations.

A linear buckling analysis was performed on the connecting rod. The buckling load factor for the connecting rod considered is 7.8, which is high. This factor also indicates that weight reduction is possible. The overall axial displacement of the connecting rod was measured to be 0.206 mm under the tensile load at 360° crank angle at 5700 rev/min. This can be seen as a measure of axial stiffness of the connecting rod. Another important factor for this component is bending stiffness. During optimization of the connecting rod, this factor has been tackled by attempting to maintain as high a section modulus as possible.

In summary, the connecting rod design loads are peak gas load as the maximum compressive load, and dynamic load corresponding to 360° crank angle at 5700 rev/min engine speed as the maximum tensile load. The connecting rod does have a potential for weight reduction. Due to high multiaxiality in a few regions of the connecting rod, equivalent multiaxial stress approach will be used for fatigue design during optimization. The load range for fatigue design will be the entire operating range as per the industry trend (Sarihan and Song, 1990). The entire operating range covers the maximum compressive gas load as one extreme load and the load corresponding to 360° crank angle at 5700 rev/min engine speed as the other extreme load.

Table 4.1: Comparison of static axial stresses under the four FEA model boundary conditions.

	Region	I		II					III		IV			V	
	Node Label	1	2	3	4	5	6	7	8	9	10	11	12	13	14
Tensile load at pin end (FEM-1)	Stress (MPa)	3.3	46.2	16.8	54.1	221.5	238.9	202.7	192.8	185.3	595.9	147.4	460.3	813.9	952.6
Tensile load at crank end (FEM-2)	Stress (MPa)	465.6	211.7	30.0	108.2	319.9	241.4	200.1	196.6	196.0	355.8	55.4	186.0	4.6	443.0
Compressive load at pin end (FEM-3)	Stress (MPa)	7.3	10.5	2.2	26.2	122.1	249.1	215.4	196.5	202.9	306.7	98.0	57.8	54.0	66.7
Compressive load at crank end (FEM-4)	Stress (MPa)	32.2	26.1	10.3	11.8	175.2	251.4	212.3	196.5	204.7	147.2	11.0	7.7	3.3	8.0

Nodes and regions are shown in Figure 4.16

Table 4.2: von Mises stresses at nodes shown in Figure 4.21.

	Tensile Load = 15.9 kN	Compressive Load = 21.8 kN
Node label	von Mises stress (MPa)	von Mises stress (MPa)
Nodes at the web near the crank end		
4933	56	136
7362	98	147
247	98	223
44094	64	116
44102	75	121
Nodes near the pin end transition		
212	357	255
216	46	146
272	46	146
266	359	256

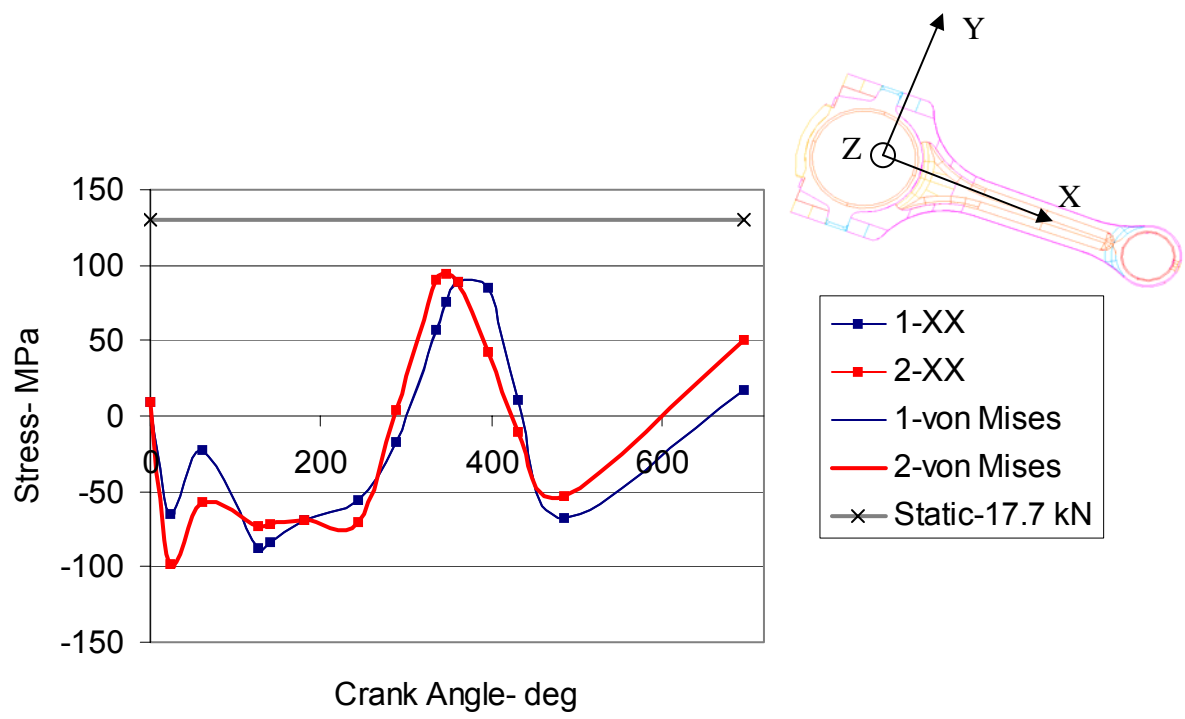


Figure 4.1: Stress variation over the engine cycle at 5700 rev/min at locations 1 and 2. XX is the σ_{xx} component of stress. The stress shown for the static tensile load of 17.7 kN, is the von Mises stress.

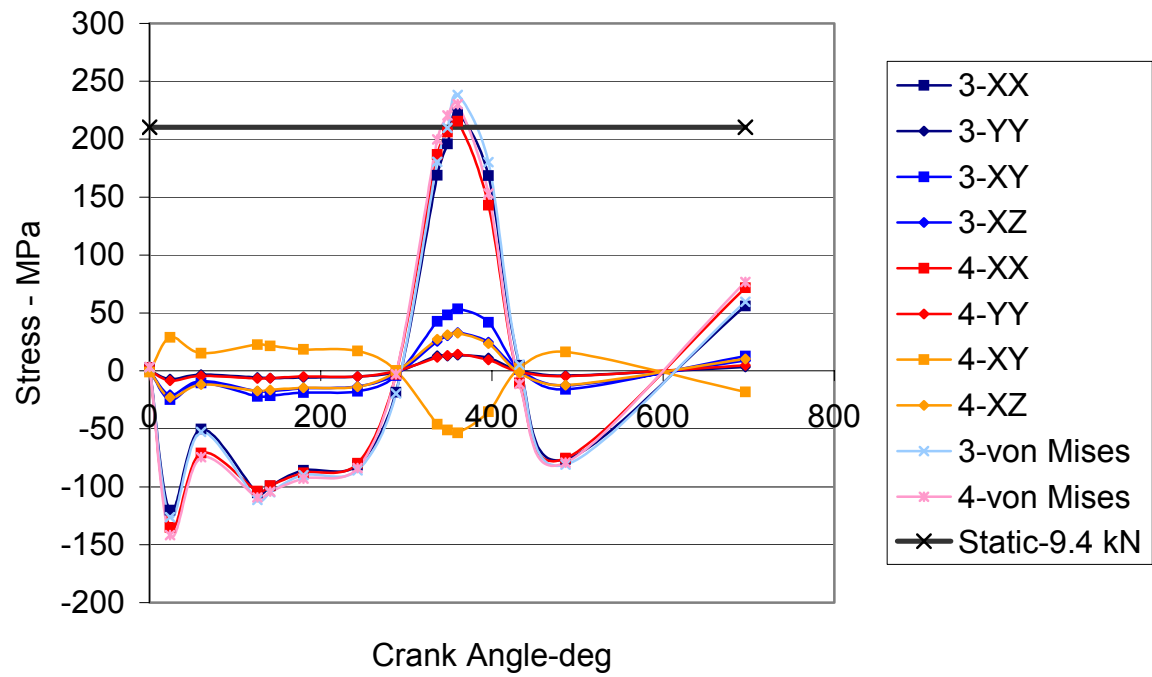


Figure 4.2: Stress variation over the engine cycle at 5700 rev/min at locations 3 and 4. XX is the σ_{xx} component of stress, YY is the σ_{yy} component of stress and so on. The stress shown for the static tensile load of 9.4 kN is the von Mises stress.

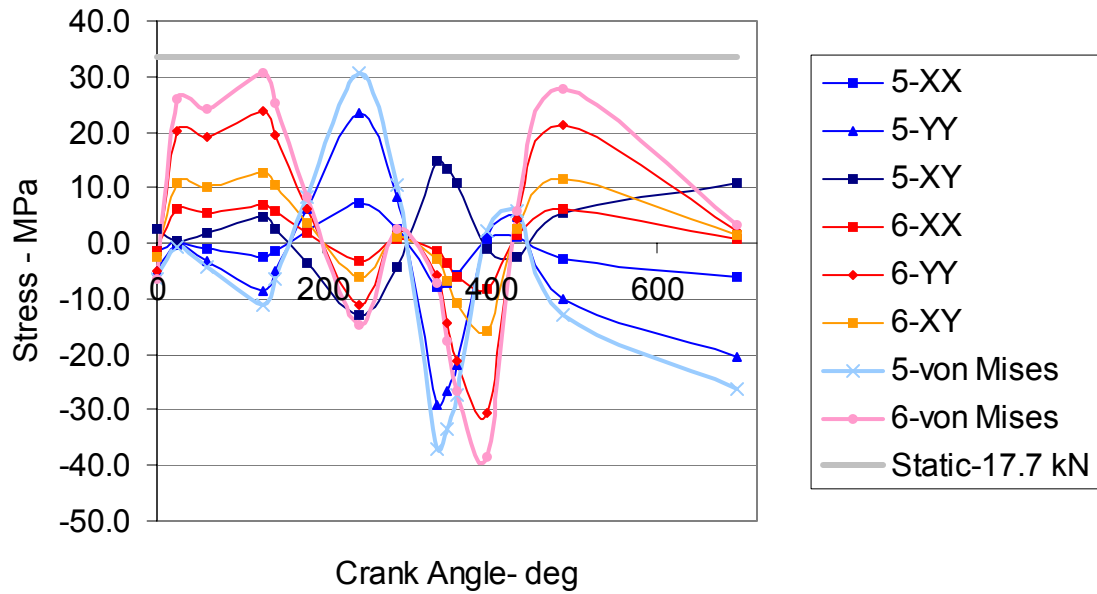


Figure 4.3: Stress variation over the engine cycle at 5700 rev/min at locations 5 and 6. XX is the σ_{xx} component of stress, YY is the σ_{yy} component and so on. The stress shown for the static tensile load of 17.7 kN is the von Mises stress.

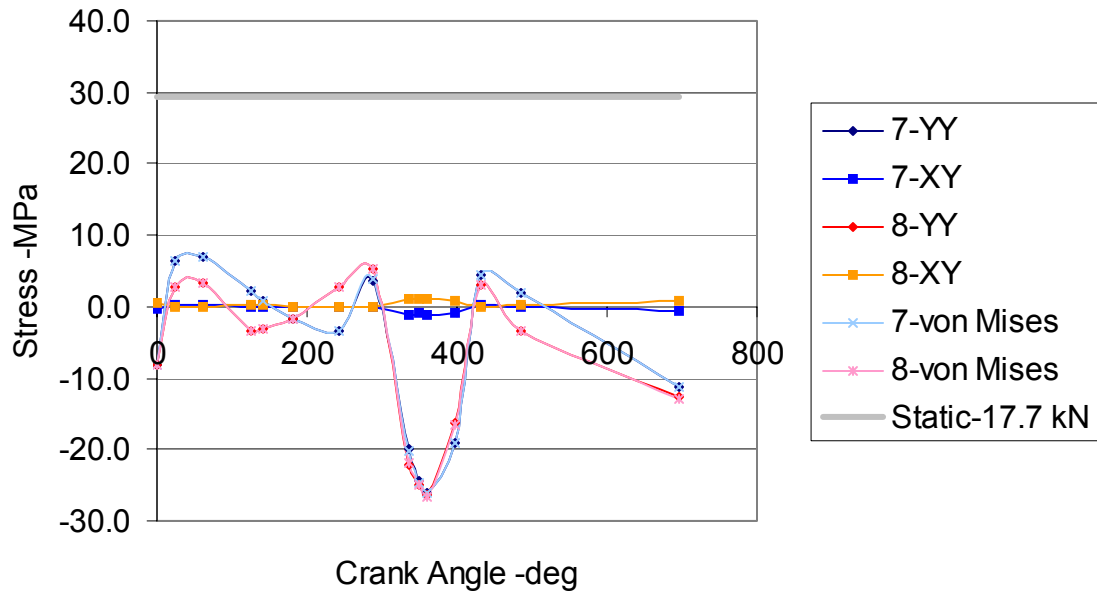


Figure 4.4: Stress variation over the engine cycle at 5700 rev/min at locations 7 and 8. YY is the σ_{yy} component, XY is the σ_{xy} component of stress, and so on. The stress shown for the static tensile load of 17.7 kN is the von Mises stress.

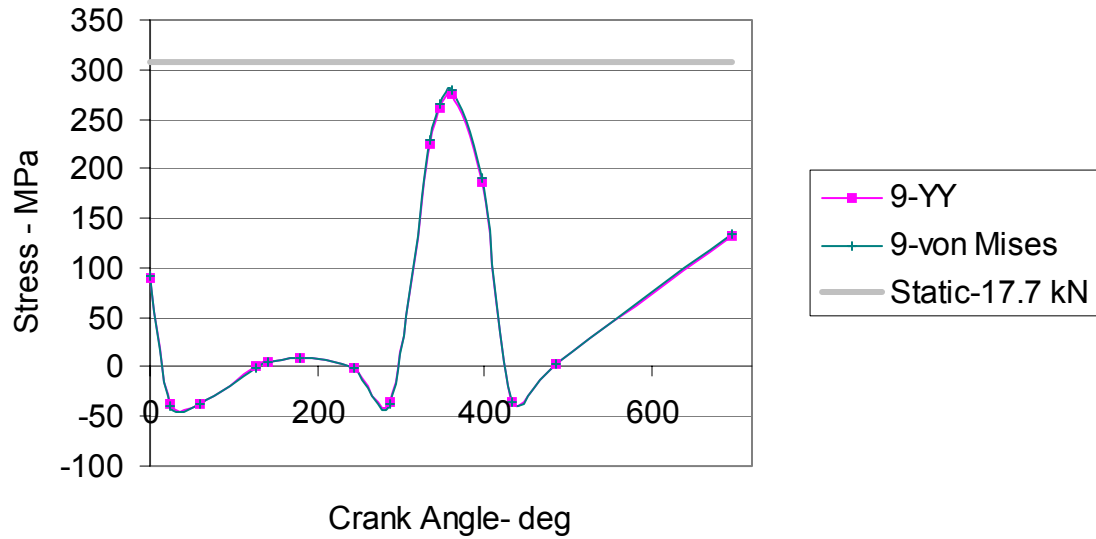


Figure 4.5: Stress variation over the engine cycle at 5700 rev/min at location 9. YY is the σ_{yy} component. The stress shown for the static tensile load of 17.7 kN is the von Mises stress.

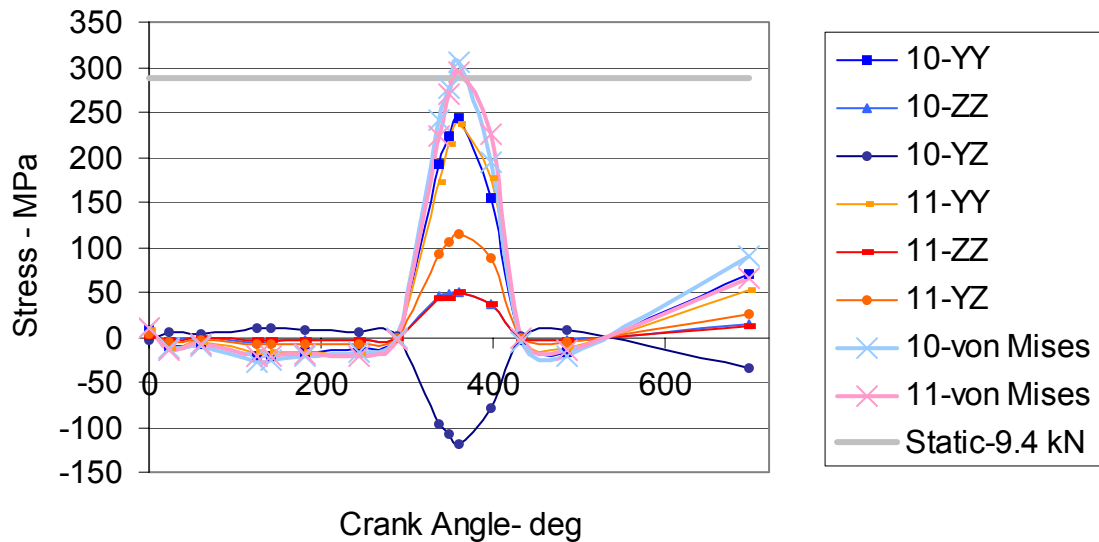


Figure 4.6: Stress variation over the engine cycle at 5700 rev/min at locations 10 and 11. YY is the σ_{yy} component, ZZ is the σ_{zz} component of stress and so on. The stress shown for the static tensile load of 9.4 kN is the von Mises stress.

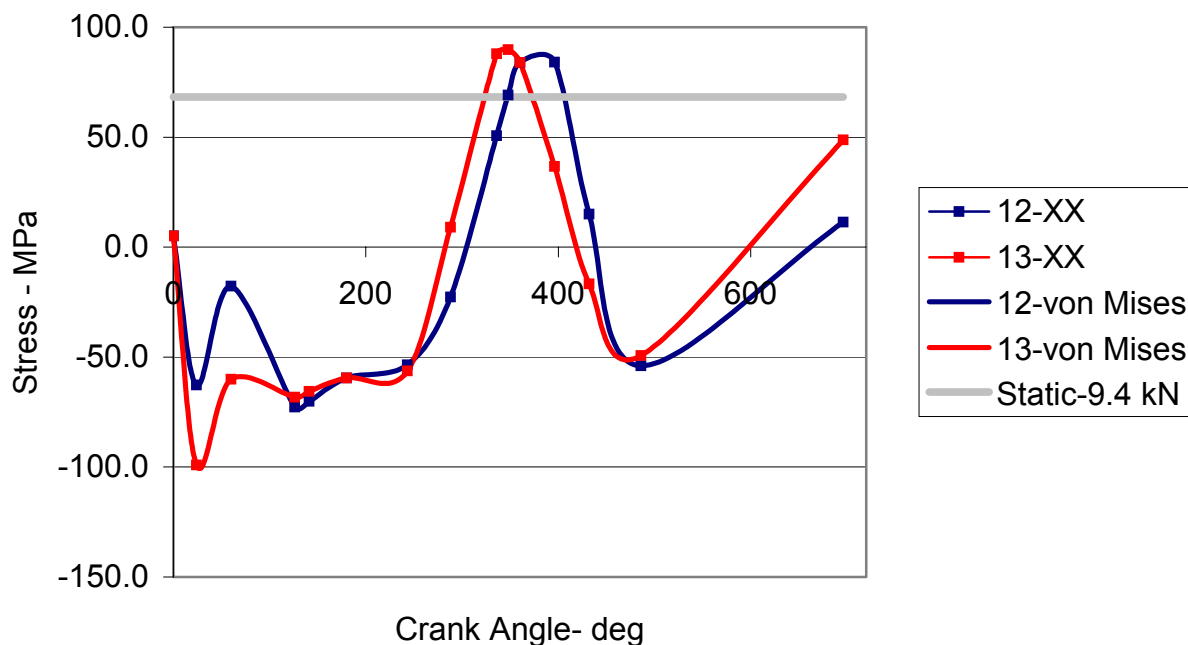


Figure 4.7: Stress variation over the engine cycle at 5700 rev/min at locations 12 and 13. XX is the σ_{xx} component of stress. The stress shown under static tensile load of 9.4 kN is the von Mises stress component.

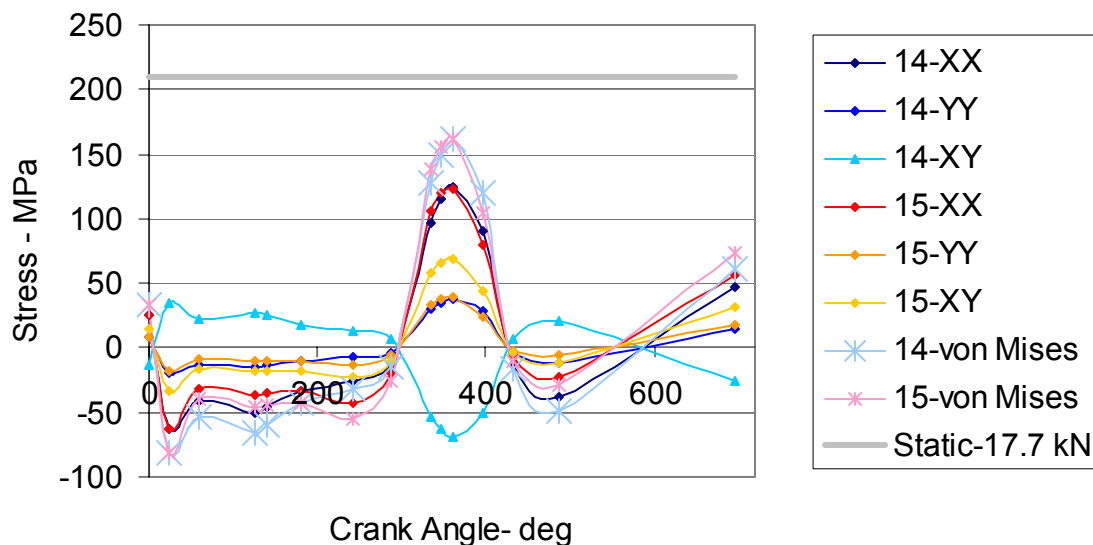


Figure 4.8: Stress variation over the engine cycle at 5700 rev/min at locations 14 and 15. XX is the σ_{xx} component of stress, YY is the σ_{yy} component and so on. The stress shown under the static tensile load of 17.7 kN is the von Mises stress.

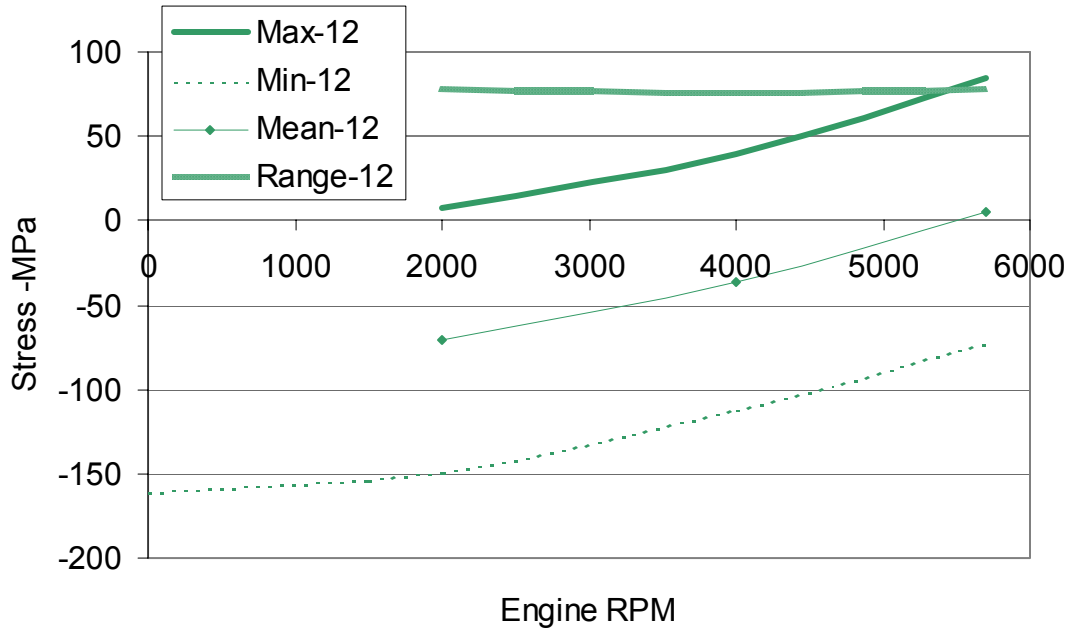


Figure 4.9: Mean stress, stress amplitude, minimum stress and maximum stress at location 12 (w.r.t. Figure 3.5) on the connecting rod as a function of engine speed.

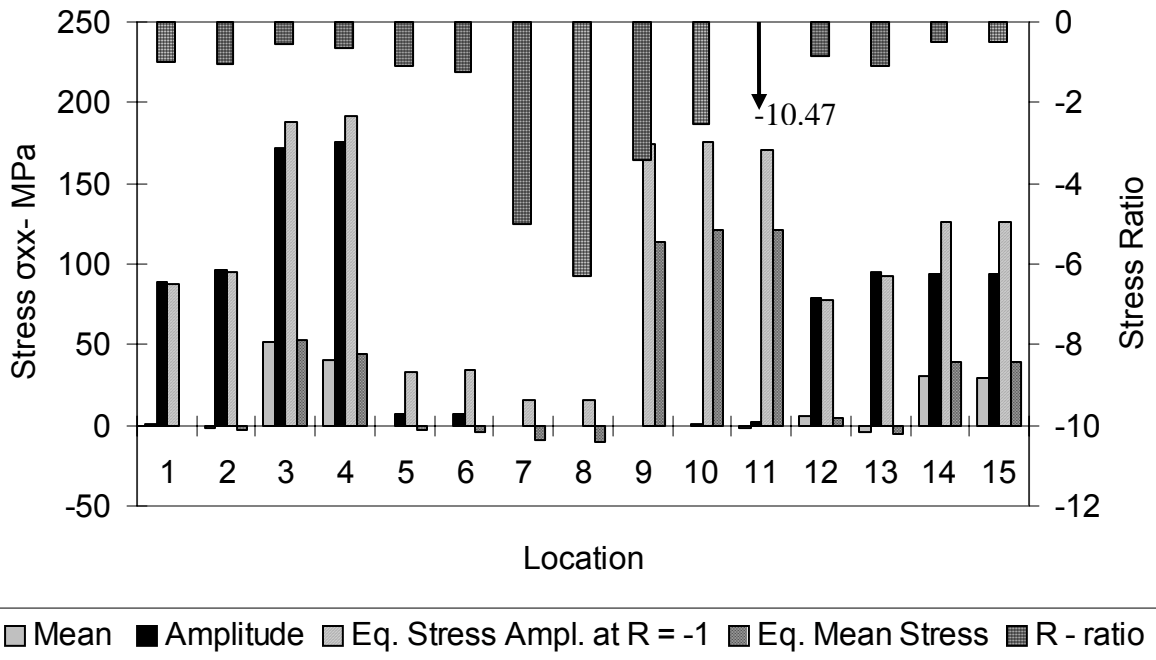


Figure 4.10: Mean stress, stress amplitude, and R ratio of the σ_{xx} component, and the equivalent mean stress and equivalent stress amplitude at R = -1 at engine speed of 5700 rev/min at locations 1 through 15.

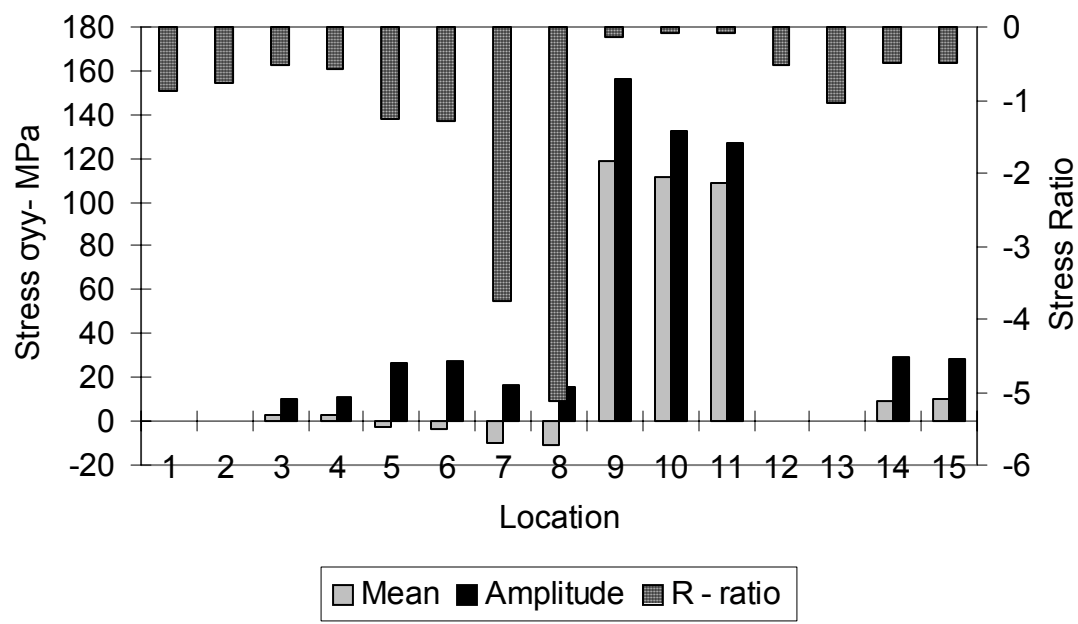


Figure 4.11: Mean stress, stress amplitude and the R ratio of the σ_{yy} component at engine speed of 5700 rev/min at locations 1 through 15.

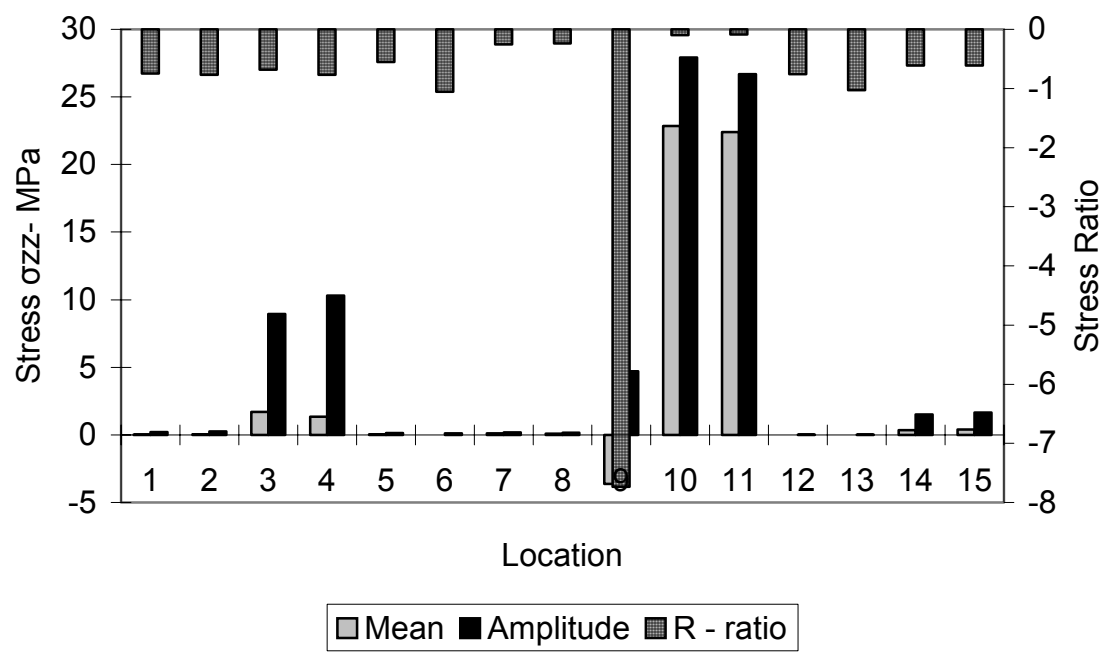


Figure 4.12: Mean stress, stress amplitude, and the R ratio of the σ_{zz} component at engine speed of 5700 rev/min at locations 1 through 15.

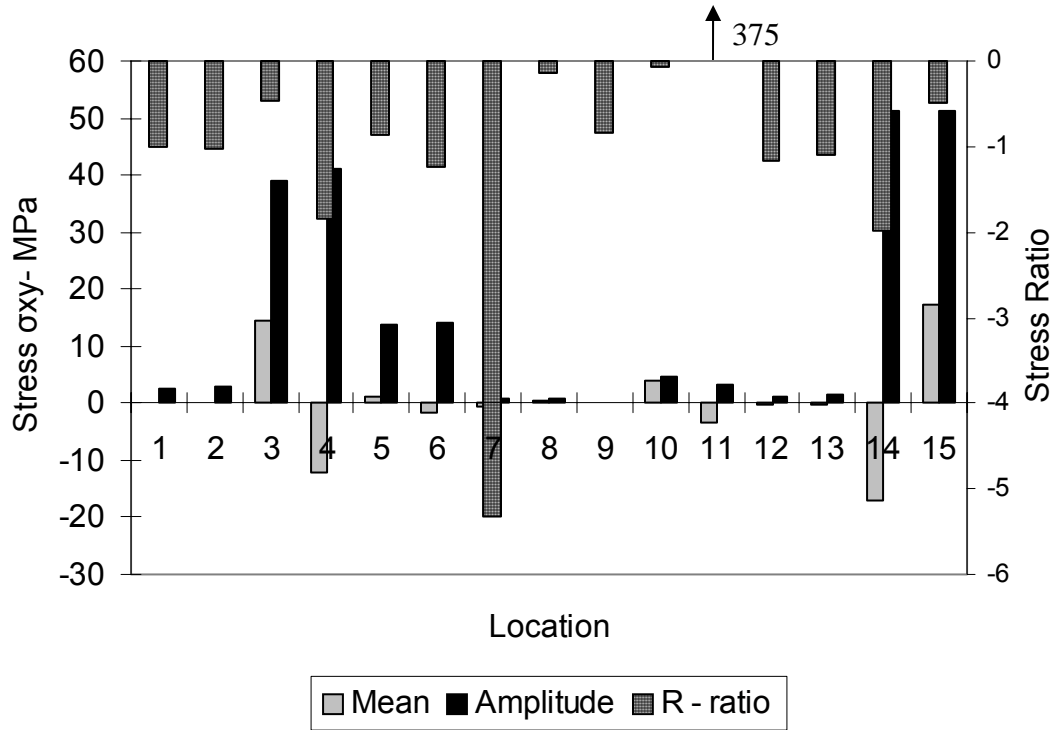


Figure 4.13: Mean stress, stress amplitude, and the R ratio of the σ_{xy} component at engine speed of 5700 rev/min at locations 1 through 15.

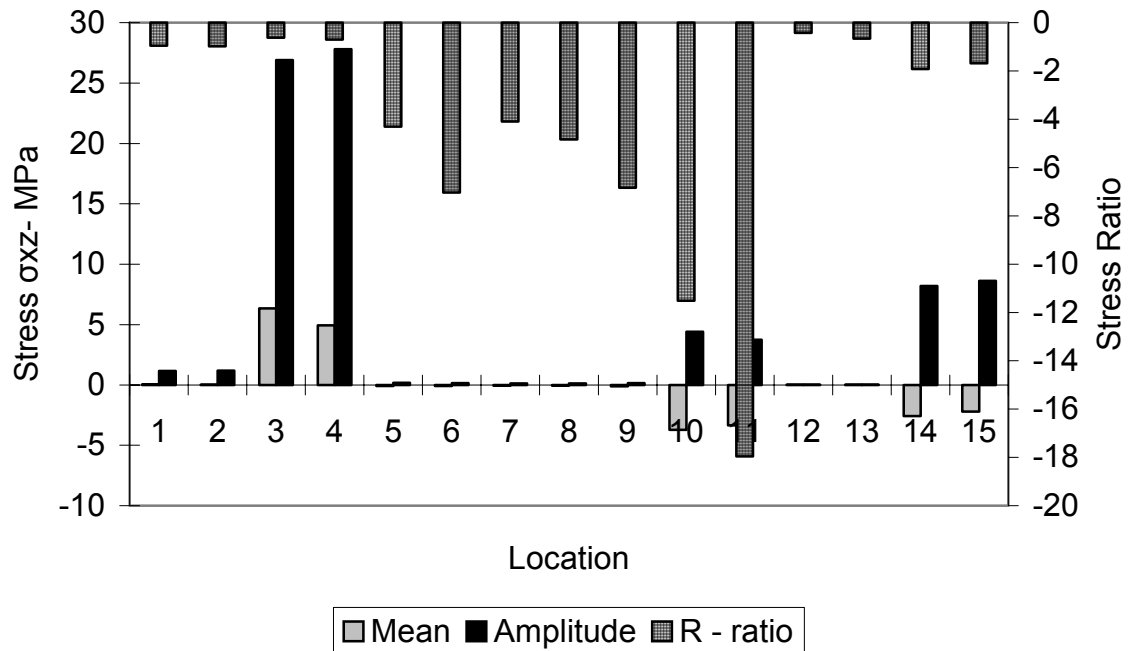


Figure 4.14: Mean stress, stress amplitude, and the R ratio of the σ_{xz} component at engine speed of 5700 rev/min at locations 1 through 15.

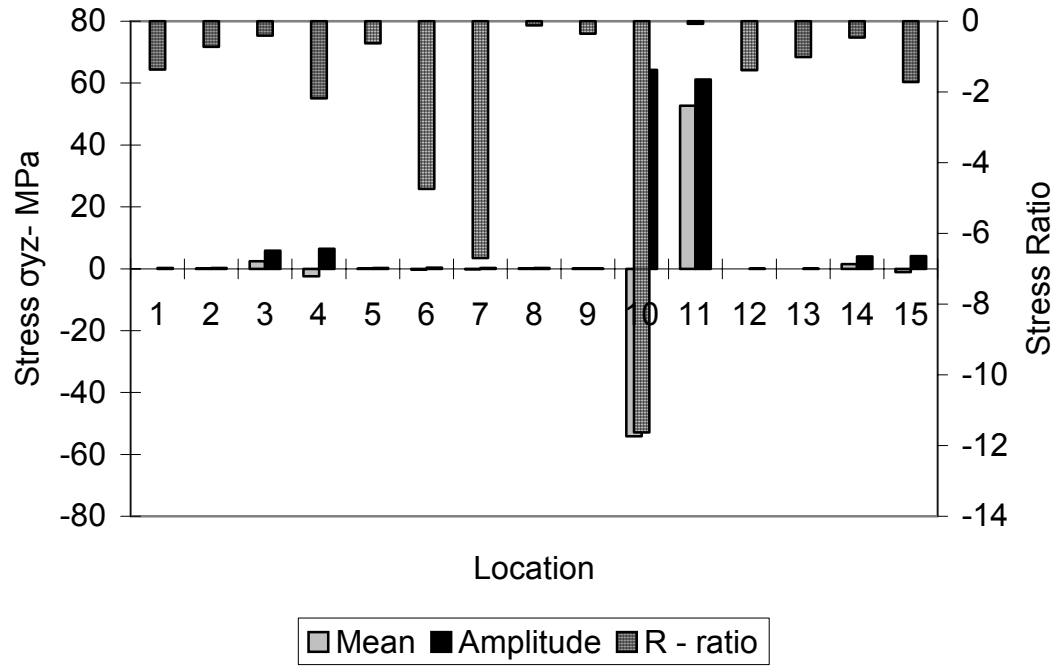


Figure 4.15: Mean stress, stress amplitude, and the R ratio of the σ_{yz} component at engine speed of 5700 rev/min at locations 1 through 15.

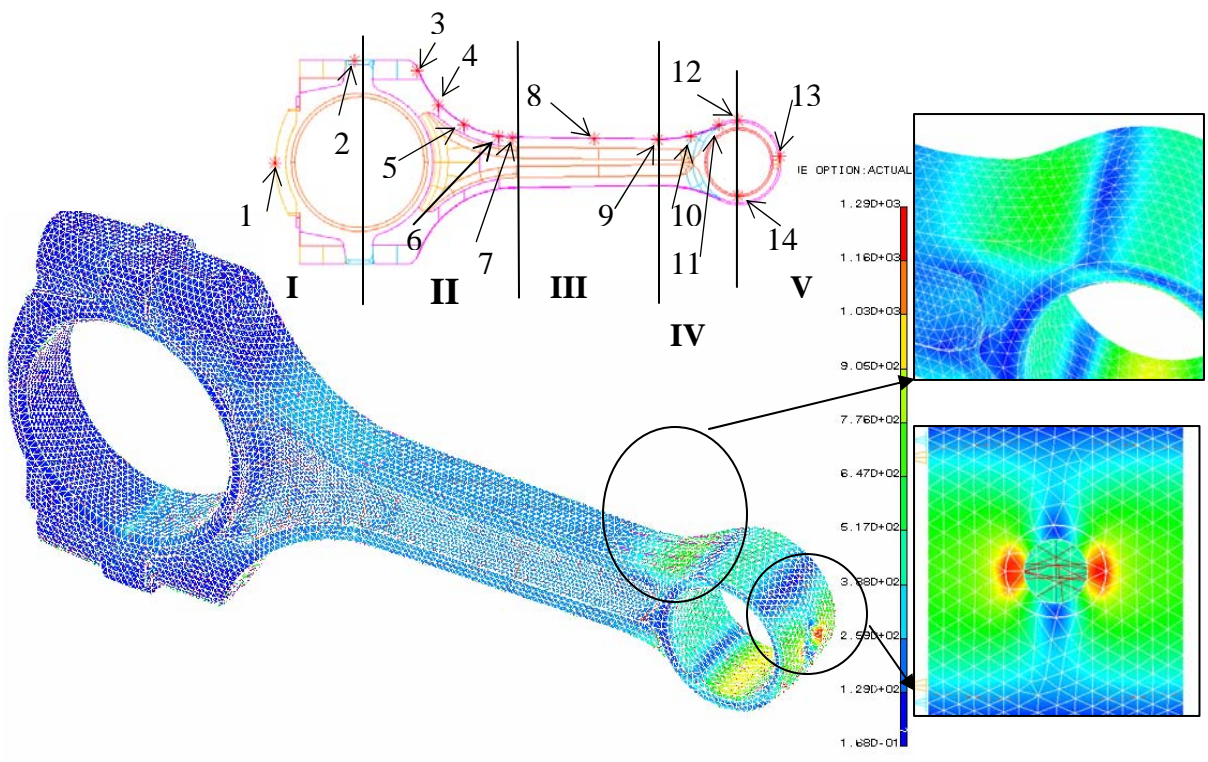


Figure 4.16: von Mises stress distribution with static tensile load of 26.7 kN at piston pin end. The crank end was restrained.

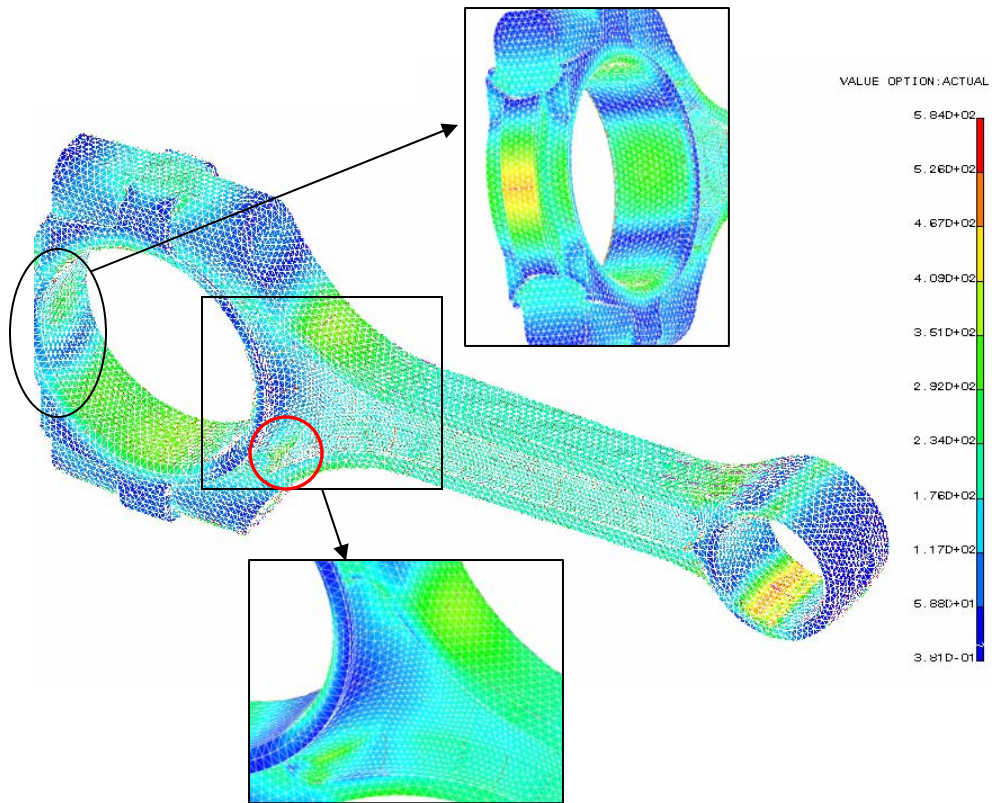


Figure 4.17: von Mises stress distribution with static tensile load of 26.7 kN at the crank end. The pin end was restrained.

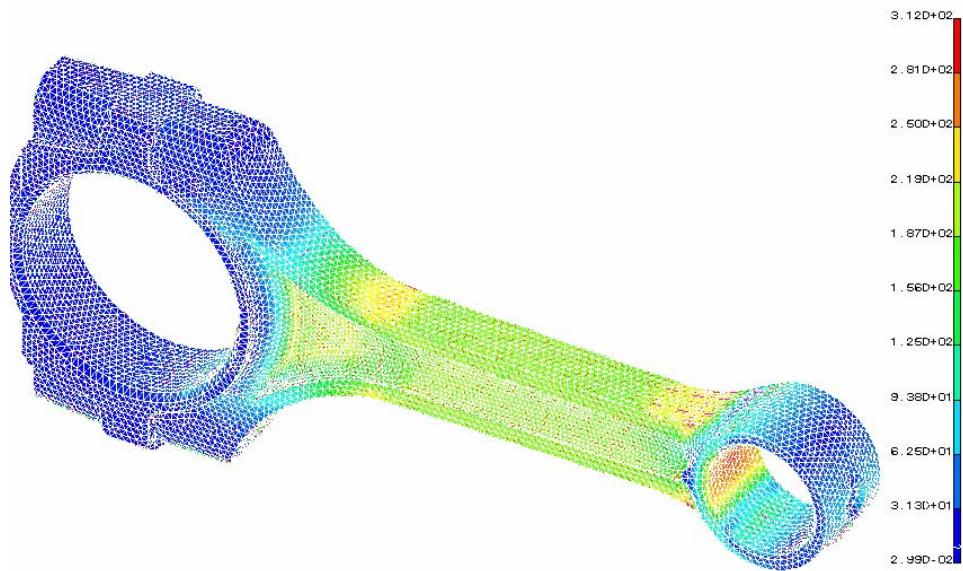


Figure 4.18: von Mises stress distribution with static compressive load of 26.7 kN at piston pin end. The crank end was restrained.

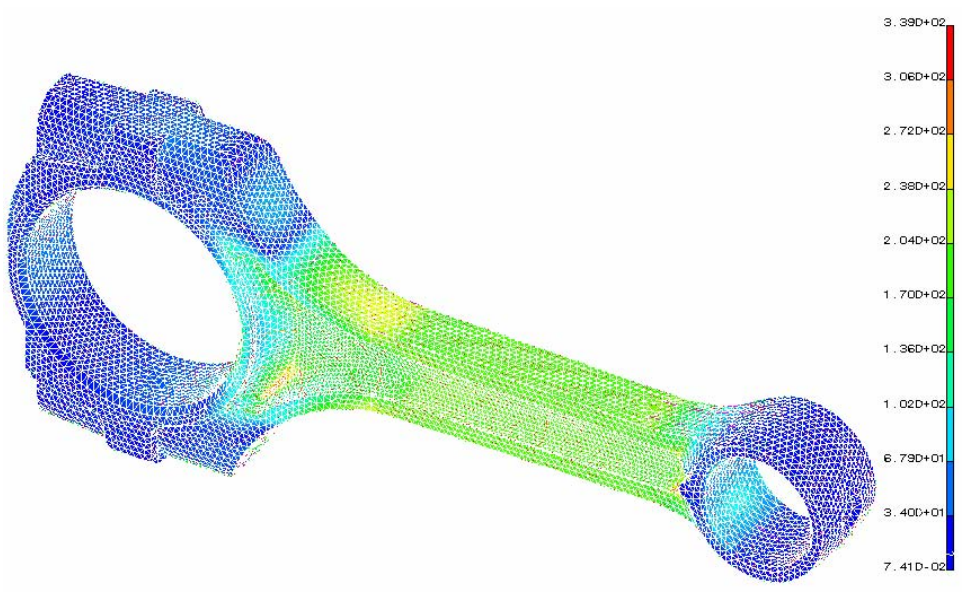


Figure 4.19: von Mises stress distribution with static compressive load of 26.7 kN at the crank end. The piston pin end was restrained.

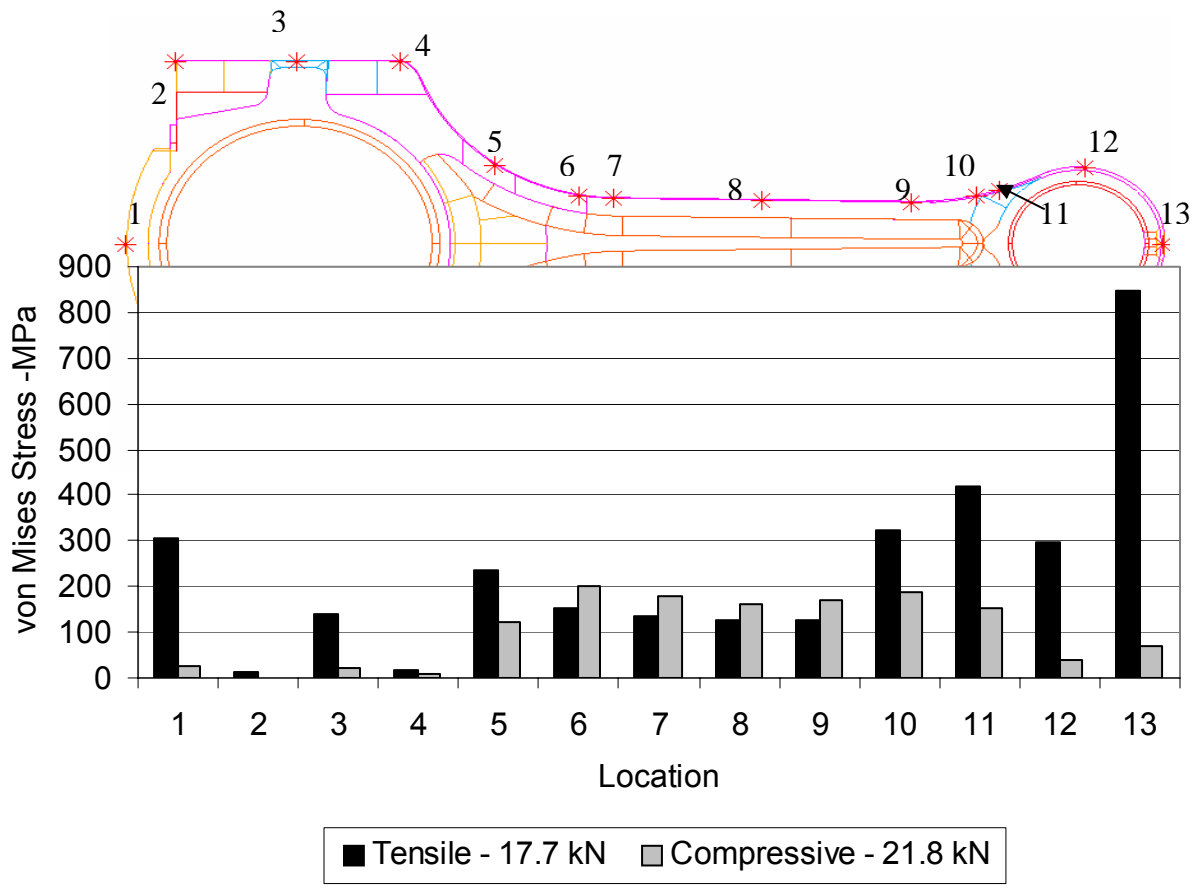


Figure 4.20: von Mises stress at a few discrete locations on the mid plane labeled on the connecting rod, along the length, for tensile (17.7 kN) and compressive loads (21.8 kN).

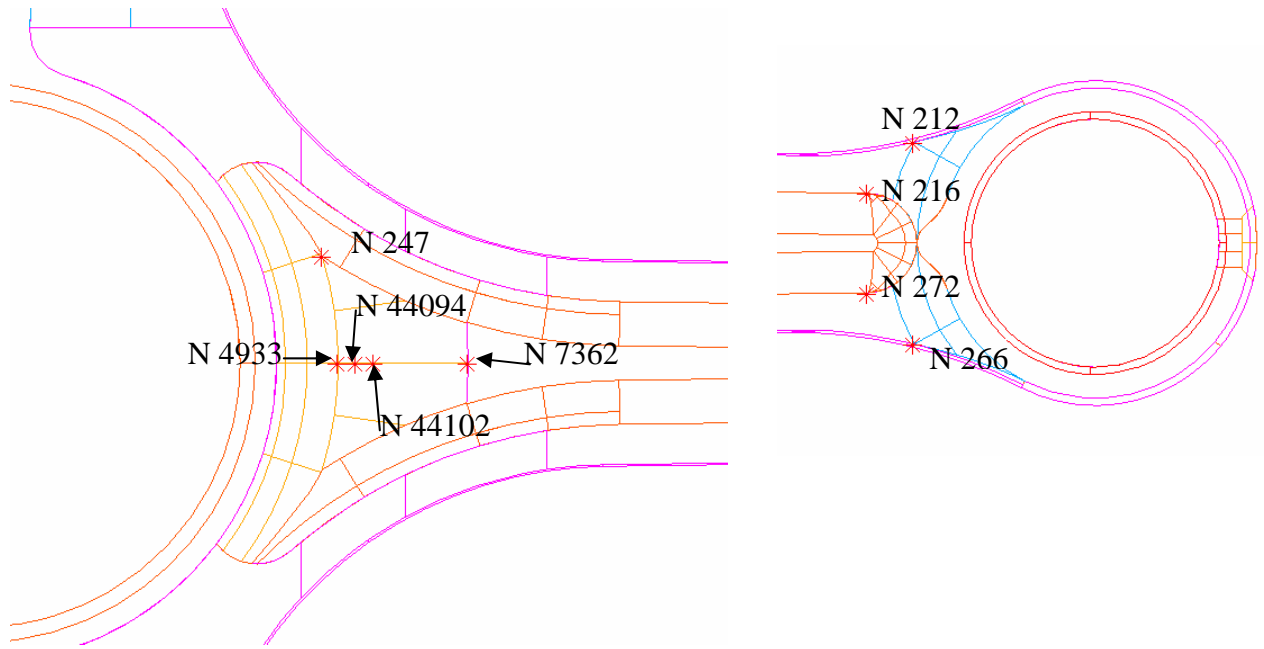


Figure 4.21: Location of the nodes in the web region near the crank end and the pin end transitions, the stresses at which have been tabulated in Table 4.2.

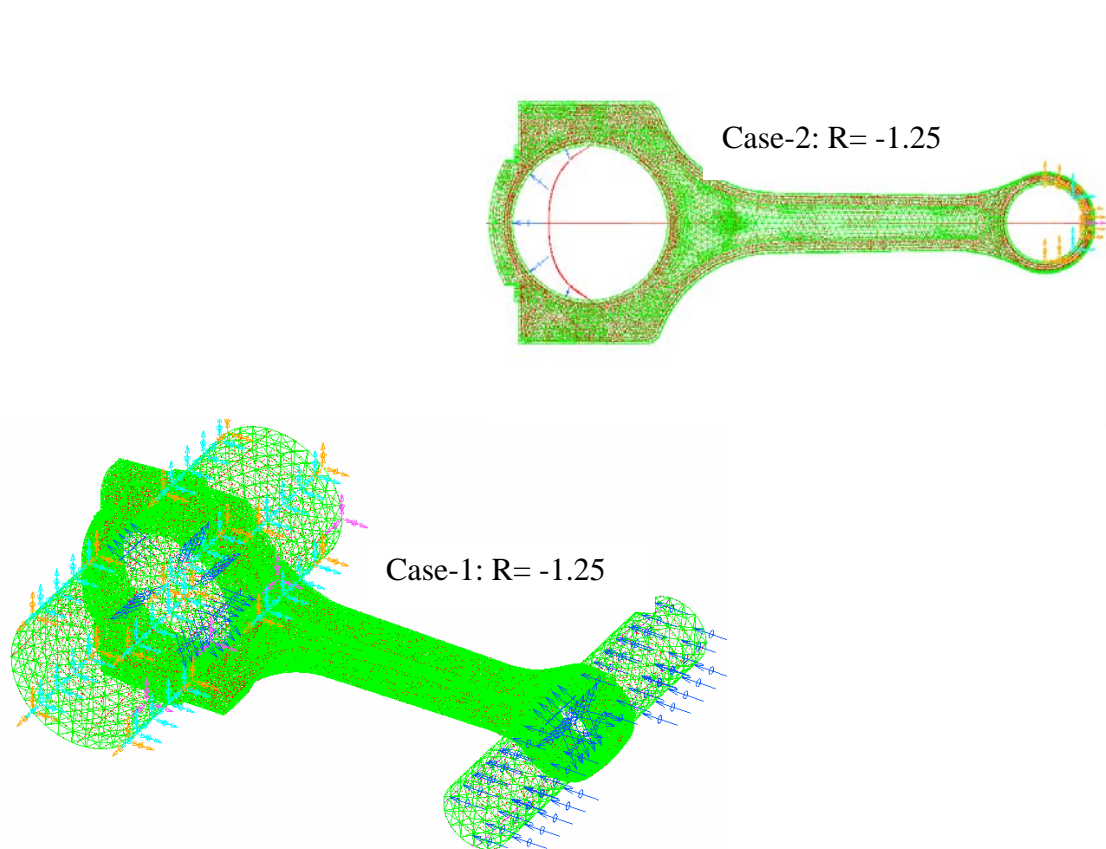
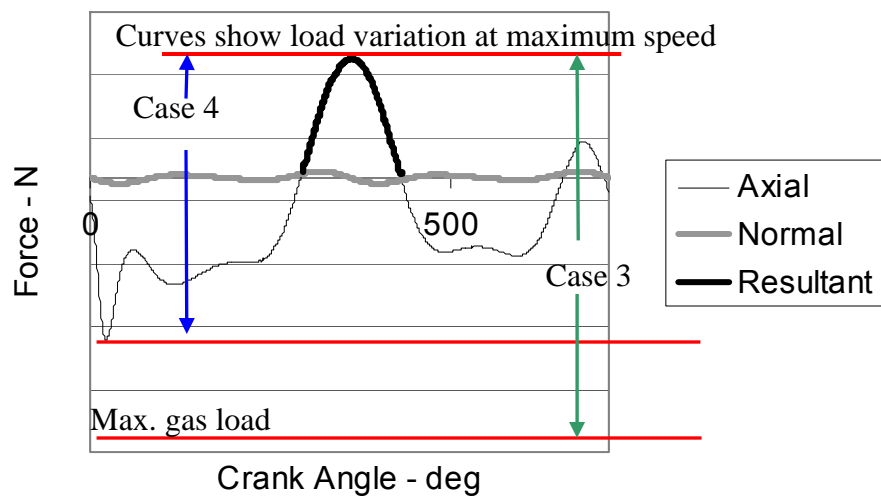


Figure 4.22: Schematic representation of the four loading cases considered for analysis.

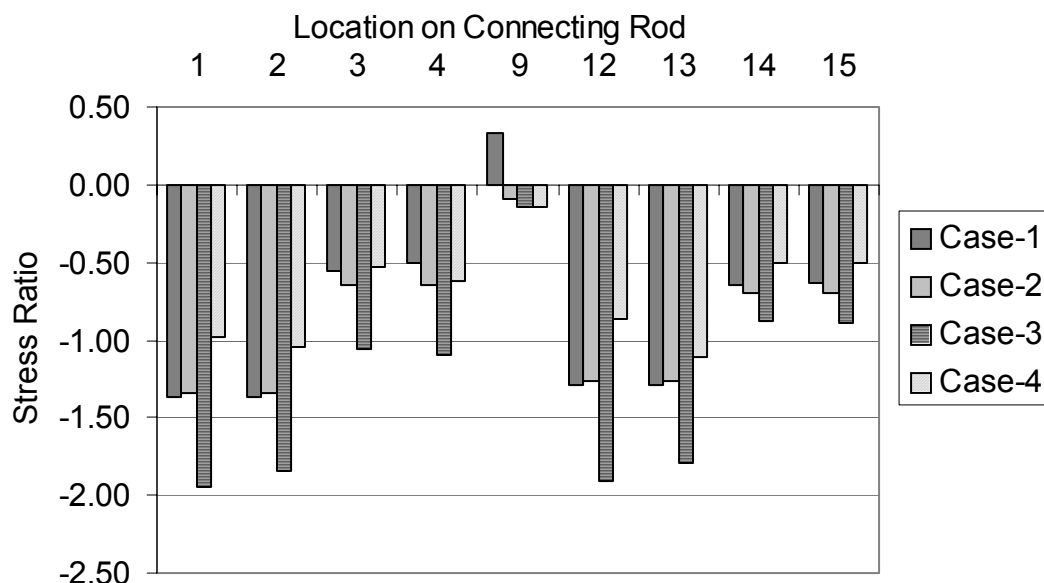


Figure 4.23: Stress ratios at different locations (shown in Figure 3.5) and for different FEA models. Case-1 is the test assembly FEA, Case-2 is the connecting rod-only FEA (with load range comprising of static tensile and compressive loads for both Case -1 and Case-2), Case-3 is the FEA with overall operating range under service condition, Case-4 is the FEA with operating range at 5700 rev/min under service operating condition. All cases are shown in Figure 4.22.

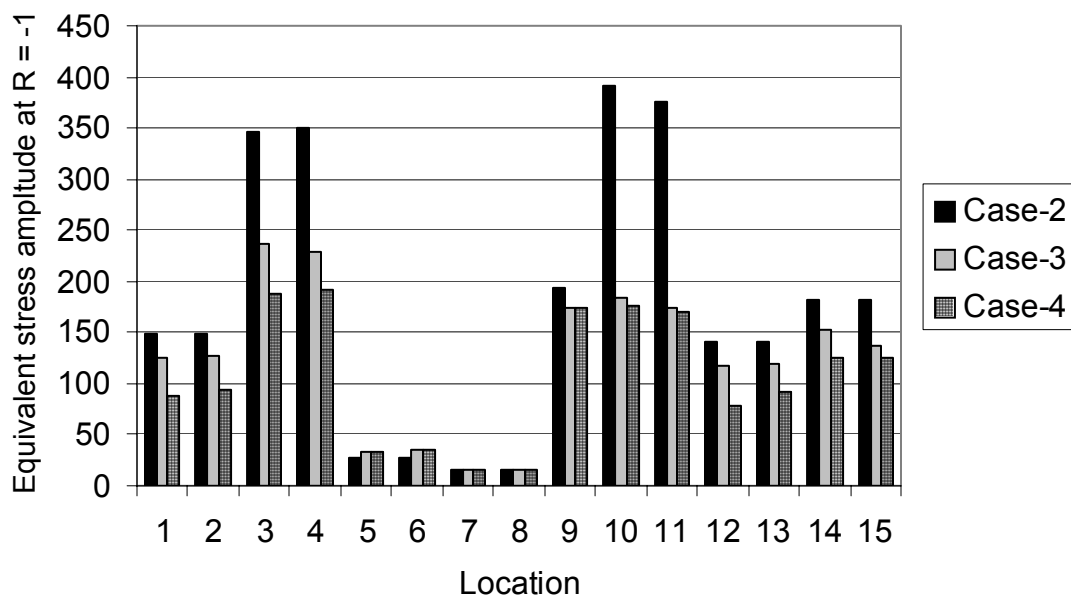


Figure 4.24: Figure shows a comparison of the equivalent stress amplitude at $R = -1$ (MPa) under three cases. Case-2 is the connecting rod-only FEA (with range comprising of static tensile and compressive loads), Case-3 is the FEA with overall operating range under service condition, Case-4 is the FEA with operating range at 5700 rev/min under service operating condition.

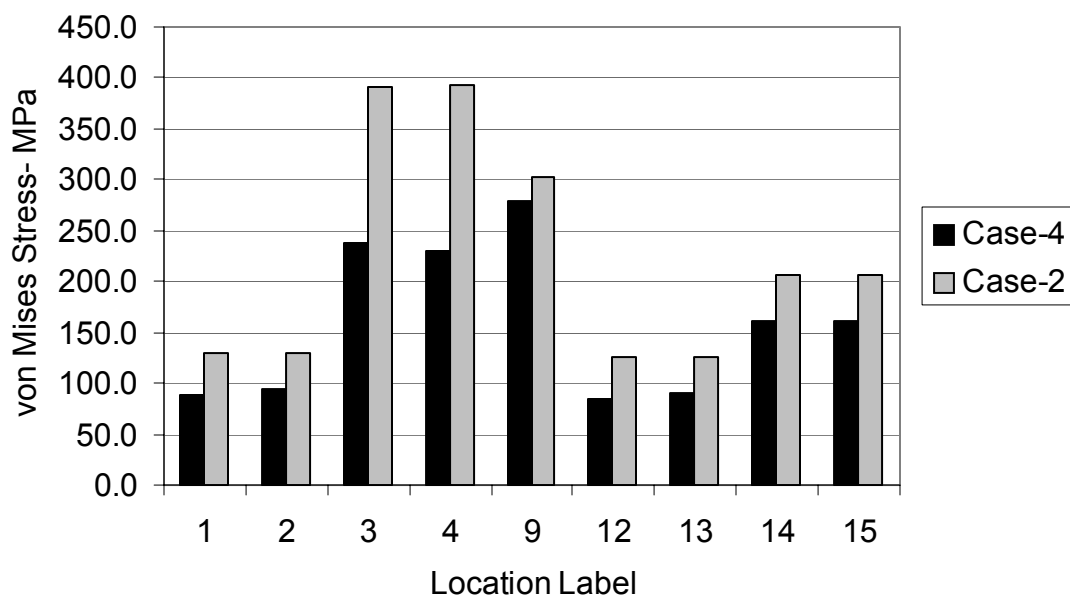


Figure 4.25: Maximum tensile von Mises stress at different locations on the connecting rod under the two cases. Case-2 is the connecting rod-only FEA (with range comprising of static tensile and compressive loads), and Case-4 is the FEA with operating range at 5700 rev/min under service operating condition.

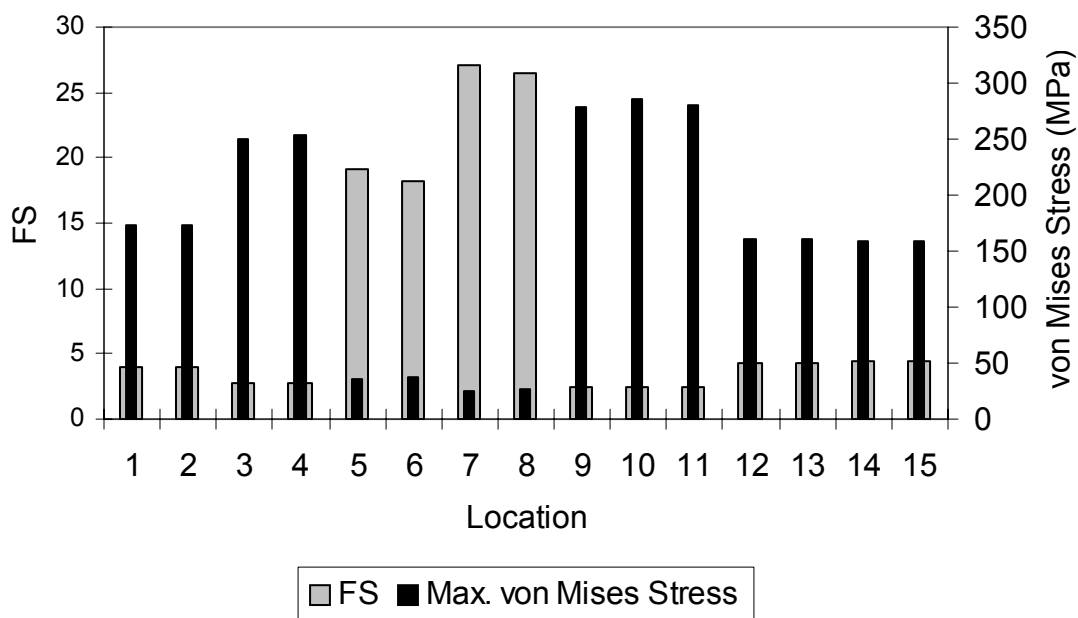


Figure 4.26: The factor of safety, ratio of yield strength to the maximum stress, for locations shown in Figure 3.5 and the maximum von Mises stress in the whole operating range.

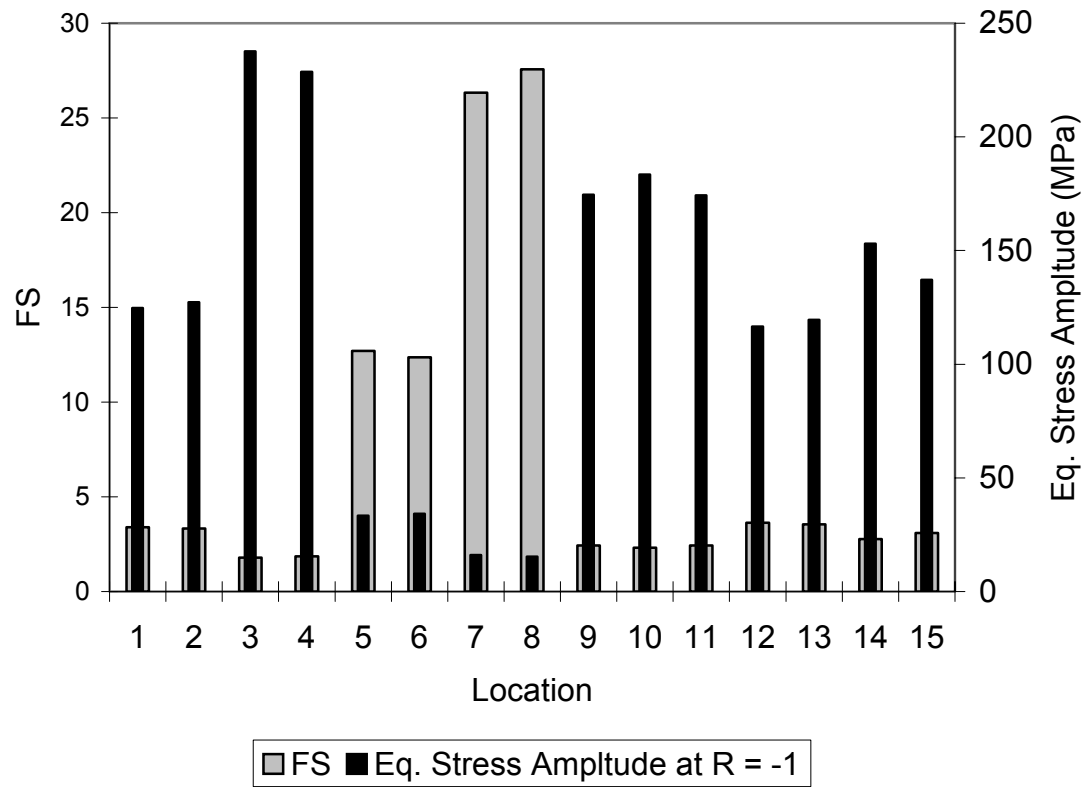


Figure 4.27: The factor of safety, ratio of the endurance limit to the equivalent stress amplitude at $R = -1$, at the locations shown in Figure 3.5 and the equivalent stress amplitude at $R = -1$ considering the whole operating range.

5. OPTIMIZATION

Chapter 4 identifies the potential for weight reduction in the existing connecting rod. It also highlights the fact that if the component is designed on the basis of axial static load or a load range based on the load variation at the crank end, it will be overdesigned. In actual operation, few regions of the connecting rod are stressed to much lower stress levels than under static load corresponding to the load at the crank end. The objective is to optimize the connecting rod for its weight and manufacturing cost, taking into account the recent developments.

Optimization carried out here is not in the true mathematical sense. Typically, an optimum solution is the minimum or maximum possible value the objective function could achieve under the defined set of constraints. This is not the case here. The weight of the new connecting rod or the ‘optimized connecting rod’ is definitely lower than the existing connecting rod. But this may not be the minimum possible weight under the set of constraints defined. What has been attempted here is an effort to reduce both the weight and the manufacturing cost of the component. Rather than using numerical optimization techniques for weight reduction, judgment has been used. The quantitative results were examined qualitatively, and the structure modified. Since this optimization task was performed manually, considering manufacturing feasibility and cost, it cannot be guaranteed that the weight of the ‘optimized part’ is the minimum weight. Cost reduction has been attempted indirectly by using C-70 steel. C-70 steel was developed

not long ago, which is fracture crackable. This fracture cracking technology is one of the factors that is responsible for the European connecting rod market share shown in Figure 1.1. It eliminates sawing and machining of the rod and cap mating faces and is believed to reduce the production cost by 25% (Reppen, 1998).

It is difficult, if not impossible, to create a mathematical statement for optimization taking into account cost, manufacturability, and weight simultaneously. For this optimization problem, the weight of the connecting rod has very little influence on the cost of the final component. Change in the material, resulting in a significant reduction in manufacturing cost, was the key factor in cost reduction. As a result in this optimization problem, the cost and the weight were dealt with separately.

The following factors have been addressed during the optimization: the buckling load factor, the stresses under the loads, bending stiffness, and axial stiffness. All of these have been checked to be within permissible limits. This chapter discusses the constraints under which weight was reduced, and how the optimized connecting rod compares with the existing one. It should be noted that the assembly-induced stresses are not included in the analysis.

5.1 OPTIMIZATION STATEMENT

Objective of the optimization task was to minimize the mass of the connecting rod under the effect of a load range comprising the two extreme loads, the peak compressive gas load and the *dynamic tensile load* corresponding to 360° crank angle at 5700 rev/min, such that the maximum, minimum, and the equivalent stress amplitude at $R = -1$ are within the limits of the allowable stresses. The production cost of the connecting rod was

also to be minimized. Furthermore, the buckling load factor under the peak gas load has to be permissible. The connecting rod has to be interchangeable with the existing one in the current engine. This requires some of the dimensions in the existing connecting rod to be maintained. These dimensions are discussed in detail in Section 5.2.4.

Mathematically stated, the optimization statement would appear as follows:

Objective: Minimize Mass and Cost

Subject to:

- Tensile load = *dynamic tensile load* corresponding to 360° crank angle at 5700 rev/min.
- Compressive load = peak compressive gas load.
- Maximum stress < Allowable stress.
- Equivalent stress amplitude < Allowable stress amplitude (for 10^6 cycles).
- Side constraints (Component dimensions).
- Manufacturing constraints.
- Buckling load > Factor of safety x the maximum gas load (Recommended factor of safety, 3 to 6).

5.2 CONSTRAINTS

5.2.1 Applied loads

The load range under which the connecting rod was optimized is comprised of the tensile load at 360° crank angle at 5700 rev/min and the compressive load of 21.8 kN, as discussed in the previous chapter. The compressive load of 21.8 kN is independent of the

geometry of the connecting rod. The tensile load is, however, dependent upon the specific geometry, as it is a function of the mass, moment of inertia, and location of C.G.

5.2.2 Allowable stress

Allowable stress is the ratio of yield strength to the factor of safety. A concept similar to factor of safety, the failure index (FI), was used in this work due to ease of processing the FEA results. The ratio of the von Mises stress in the existing geometry to the yield strength of the existing material, referred to as the failure index (FI), was obtained. The material chosen for the optimized connecting rod was C-70 due to its fracture crackability. C-70 has a percent elongation of 27%, and the monotonic stress-strain curve (Adila, 2004) shows the behavior of a relatively ductile material. As a result, the FI was defined with respect to the yield strength, rather than the ultimate tensile strength. The factor of safety with respect to the ultimate tensile strength has also been determined and is discussed later in the chapter. As the name implies, failure index will be an indication of the failure possibility. The closer the FI to one, the higher the possibility of failure. A FI or factor of safety was assumed based on work by previous researchers. Either the assumed FI or the FI in the existing component, whichever was higher, was used for obtaining the allowable stress at a given location or region of the connecting rod.

One such critical location is the oil hole at the piston pin end of the connecting rod. FEA results predict a higher FI at this region than the assumed one. Since the new material has lower yield strength and fatigue limit, the region was redesigned to maintain the same FI as the existing connecting rod. At other locations the FI predicted by FEA for the existing geometry and material (connecting rod) was lower than the assumed value.

As a result, the FI at these locations was raised closer to the assumed value in the optimized part.

The factor of safety applied to the yield strength in this work was 2.1, which corresponds to a FI of 0.48. The choice was based on the guidelines recommended by Norton (1996) and also on the ratio of the tensile strength to the tensile stress at a critical location in the work published by Folgar *et al.*(1987). In Folgar *et al.* study, the maximum tensile stress was 262 MPa and the tensile strength was 552 MPa, for a connecting rod made of 50-55% by volume Fiber FP reinforced Aluminum casting. Notice that Folgar *et al.* (1987) used factor of safety with respect to ultimate tensile strength. In this work, FS is defined with respect to the yield strength, and will be higher if defined with respect to the ultimate tensile strength. The factor of safety used in this work is adequate since, the factors unaccounted for are the angular acceleration of the crank, which can increase or decrease forces by about 1%, and the assembly stresses (assembly in engine). Bending stresses can occur due to eccentricities, crankshaft and case wall deformations, and inertia forces. The bending stresses resulting from inertia were determined for the existing connecting rod and it was found that the bending stresses were about 26% of the maximum stress at the section through location 12. Sonsino and Esper (1994) carried out stress analysis in an engine in which the bending stresses amounted to only 10% of the axial stresses for a PM connecting rod. This bending stress included the stresses resulting from inertia, eccentricities and wall and crankshaft deformations. Therefore, it can be concluded that bending stresses resulting from eccentricities and crankshaft and wall deformations are small in magnitude. Bending stresses resulting from inertia have been accounted for and discussed later in this

chapter in Section 5.3. This leaves only the bending stresses resulting from eccentricities and wall deformations, which can now be assumed to be less than 10%, as the unaccounted factor. Though Sonsino and Esper (1994) performed strain analysis on a PM connecting rod, similar bending stresses resulting from eccentricities, case wall, and crankshaft deformation can be expected in a forged steel connecting rod, since they are dependent on machining of the connecting rod. It is possible to use machining lines with the same capabilities for connecting rods made of either processes.

The distribution of the FI with respect to the yield strength of the material under tensile and compressive loads for the existing component was obtained. Figures 5.1 and 5.2 show the FI distribution under tensile and compressive loads, respectively. Figure 5.1 indicates that under the dynamic tensile load, the oil hole has a FI of 0.7, which is the maximum FI in the component at this load. At the region around the partition on the piston pin inner surface where the load was applied, the maximum FI is about 0.5. Due to this region being very close to the boundary condition, the results may not be very accurate. For the length of the connecting rod between the crank end till nearly the piston pin center, the maximum FI for the existing connecting rod and material is about 0.4. Figure 5.2 indicates that under compressive load the maximum FI is 0.395.

For the optimized connecting rod, under tensile load, at the oil hole the maximum failure index should not exceed 0.7, which means that the stress at the oil hole should not exceed (0.7×574) , or 399 MPa. At the piston pin end the strength in the optimized connecting rod should be nearly the same as that in the existing component (due to lower confidence in the stresses at this location). The stresses at the oil hole are sensitive to the boundary conditions. Similar boundary conditions were used for both the existing and the

optimized connecting rods. Moreover, no failures were observed during testing of the connecting rod or reported by the OEM. Hence, the same high FI was maintained in the optimized connecting rod at the pin end region near the oil hole. As for the rest of the connecting rod, the FI could be 0.48 under the tensile and compressive loads, or the maximum von Mises stress could be 273 MPa (0.48×574). The FI discussed in the above section was with respect to the yield strength of the material. The FI with respect to the ultimate tensile strength was also determined and is discussed in Section 5.3.

5.2.3 Allowable stress amplitude

Allowable stress amplitude is the ratio of the endurance limit to the factor of safety. The connecting rod is expected to survive between 10^8 to 10^9 cycles. This is the range into which the expected computed life will fall, assuming that the vehicle will be in service for 200,000 miles while operating at an average speed of 40 miles/hr, with an engine speed of 2500 rev/min. Since the S-N curve of steel is known to have a knee at about 10^6 cycles, the fatigue strength at 10^6 cycles can represent the endurance limit for the material. For the connecting rod to have life on the order of 10^8 to 10^9 cycles, the equivalent stress amplitude for $R = -1$ at various locations on the connecting rod must be less than the allowable stress amplitude. Allowable stress amplitude is obtained by applying a factor of safety to the endurance limit. The endurance limit for steels is known to exist under non-corrosive conditions and for constant amplitude loading. Sonsino and Esper (1994) derived endurable stress amplitude, for the connecting rod they designed, at 2×10^6 cycles. Factor of safety was applied to the resulting endurable stress amplitude. Their PM connecting rod was tested in an engine and found to be satisfactory.

The material chosen for the new connecting rod is C-70, which is believed to decrease the total cost by 25% by virtue of its fracture crackability (Repgen, 1998). Cost aspects have been discussed in Section 5.6. Properties of the existing material and C-70 material are listed and compared in Table 5.1. Note that while the ultimate tensile strength is nearly 3% higher, the yield strength of C-70 is 18% lower and the endurance limit is 20% lower than that of the existing forged steel material. The endurance limit for the C-70 material is calculated to be 339 MPa, whereas for the existing forged steel material it is 423 MPa.

The surface finish factor has not been taken into account, since the shot peening process negates the negative impact that the forged surface finish has on the fatigue life, by inducing compressive residual stress on the surface.

The equivalent stress amplitude for $R = -1$ at each node in the FE model is compared with the allowable stress amplitude of the material. This is tantamount to comparing the local stresses with the endurance limit of the material, rather than comparing nominal stress across a section with the endurance limit. Since FEA is used, the stress concentration effect is inherently accounted for and the stress concentration factor was not needed.

The FI distribution for the existing geometry with respect to the endurance limit of the existing material under cyclic load was obtained. The cyclic load consists of the tensile load at 360° crank angle at 5700 rev/min as one extreme, and maximum compressive load of 21.8 kN as the other extreme. Figure 5.3 shows the distribution. The approach used in Section 5.2.1 for deciding the stress limits has been used here. A FI or factor of safety was assumed based on work by previous researchers. Either the assumed

FI or the FI in the existing component, whichever was higher, was used for obtaining the allowable stress amplitude at a given location or region of the connecting rod. This is further explained in the following paragraph.

Sonsino and Esper (1994) used a safety factor of 1.66 on the endurable load amplitude for a PM connecting rod. The same factor was used for the allowable stress amplitude here. The allowable stress amplitude was thus obtained by applying a factor of safety of 1.66 to the endurance limit of the material. The allowable equivalent stress amplitude at $R = -1$ would then be 204 MPa ($338/1.66$), or a FI of 0.602. The maximum FI over the equivalent stress amplitude for $R = -1$, with respect to the endurance limit of the material (424 MPa) for the existing connecting rod is 0.87 at the oil hole, which is greater than 0.602 (maximum allowable FI). As a result, for the optimized connecting rod to be made of C-70, the maximum FI of 0.87 was used at the oil hole. This means that the maximum allowable stress amplitude for $R = -1$ condition is 295 MPa at the oil hole. For other regions of the optimized connecting rod, from the crank end to the pin end, the equivalent stress amplitude for $R = -1$ could be 204 MPa. The existing connecting rod has a higher factor of safety (or lower FI) at other locations.

5.2.4 Side constraints

The optimized connecting rod is expected to be interchangeable with the existing one. The diameters of the crank pin hole, $D1$, the piston pin hole, $D2$, the overall thickness of the connecting rod, $W1$, and the center to center distance, $L1$, cannot be changed. These dimensions are indicated in Figure 5.4. The piston pin end fits under the piston and is supposed to clear off the piston skirt and the piston bottom when in

operation. The outer diameter of the piston pin end, D3, and the dimension, H1, especially at the piston pin transition are ordinarily constrained based on the space available under the piston. The design and layout of this region and the entire space was not available. However, these dimensions (D3 and H1) had to be increased to satisfy stress constraints. The dimensions of the bolts and their holes were also retained. This is because modeling the bolt-connecting rod interface is a complex problem and beyond the scope of this work. The dimension H2 was also not changed. All other dimensions of the connecting rod could be varied, within practical limits.

5.2.5 Buckling load

Linear buckling analysis was performed on the connecting rod with the compressive load of 21.8 kN, the maximum compressive load in the entire cycle. The buckling load factor should be between 3 and 6 (Bhandari, 1994). This is further discussed in Section 5.3.

5.3 OPTIMIZATION UNDER DYNAMIC LOAD

The software used I-DEAS has an optimization module. This optimization module in I-DEAS has the capability to perform optimization under a set of loads. In the case of this particular optimization problem, these load sets consist of the tensile load at 360° crank angle at 5700 rev/min and the peak compressive gas load. von Mises stress under these loads can be constrained. However, one of the constraints defined in Section 5.1 uses equivalent stress amplitude at $R = -1$ (for life of 10^6 cycles). I-DEAS does not offer the capability to define the equivalent stress amplitude at $R = -1$ as a constraint.

The chamfers between the ribs and the web in the connecting rod accounted for a considerable portion of the cross sectional area. The dimensions of these chamfers varied over the length of the connecting rod. Problems encountered while using the optimization module with these chamfers, that had to do with the definition of the geometry, lead to using an iterative manual procedure using intuition and judgment.

Figures 4.26 and 4.27 were used as a guide to begin optimization. Since the objective was also to reduce the total production cost of the connecting rod, the material was changed from the existing forged steel to C-70 steel, which is fracture crackable. This reduced the yield strength from 700 MPa to 574 MPa. With reference to the constraints of maximum stress and equivalent stress amplitude in Section 5.1, as discussed in Sections 5.2.2 and 5.2.3, the allowable maximum von Mises stress is 273 MPa and allowable equivalent stress amplitude at $R = -1$ is 204 MPa. The loads under which the results in Figures 4.26 and 4.27 were obtained were as defined in Section 5.1. Comparing the results in Figure 4.26 with the stress value of 273 MPa and the results in Figure 4.27 with 204 MPa indicates that regions near locations 1, 2, 12, 13, 14, and 15 (i.e. essentially the entire shank of the connecting rod) offered the greatest potential for weight reduction. Regions near locations 3, 4, 9, 10, and 11 were already highly stressed. The regions near locations 5, 6, 7, and 8 also offer potential for weight reduction. This region involves complex interface between the bolt and the connecting rod and the FEM would be complex. As a result, it was decided that this region would not be the focus in this study.

The steps taken for achieving weight reduction can be generalized. The guidelines followed are with reference to Figure 5.4. In the shank, the rib and the web dimensions,

T1 and W3, were reduced. To maintain forgeability, there was a limit to which dimensions W3 and T1 could be reduced. The section modulus of the new connecting rod should be high enough to prevent the bending stresses from increasing. In order for the section modulus to be as high as possible, the width of the rib, W2, was increased and equated to W4 (i.e. it was increased from 12 mm to 15.9 mm). Obviously the higher the value of W2, the higher the section modulus. The outer diameter of the pin end, D3, was increased and the center of the outer surface was offset by O1 in order to add more material at the oil hole. It was required to increase the strength in this region due to the lower yield strength and endurance limit of C-70 steel, as compared to the existing forged steel. O1 is the offset between the centers of the arcs with diameters D3 and D2. In order to reduce the stress concentration effect at the transition to the pin end the distance between the ribs of the connecting rod, H1, was increased. The current connecting rod shank slightly tapers (taper of less than 1°) down from the crank end to the pin end. For the optimized connecting the shank was parallel since the dimension H1 had to be increased. Based on the guideline outlined by Repgen (1998), the jig spot was relocated from the existing location to be entirely on the cap. The radii RB and RS were increased and L2 decreased to reduce stresses, since relaxing the radii has the effect of reducing the stress concentration effect. Dimensions W1, H2, L1, D1 and D2 were not changed to maintain component interchangeability with the existing connecting rod. It must be mentioned that in addition to the dimensions labeled in Figure 5.4, dimensions of chamfers in the web and the cap of the connecting rod were varied during optimization.

After following these guidelines and a few iterations, the geometry of the new connecting rod, as shown in Figure 5.5, was found to be satisfactory in terms of satisfying

the constraints listed in Section 5.1. The mass, moment of inertia, and the center of gravity of the optimized connecting rod were determined and used to obtain the load variation over the entire cycle of operation of the connecting rod under service operating conditions. All other parameters (i.e. the piston mass, the engine speed, the pressure crank angle diagram) were maintained the same as for the previous case (i.e. the existing connecting rod). This step of determining the load variation was required for every geometry analyzed. The load corresponding to 360° crank angle at 5700 rev/min (different from the previous case due to different inertia properties) and the gas load of 21.8 kN were used to perform the FEA. Loads were applied as explained in Section 3.3.1 using the loads tabulated in Table 5.2. Table 5.2 lists few of the results from the dynamic load analysis performed for the optimized connecting rod.

Following the FEA of this component, the results were processed to obtain the distribution of the FI with respect to the yield strength (of C-70) under the action of the tensile and compressive loads, described in Section 5.1, and with respect to the endurance limit of the C-70 steel under the action of the cyclic load comprising the loads listed in Section 5.1. When computing FI with respect to the endurance limit, the equivalent stress amplitude at $R = -1$ is computed using Equations 4.1, 4.2, and 4.3. The distributions are shown in Figures 5.6 through 5.8.

Figure 5.6 indicates that the maximum FI under tensile load at the oil hole is 0.68, which is less than the maximum FI at the oil hole for the existing connecting rod. The maximum FI under the tensile load for the region of the connecting rod between the crank end and nearly the center of the piston pin end is 0.454. This is less than the limit of 0.48 discussed in Section 5.2.2. In Figure 5.6, the inset shows FI distribution on the

surface of the pin end bore. Note that the FI is around 0.63, which is higher than the limit of 0.48. In a study which involved FEA of the connecting rod with the piston pin and the bushing, it was observed that the stresses in this region (bore of the pin end) were significantly lower than the stresses predicted with cosine loading. From the results of this FE analysis (with piston pin and bush) the FI of this region was calculated to be 0.42 (FS of 2.38), which is less than the limit of 0.48 under tensile load. Figure 5.7 indicates that the maximum FI under compressive load is 0.46, again less than the limit of 0.48. Figure 5.8 indicates that the maximum FI with respect to the endurance limit of 339 MPa is 0.79 at the oil hole, which is less than the FI for the existing component of 0.87. The maximum FI for other regions is 0.48, less than the limit of 0.602. Once a forgeable connecting rod satisfied the stress constraints, linear buckling analysis was performed on the connecting rod under the compressive load of 21.8 kN. The Buckling load factor for the optimized connecting rod is 9.6, which is more than adequate. Mass of the optimized connecting rod is 395.9 gms, lower than the mass of existing connecting rod by 10%. Note that this weight does not include the weight of the bolt heads and is the weight of the connecting rod as shown in Figure 5.5. The 10% weight reduction is computed when compared with the existing connecting rod, which did not include the bolt heads either.

With the failure index being either equal to that of the existing component or less than the limit set, the design is clearly acceptable. Table 5.3 compares the minimum factor of safety (FS) for the existing and the optimized connecting rods in different regions. These regions have been identified in Figure 5.9. The FS listed in the Table 5.3 are the minimum FS in the region. Regions I and V, as shown in Figure 5.9, are the most severely stressed regions (the cap and pin end) under the tensile load (Section 5.1). Once

again, higher weight reduction may be achieved by applying formal optimization techniques (i.e. by automating the optimization) than what has been achieved here. The minimum FS with respect to the yield strength is 2.19 (with the exception of region V, the oil hole region), and 3.68 with respect to the ultimate tensile strength. By automating the optimization process the FS in region II under the cyclic load can be made equal to 1.66 (assumed FS discussed in Section 5.2.3) from the current value of 1.69, which can reduce the weight further.

Based on the discussion so far, it can be concluded that the optimized connecting rod which was optimized under cyclic load (Section 5.1) has sufficient fatigue strength, because stress amplitude at $R = -1$ is less than the allowable stress amplitude, and it has sufficient strength against yielding, because maximum stress is below the allowable stress. It also has sufficient strength against buckling (load factor of 9.6).

As already pointed out in Section 4.1, there does not exist an instant of time at which all the points on the connecting rod experience maximum stress. This is evident from Figures 4.1 through 4.8, which shows stress variation for the existing connecting rod. At locations 1, 2, 12, and 13 maximum stress occurs at 348° crank angle (among the crank angles at which FEA was performed), whereas at locations 3, 4, 7, 8, 9, 10, and 11 maximum stress occurs at 360° crank angle (among the crank angles at which FEA was performed). At locations 5 and 6 maximum stress occurs at crank angles of 336° and 396° , respectively. Since the optimization was performed under dynamic loads at 360° crank angle (at 5700 rev/min), a concern is whether the optimized connecting rod with its new mass and inertia distribution has stresses below the limits at other crank angles. The concern is due to the fact that in the regions near locations 1, 2, 12 and 13 (Figure 3.5),

under the effect of the bending stress the total stress exceeds the stress at 360° crank angle. The following paragraphs address this concern.

Among the locations selected, regions near locations 5, 6, 7, and 8 are at low levels of stress, and therefore, are not of concern. At locations 3, 4, 9, 10, 11, 14, and 15 the maximum stress occurred at 360° crank angle in the existing connecting rod. The same behavior can be expected for the optimized connecting rod.

From Table 5.3, the maximum stress in region II (where locations 1 and 2 are located) at 360° crank angle can be computed to be 222 MPa. From Figure 4.1, showing the stress variation for locations 1 and 2 for the existing connecting rod, it is observed that the maximum stress occurs at 348° crank angle. The bending stress (12 MPa) is about 11% of the axial stress (85 MPa) in that section at 348° crank angle. The weight reduction in the optimized connecting rod also resulted in a reduction of the bending section modulus (I/y_{\max}). For the section through location 1, the section modulus reduced by 2.8% for the optimized connecting rod, as compared to the existing one. As a result, the bending stress for the new connecting would be higher by about 2.8% (assuming the bending moment to remain the same as in the existing connecting rod, even though the moment actually decreases due to mass reduction). A 13.8% increase (i.e. 11% + 2.8%) in 222 MPa stress equals 253 MPa, still within the limit of 273 MPa (maximum allowable stress). It should also be pointed out that the axial stress at 348° crank angle is lower than the axial stress at 360° crank angle, so the actual stress will be lower than 253 MPa.

The stress in region III (for locations 12 and 13) at 360° crank angle (tensile load) is of the order of 116 MPa. This leaves ample margin for bending stresses. In region IV the maximum stress at 360° crank angle is 229 MPa, below 273 MPa, and the bending

stresses are very low in this region. The above discussion validates that the optimized design is acceptable. It should be noted that the load at 362° crank angle will be higher than the load at 360° crank angle by less than 1%.

Just as the maximum stress was confirmed to be within the limits of allowable maximum stress, it is essential to verify that the equivalent stress amplitude at $R = -1$ is within the allowable stress amplitude at other crank angles. In region II the minimum FS from Table 5.3 under cyclic load is 1.69. This minimum FS occurs at a location where the bending stresses are low and the maximum stress does in fact occur at 360° crank angle (confirmed using results of Chapter 4). So, there is no concern of the allowable stress amplitude being violated at other crank angles.

When discussing the FEA results in Chapter 4, the load range comprised the entire cycle ($0^\circ - 720^\circ$) at 5700 rev/min and the peak compressive gas load. However, while optimizing the connecting rod, the load range comprised only the load at 360° crank angle at 5700 rev/min and the maximum gas load. Using results of Chapter 4, it was found that the equivalent stress amplitude at $R = -1$ at a few locations of concern (i.e. locations 2 and 13) between the two load cases differed by less than 2.5%. In addition to the slight increase in the equivalent stress amplitude at $R = -1$ due to a difference in the load range considered, one can expect it to increase also due to the decrease in the section modulus of 2.8% as previously discussed. The equivalent stress amplitude at $R = -1$ increased only by about 1% for a 2.8% decrease in the section modulus. Therefore, in total, one can expect an increase in the equivalent stress amplitude by less than 3.5% at locations 2 and 13. No differences are observed for other locations (i.e., locations 1, 12, 14, and 15) between the two load cases.

From Table 5.3 the minimum FS under the cyclic load in region II (for locations 1 and 2) is 1.69 (very close to limit of 1.66). However, this minimum FS occurs at a location where the bending stresses are low and the maximum stress does in fact occur at 360° crank angle. In the optimized connecting rod for regions around locations 1 and 2, the maximum equivalent stress amplitude at $R = -1$ is 177 MPa and for regions around locations 12 and 13 the maximum equivalent stress amplitude at $R = -1$ is 152 MPa. Increasing the stress at these locations by 3.6% still keeps the stress within the limit of 204 MPa (Section 5.2.3).

Table 5.4 lists various material and geometric properties for the two connecting rods. The buckling load factor for the optimized connecting rod (9.6) is higher than the existing one (7.8). Since no absolute value of permissible displacement was available as a standard for comparison, a comparison has been made between the existing connecting rod and the optimized one. Note that, in spite of weight reduction the axial stiffness of the component has slightly increased (Table 5.4), and I_{ZZ} , which is the mass moment of inertia of the connecting rod about the axis normal to its plane of motion (z axis) and passing through its C.G., has slightly decreased. The weight is also listed for the two connecting rods. The weight does not include the weight of the bolt heads and is the weight of the geometry generated for FEA.

The optimized and existing connecting rod geometries have been superimposed in Figure 5.10. Notice that the pin end of the optimized connecting rod is slightly larger than the pin end of the existing connecting rod. The bore diameters at the crank and the pin ends are the same for the two connecting rods. Material removal from the transition near the crank end is obvious in this diagram. Figure 5.11 shows the isometric view of the

existing and the optimized connecting rod. Figure 5.12 shows a drawing of the optimized connecting rod. An edge radius of 1.5 mm is required for all the edges (correspondence with Mr. Tom Elmer from MAHLE Engine Components, Gananoque, ON, Canada). This radius is not shown in the drawing.

5.4 VALIDATION OF THE CRANK END DESIGN

The crank end of the connecting rod had to be redesigned. Based on the guidelines by Repgen (1998), the jig spot was relocated so that it would not be in the path of the fracture crack during the fracture cracking of the cap and rod. In order to validate the adequacy of the design, a more detailed FEA was performed. In this new FEA, the bolt holes were modeled, and the cap was split from the rod and connected with two bolts. The connection between the bolt and the rod, at the threads was modeled using spring elements with very high stiffness. This region was not modeled with great details, since the behaviour at the bolt-rod interface was not of interest, as the original design of the bolt was being retained. The behaviours at the cap-rod interface and of the rod and the cap under more realistic conditions were of primary interest. The abovementioned model captures the bolt effect for these behaviours adequately. The bolt pretension was modeled as shown in Figure 5.13. By applying the bolt pretension load as shown in the Figure 5.13, the behaviour of the rod and cap is captured appropriately, though the behaviour of the bolt itself is not. The bolt pretension was estimated to be 12.8 kN per bolt. It was estimated using theory of machine design (Shigley and Mischke, 1989) for a bolt torque of 20 Nm (specified in OEM workshop manual) for a bolt having major thread diameter of 7.82 mm. Contact elements were defined between the rod and the cap at their mating

surface. Contact elements were also defined between the bolt head and the bolt seat on the cap. The pin end was restrained, and a tensile load corresponding to 360° crank angle at 5700 rev/min and a compressive load of 21.8 kN were applied to the connecting rod, as discussed previously in Section 3.3.1 (tensile load from quasi-dynamic FEA and compressive load from static FEA). Thus two FEA models were solved, one with a tensile load and the other with a compressive load. The complete FEA model under tensile load is shown in Figure 5.14.

Figure 5.15 shows the von Mises stress variation and the displacements of the model just discussed under the tensile load. The displacement shape of the cap and the rod, especially at the rod-cap interface indicates that FEM was modeled appropriately.

The von Mises stress in the region of location 9 (Figure 3.5) predicted by the FEM in Figure 5.14 is 334 MPa. Also, the von Mises stress at the outer corner of rod-cap interface in Figure 5.15 is in excess of 400 MPa. These are above the limit of 273 MPa by a significant margin. Of the many nodes on the cap edge shown in Figure 5.16, the node with minimum radial displacement had a radial displacement value of 0.077 mm. This displacement is towards the center of the connecting rod bore. However, the clearance between the crank end bearing and the crankshaft is of the order of 0.026 mm for connecting rods in this size range (as it was in the case of Goenka and Oh, 1986; Makino and Koga, 2002).

A few cases were investigated to compare the rigidity of the connecting rod assembly (with the crank pin and bearing) as opposed to the rigidity of the connecting rod alone. These included connecting rod with a bearing, connecting rod with bearing in which the stiffness of the bearing was reduced to a very low value, and a connecting rod

with a pin (representing the crankshaft) having radial clearance of 0.026 mm. The connecting rod used in these cases had the cap integral to the rod.

Comparison of these results indicated that the rigidity of the connecting rod crank end increased with the bearing assembled in the crank end bore. Moreover, the stresses and displacements were significantly lower at critical location in the presence of the pin, indicating that its presence increased the rigidity of the crank end of connecting rod assembly (when compared with its behavior under cosine loading). The displacements at the region corresponding to the edge (shown in Figure 5.16) reduced significantly to lower than the clearance value. The only factor not accounted for in the analysis mentioned in this paragraph is the presence of the oil film. The oil film is not expected to reduce the rigidity.

The fracture surface at the cap-rod interface, is also known to increase stiffness due to a firm contact between the cap and rod (Park *et al.*, 2003). Moreover, from the discussion in the above paragraph it can be concluded that rigidity of the crank end is increased in the presence of the crankshaft and the bearing. As a result, springs were added across the opposite inner edges of the rod and cap to approximately model the above-mentioned stiffness. Several (twelve) springs with low stiffness (of 1697 N/mm which, as discussed later was found to be an under-estimated value) were added across the edges (Figure 5.16) of the cap at the rod-cap interface to uniformly increase the stiffness. Identical springs were added across the edges of the rod at the rod-cap interface. The resulting FEM is shown in Figure 5.17. Following the addition of the above stiffness, the maximum stress at the rod cap interface dropped to about 226 MPa, and the maximum stress at the crank end cap at location 9 dropped to 248 MPa, both within

permissible limits. The stress variation for the FEM shown in Figure 5.17 is shown in Figure 5.18. Stresses are within the maximum limit of 273 MPa. Note that the outer edge of the cap at the cap-rod interface is not affected by the springs attachments, even though stresses at the locations where the springs were connected in the inner edge were very high. The resulting displacement shape was similar to the one shown in Figure 5.15. The node with the minimum displacement on the inner edge, for the FEM shown in Figure 5.17, had a displacement value of 0.0367 mm. This is still more than the clearance between the bearing and the crankshaft. It can, therefore, be concluded that the stiffness assumed for the springs was not over-estimated, rather it was under estimated. Therefore, even though stresses are within permissible limits, they are still over-estimated at the interface.

Figure 5.19 shows the FEM of the assembled connecting rod under compressive load. The stress distribution for this FEM is shown in Figure 5.20. Note that the stresses are within the limit of 273 MPa.

Both the rod-cap outer edge and the extreme end of the cap corresponding to location 9 in Figure 3.5 have nearly $R = 0$ stress ratio. Since the maximum stress at the cap edge is 226 MPa, the equivalent stress amplitude at $R = -1$ is approximately 127 MPa. Similarly, the maximum stress at the extreme end of the cap is 248 MPa. So the equivalent stress amplitude at $R = -1$ is approximately 142 MPa. Both are within the limit of 204 MPa (Section 5.2.3).

5.5 OBSERVATIONS FROM THE OPTIMIZATION EXERCISE

1) The literature survey suggests that connecting rods are typically designed under static loads. It appears that different regions are designed separately with different static loads (i.e. such as in Sonsino and Esper, 1994). Doing so increases the number of steps in the design process. In contrast, a connecting rod could very well be designed under dynamic loads. Doing so would reduce the number of steps in the design process.

2) Though it is clear from Chapter 4 that the load at 360° crank angle is not necessarily the worst case loading, it can be concluded from the discussion in Sections 5.3 and 5.4 that a design with this load is clearly satisfactory.

The inertia load on the connecting rod is highest at 360° crank angle. However, depending on the particular pressure crank angle diagram the maximum load can occur at a different crank angle. In the case of the connecting rod considered, the peak load occurred at 362°

3) The applied load distribution at the crank end and at the piston pin end were based on experimental results (Webster *et al.*, 1983). They were also used in other studies in the literature by Folgar *et al.* (1987) and Athavale and Sajanpawar (1991). Since the details were not discussed by Webster *et al.*, the applicability of the loading to this connecting rod could not be evaluated.

4) With manual optimization under dynamic loading, at least 10% weight reduction could be achieved for the same fatigue performance as the existing connecting rod. This is in spite of the fact that C-70 steel has 18% lower yield strength and 20% lower endurance limit. Clearly, higher weight reduction may be achieved by automating the optimization and more accurate knowledge of load distributions at the connecting rod

ends. The axial stiffness is about the same as the existing connecting rod and the buckling load factor is higher than that for the existing connecting rod.

6) A component as shown in Figure 5.21 was also under development. However, punching out of the cavity in the shank would create distortion issues in the shank during the operation. From a steel forging point of view the connecting rod as shown in Figure 5.21 with a cavity in the shank is not recommended (correspondence with Mr. Tom Elmer from MAHLE Engine Components, Gananoque, ON, Canada).

7) C-70 has lower yield strength and endurance limit than the existing material. As a result it was essential to increase weight in the pin end region. New fracture cracking materials are being developed (such as micro-alloyed steels) with better properties (Repgen, 1998). Using these materials can help significantly reduce the weight of the connecting rod in the pin end and crank end cap. However in the shank region, manufacturing constraints such as minimum web and rib dimensions for forgeability of the connecting rod present restrictions to the extent of weight reduction that can be achieved.

8) Considering static strength, buckling load factor, and fatigue strength, it was found that the fatigue strength of the connecting rod is the most significant and the driving factor in the design and optimization of connecting rod.

5.6 MANUFACTURING ASPECTS

The connecting rod manufacturing processes for the conventional steel forging, powder forging, and fracture crackable steel forging are shown by charts in Figures 5.22, 5.23, and 5.24, respectively. A comparison between the processes can be made by

comparing the charts. The following steps in the manufacturing of the existing forged steel connecting rod can be eliminated by introducing C-70 crackable steel: the heat treatment, the machining of the mating faces of the crank end, and drilling for the sleeve. An entire block of machining steps after fracture splitting of C-70 is eliminated.

The fracture splitting process eliminates the need to separately forge the cap and the body of the connecting rod or the need to saw or machine a one-piece forged connecting rod into two. In addition, the two fracture split parts share a unique surface structure at the fractured surface that prevents the rod and the cap from relative movement (Reppen, 1998). This provides a firm contact and increases the stiffness in this region (Park *et al.*, 2003).

The fracture splitting is accomplished by making a notch in the connecting rod on diametrically opposite sides of the crank end bearing surface at the parting line of the rod and the cap. This notch may be generated by either laser notching, broaching or wire cutting. A cracking cylinder which runs through the crank end bore and which is hydraulically operated splits the connecting rod into two. The schematic is shown in Figure 5.25 (Park *et al.*, 2003).

The only manufacturing aspect taken into account during the optimization process was maintaining the forgeability of the connecting rod. While reducing the dimensions of the shank, the web and the rib dimensions were reduced to a certain limit. The web was retained in the shank for the same reason. Making a cut out in the shank would have resulted in more efficient utilization of the material, but the shape would not be forgeable without distortion as discussed in Section 5.5. Another aspect addressed to maintain the

forgeability is the draft angle provided on the connecting rod surface. The optimized geometry shown in Figure 5.12 includes a draft angle of 5° .

5.7 ECONOMIC COST ASPECTS

Paek *et al.* (1997), introduced a powder metal connecting rod, for their Hyundai Motor Co. Engine. They note that by adapting powder material for connecting rods, without loss of stiffness, they saved 10.5% on product cost in comparison with hot steel forged ConRods. The steel hot forged connecting rods they replaced required machining at the rod–cap joint face. In a paper published in 1998, Reppen with reference to forged steel connecting rods notes: “The development of the fracture splitting the connecting rods achieves a total cost reduction up to 25% compared to conventionally designed connecting rods and is widely accepted in Europe”. The result of these two studies indicate a cost advantage of 15% by switching from powder forged connecting rods to fracture cracking steel forged connecting rods. Reppen (1998) also makes a similar note: “In principle, a forged rough part can run on machining lines originally designed for powder metal connecting rods. An automotive manufacturer analyzed the costs and proved a cost reduction of 15%”.

Cost is a proprietary issue and is not easily available. There is a study published in 1989, which compared the cost of powder forged and steel forged connecting rods. The costs are as follows: combined conventional steel forged (single piece rod and cap as forged) fully machined cost is \$5.36 per connecting rod, the fully machined powder forged connecting rod costs \$5.04 per connecting rod. Table 5.5 shows a summary of the cost break down of forged steel and forged powder metal connecting rods (Clark *et al.*,

1989). Notice that machining steps of a forged steel connecting rod account for 62% of the total cost, whereas machining of a forged powder metal connecting rod accounts for 42% of the total cost. Connecting rods made of C-70 could have machining cost significantly less than 62% of the total cost. Elimination of heat treatment (correspondence with Mr. Tom Elmer from MAHLE Engine Components, Gananoque, ON, Canada) and lower material costs are other factors responsible for adding to the cost saving over the powder forged connecting rod.

Without considering the inflation, 25% cost reduction (Repgen, 1998) over the 1989 cost of the connecting rod means a saving of \$1.34 per connecting rod. With the current cost, the savings will be even more.

Costs of the individual processes are also indicated in Figures 5.22 through 5.24. The study by Clark *et al.* (1989) was used for obtaining these costs. Using the same study as a basis, the cost of connecting rod manufactured from C-70 was estimated. For a fracture splittable steel connecting rod, one can expect similar machining steps as for a powder forged connecting rod. As a result, it is a reasonable approximation to carry the machining costs from the powder forging process over to the C-70 forging process. Most of the other costs in the chart for C-70 have been carried over from the steel forging process. The cost of the fracture splitting process was not available. As a result, the cost of shearing the connecting rod and the cap was carried over.

During the optimization of the connecting rod, the material was changed from the existing forged steel to C-70 steel. In perspective of the above discussion, this change in material brings down the production cost of the optimized connecting rod by about 25%, in comparison to the cost of the existing connecting rod. It should be noted that the cost

has not been optimized, rather, it has been reduced. For example, consider the factors listed in Table 5.5. Among these factors it is clear that one important requirement to reduce machining cost is production of near net shape rough part, which could increase the forging, heating, and sizing costs. A mathematical model of the cost could be constructed taking into account all these conflicting factors. One could obtain a solution for minimum cost within these conflicting parameters. Taking such an approach of generating a mathematical model of various manufacturing parameters and costs was beyond the scope of this study.

Table 5.1: Summary of mechanical properties of existing forged steel and C-70 steel.

Monotonic Properties	Existing Forged Steel		C-70		% Change
Modulus of elasticity (assumed), E, GPa (ksi):	206.8	(29996)	211.5	30674	2.3
Yield strength (0.2% offset), YS, MPa (ksi):	700.0	(101.5)	573.7	(83.2)	-18
Ultimate strength, S _u , MPa (ksi):	937.7	(136.0)	965.8	(140.1)	2.9
True fracture strength, σ _f , MPa (ksi):	1266	(183.6)	1141	(165.5)	
Percent elongation, %EL (%):	24%		27%		
Percent reduction in area, %RA (%):	42%		25%		
Hardness, HRC:	28		23		
Cyclic Properties					
Fatigue strength coefficient, σ _f ['] , MPa (ksi):	1,187.9	(172.3)	1,302.6	(188.9)	
Fatigue strength exponent, b:	-0.0711		-0.0928		
Cyclic yield strength, YS', MPa (ksi)	619.8	(89.9)	527.6	(76.5)	-14.9
Endurance limit*, MPa (ksi)	423.4	(61.4)	338.9	(49.2)	-19.9

* Endurance limit computed (for N_f = 10⁶ cycles) using Basquin's equation: S_f = σ_f['] (2N_f)^b

Table 5.2: Input for quasi-dynamic FEA of the optimized connecting rod, using load analysis results at crankshaft speed of 5700 rev/min.

Crank Angle	Ang. Vel.	Ang. Acc.	Crank End Force				Piston Pin End Force				Pressure Constant for UDL -N/mm ²		Pressure Constant for Cosine Load-N/mm ²	
			Fx	Fy	Resultant	Direction	Fx	Fy	Resultant	Direction	Crank End	Piston Pin End	Crank End	Piston Pin End*
deg	rev/s	rev/s ²	N	N	N	deg	N	N	N	deg				
336	-30.1	-7205	-14255	667	14271	-2.7	7584	1396	7711	10.4	0.00	0.00	22.2	23.2
348	-32.0	-3603	-16078	240	16080	-0.9	8826	815	8863	5.3	0.00	0.00	25.0	26.6
360	-32.7	0	-16854	0	16854	0.0	9404	0	9404	0.0	0.00	0.00	26.2	28.3
362	-32.7	600	-16887	-32	16887	0.1	9443	-145	9444	-0.9	0.00	0.00	26.3	28.4
396	-27.0	10761	-12358	-1223	12418	5.6	6614	-1760	6844	-14.9	0.00	0.00	19.3	20.6

Acceleration at the crank end center is 17,280,197 mm/s².

Pressure constant for UDL is as defined by Equation 3.6

Pressure constant for cosine load is as defined by Equation 3.3.

* The pressure constants in this column have been corrected for the oil hole.

Table 5.3: Minimum factor of safety for regions I through V, shown in Figure 5.9.

Region on Con Rod	Minimum FS for the listed region with respect to S_y .		Minimum FS for the listed region with respect to S_u .	
	Existing Con Rod	New Con Rod -C-70	Existing Con Rod	New Con Rod -C-70
Tensile Load	Yield Strength/von Mises Stress (Tensile Load*)		Ultimate Strength/von Mises Stress (Tensile Load*)	
I	2.50	2.20	3.35	3.71
II	3.37	2.58	4.51	4.35
III	7.41	4.31	9.92	7.26
IV	2.75	2.25	3.69	3.78
V	1.42	1.42	1.90	2.39
Compressive Load	Yield Strength/von Mises Stress (Compressive Load*)		Ultimate Strength/von Mises Stress (Compressive Load*)	
I	20.00	16.10	26.79	27.11
II	2.33	2.19	3.12	3.68
III	4.13	2.36	5.54	3.97
IV	2.68	2.60	3.59	4.38
V	6.37	7.19	8.53	12.11
Cyclic Load	Endurance Limit/Equivalent Stress Amplitude			
I	2.39	2.09		
II	2.56	1.69		
III	3.34	1.91		
IV	1.72	1.81		
V	1.13	1.20		

* Loads as defined in Section 5.1.

Table 5.4: Comparison of the optimized connecting rod based on dynamic load analysis with the existing connecting rod.

	Optimized ConRod	Existing ConRod	% Change over existing
Material Properties	C-70	FS	
E (GPa)	211.5	206.7	2.3
Yield Strength (MPa)	574	700	-18
Percent Elongation, %EL (%):	27%	24%	12.5
Percent Reduction in Area, %RA (%):	25%	42%	-40.5
Ultimate Tensile Strength (MPa)	966	938	2.9
Endurance Limit (MPa)	339	423	-19.9
Other Factors			
Axial Displacement ¹ (mm)	0.204	0.206	0.9
Weight ² (gms)	396	440	-10.0
I _{zz} * (kg m ²)	0.00139	0.00144	-4.4
Buckling Load Factor	9.6	7.8	23

¹Obtained by measuring the overall displacements along the length of the connecting rod under the action of tensile load described in Section 5.1.

²Weight of the connecting rod does not include the weight of the bolt heads. Reported weight is the weight of the solid model generated for FEA. Since both weights are measured under similar conditions, the same weight savings can be expected in actual manufactured connecting rod.

*Mass moment of inertia of the connecting rod about the axis normal to the plane of motion and passing through the C.G. of the connecting rod.

Table 5.5: Cost split up of forged steel and forged powder metal connecting rods (Clark *et al.*, 1989).

Forged Steel		
Process	\$/part	Percent
Building	\$0.02	0.40%
Raw Material	\$0.84	15.60%
Heating	\$0.18	3.40%
Sizing	\$0.04	0.80%
Forging	\$0.45	8.30%
Trimming	\$0.13	2.40%
Coining	\$0.11	2.00%
Heat treating	\$0.10	1.80%
Shot Blast	\$0.04	0.80%
Shearing	\$0.04	0.80%
Inspection	\$0.09	1.60%
Machining	\$3.32	62%
Total	\$5.36	100.00%

Powder Metal		
Process	\$/part	Percent
Material	\$0.91	18.01%
Blending	\$0.08	1.57%
Compaction	\$0.51	10.07%
Sintering	\$0.37	7.33%
Forging	\$0.79	15.60%
Machining	\$2.12	42.01%
Building	\$0.12	2.33%
Sawing	\$0.07	1.40%
Inspection	\$0.08	1.67%
Total	\$5.04	100.00%

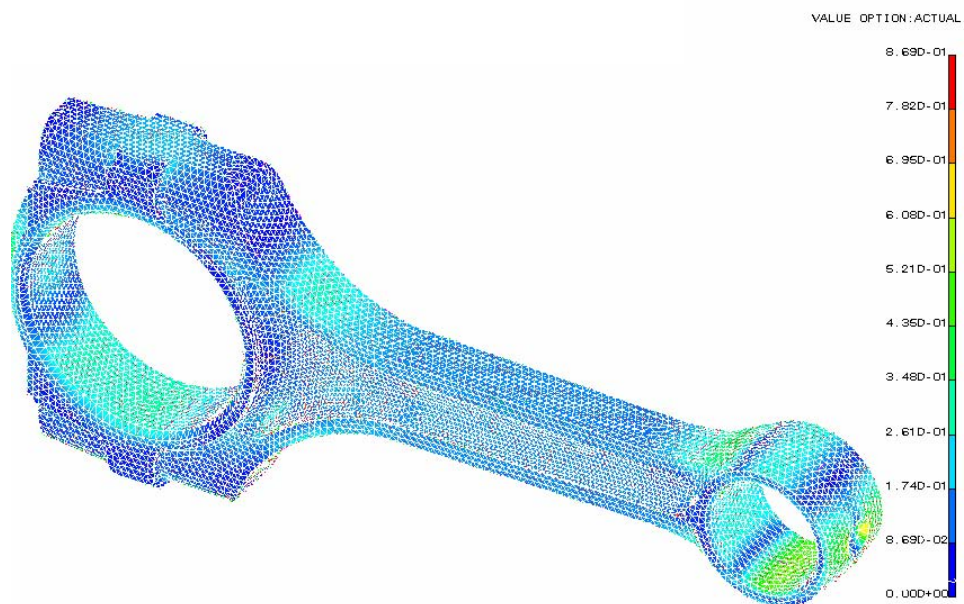


Figure 5.1: Failure Index (FI), defined as the ratio of von Mises stress to the yield strength of 700 MPa, under the dynamic tensile load at 360° crank angle for the existing connecting rod and material. Maximum FI is 0.696.

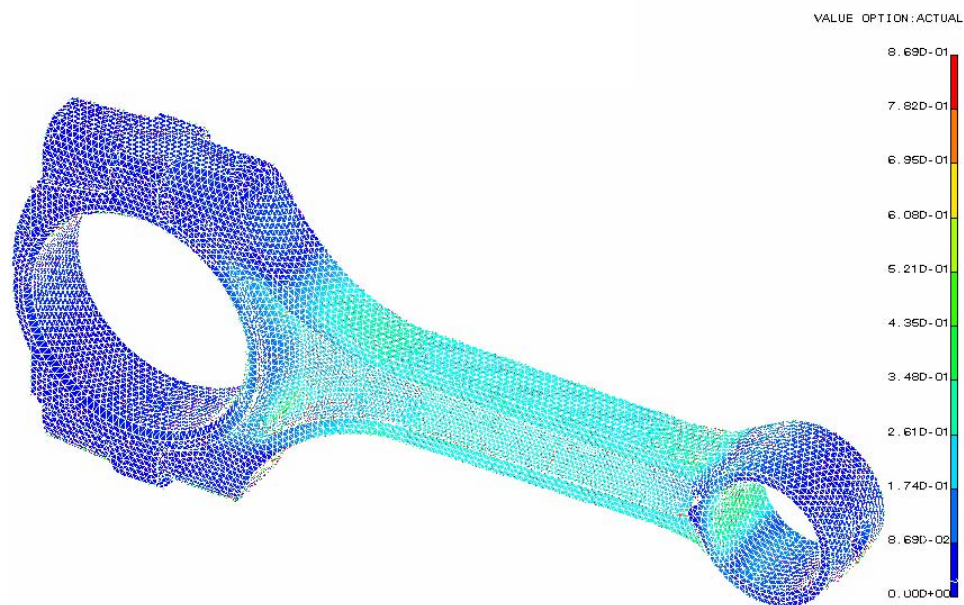


Figure 5.2: Failure Index (FI), defined as the ratio of von Mises stress to the yield strength of 700 MPa, under peak static compressive load for the existing connecting rod and material. Maximum FI is 0.395.

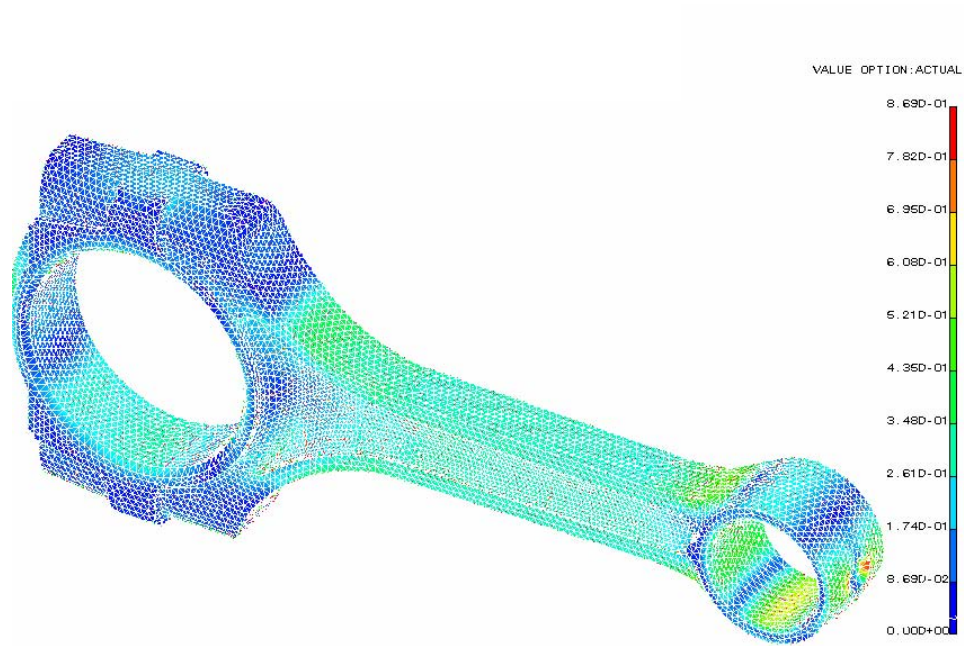


Figure 5.3: Failure Index (FI), defined as the ratio of equivalent stress amplitude at $R = -1$ to the endurance limit of 423 MPa, for the existing connecting rod and material. Maximum FI is 0.869.

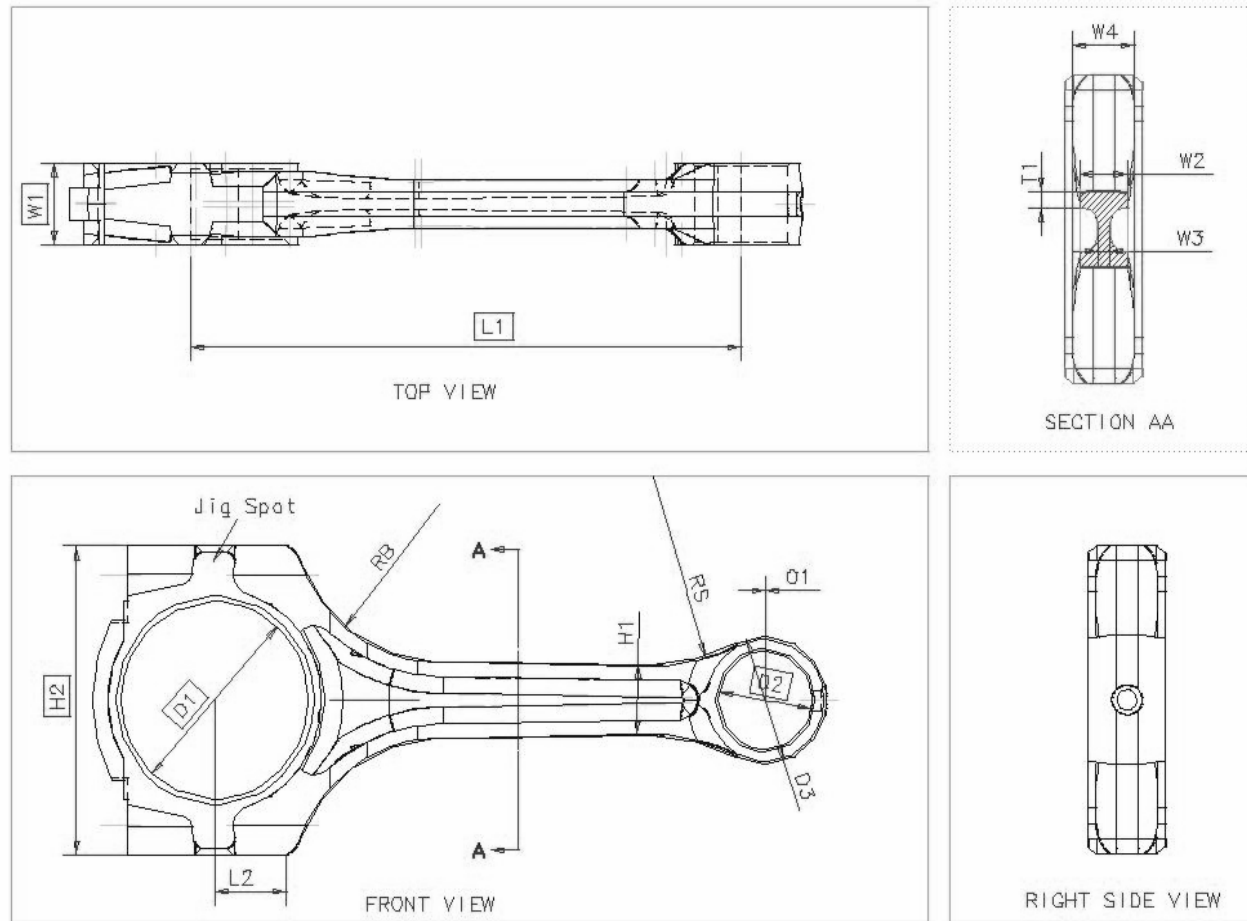


Figure 5.4: Drawing of the connecting rod showing few of the dimensions that are design variables and dimensions that cannot be changed. Dimensions that cannot be changed are boxed.

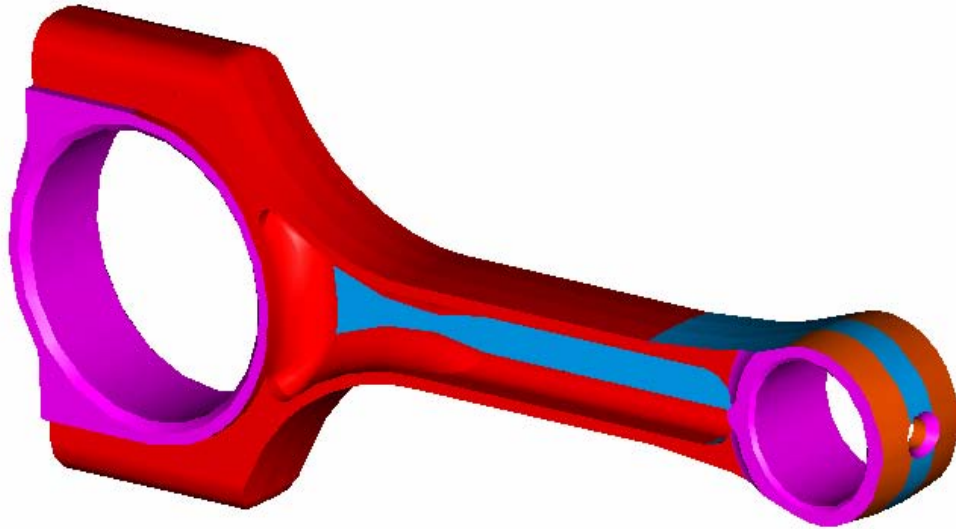


Figure 5.5: The geometry of the optimized connecting rod.

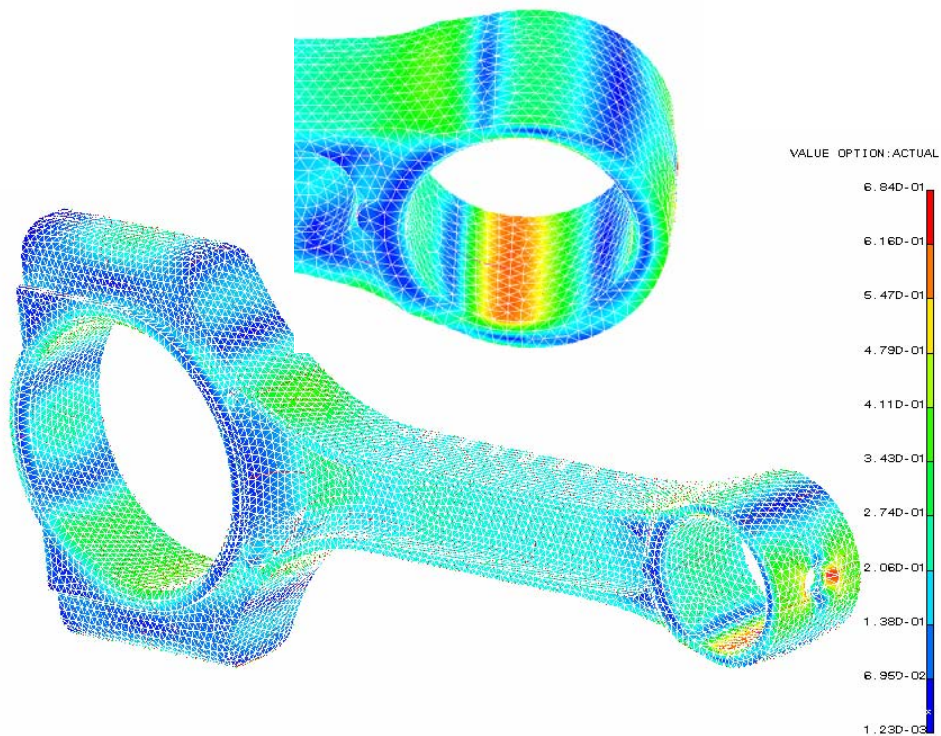


Figure 5.6: Failure Index (FI), defined as the ratio of von Mises stress to the yield strength of 574 MPa, under the dynamic tensile load occurring at 360° crank angle at 5700 rev/min for the optimized connecting rod. Maximum FI is 0.684.

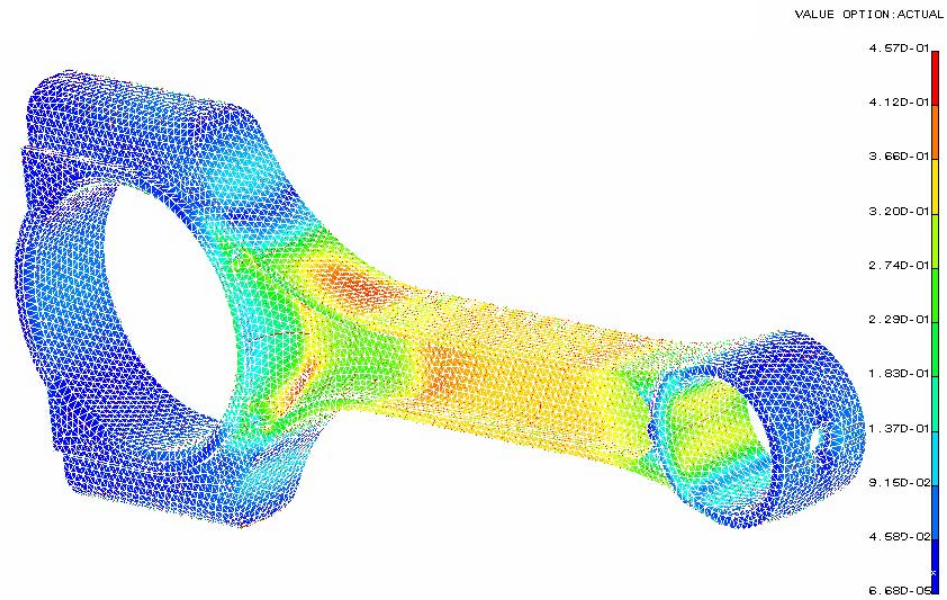


Figure 5.7: Failure Index (FI), defined as the ratio of von Mises stress to the yield strength of 574 MPa, under the peak compressive gas load for the optimized connecting rod. The maximum FI is 0.457.

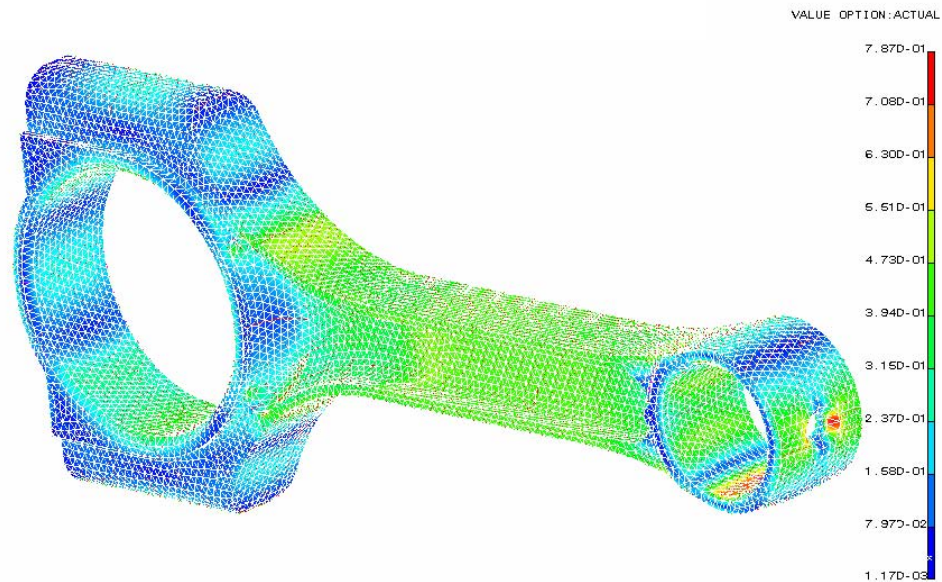


Figure 5.8: Failure Index (FI), defined as the ratio of equivalent stress amplitude at $R = -1$ to the endurance limit of 339 MPa for the optimized connecting rod. Maximum FI is 0.787.

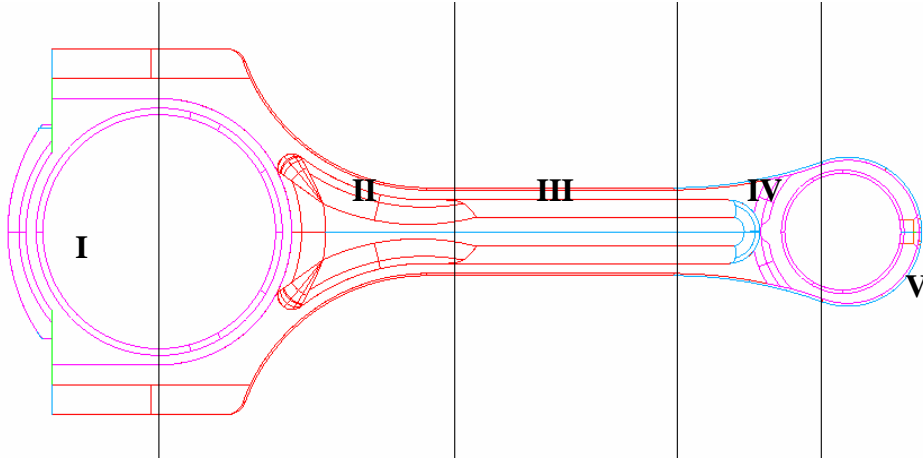


Figure 5.9: The various regions of the connecting rod that were analyzed for Failure Index (FI) or Factor of Safety (FS).

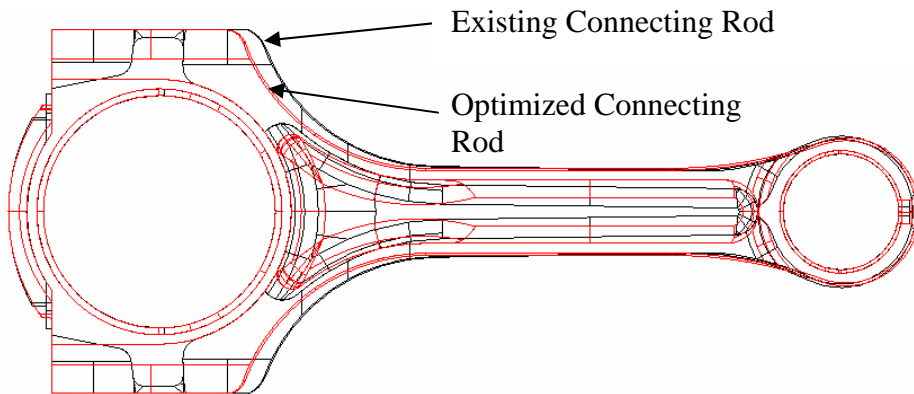


Figure 5.10: The existing and the optimized connecting rods superimposed.

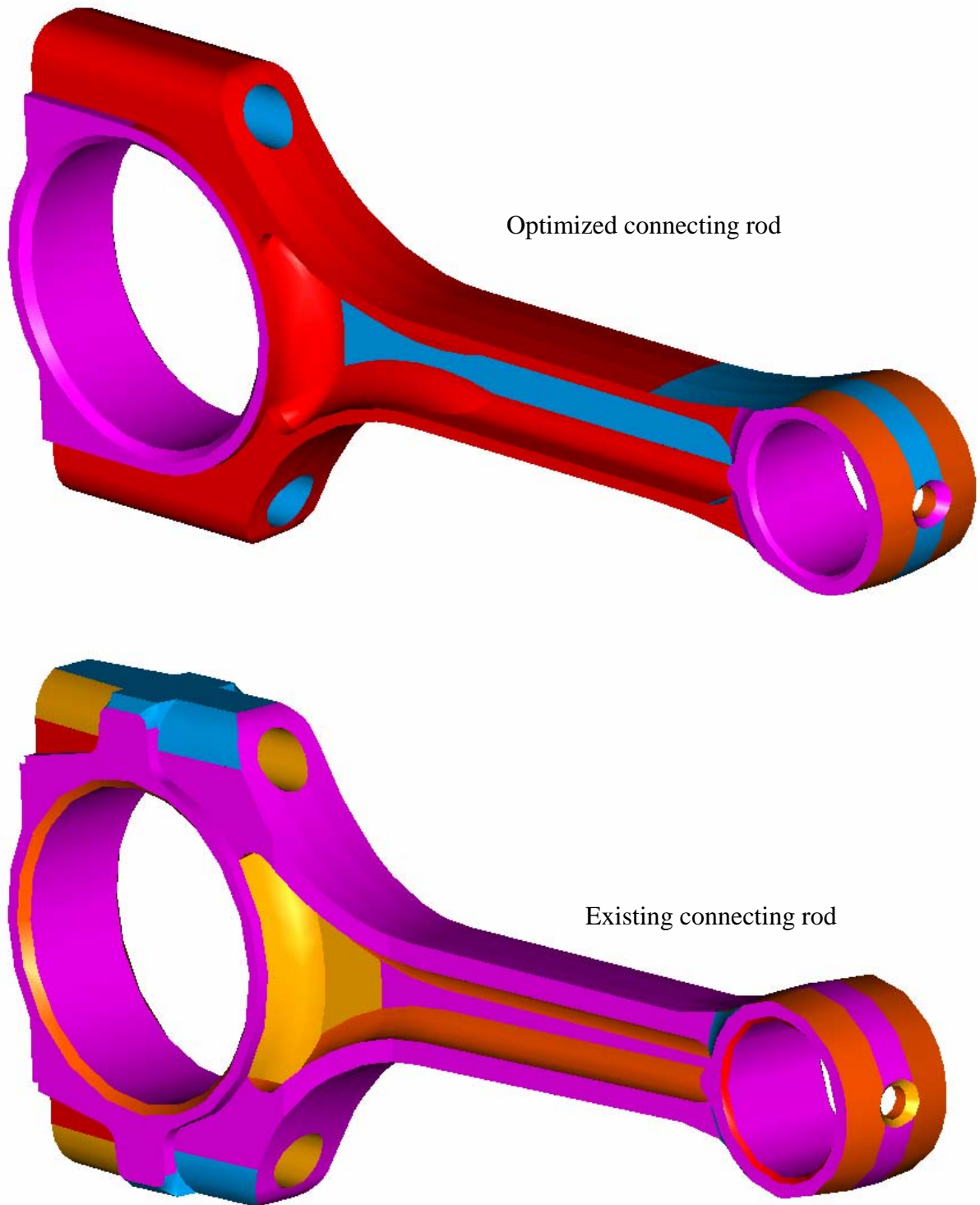


Figure 5.11: Isometric view of the optimized and existing connecting rod.

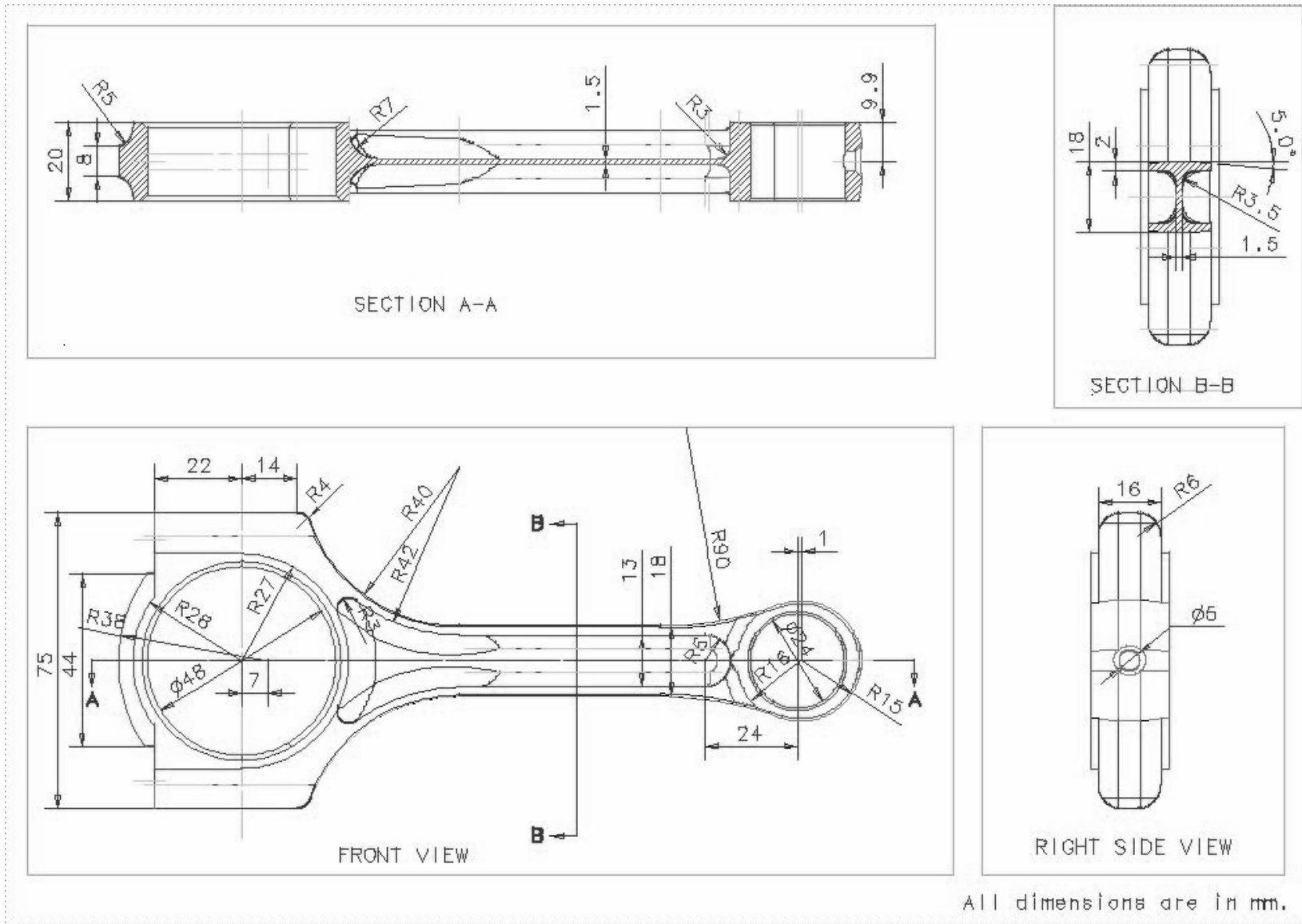


Figure 5.12: Drawing of the optimized connecting rod (bolt holes not included).

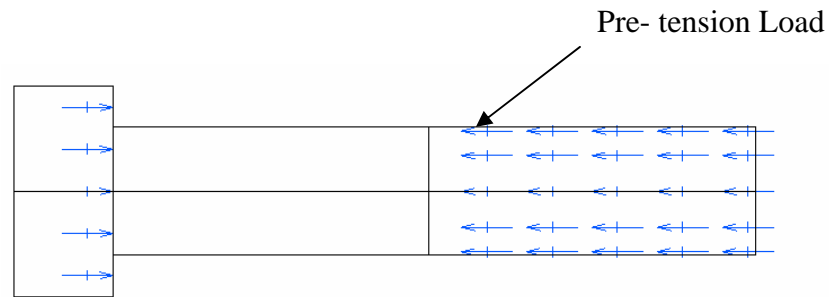


Figure 5.13: Modeling of the bolt pretension in the connecting rod assembly.

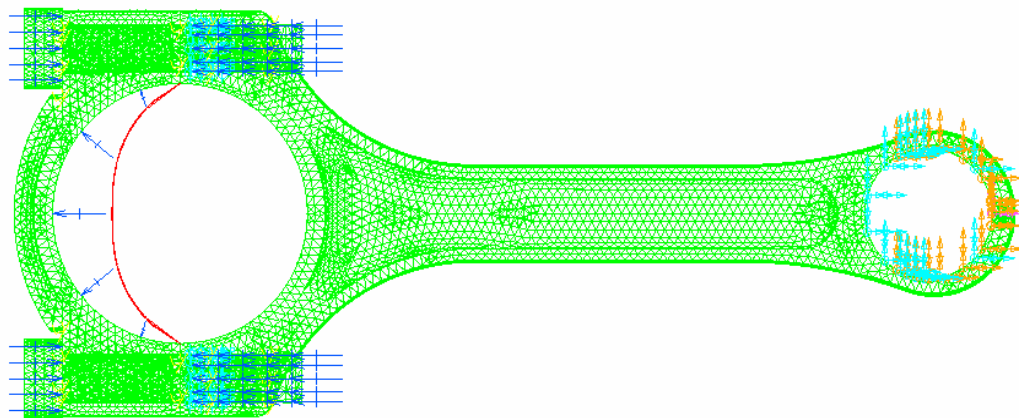


Figure 5.14: FE model of the connecting rod assembly consisting of the cap, rod, bolt and bolt pre-tension. The external load corresponds to the load at 360° crank angle at 5700 rev/min and was applied with cosine distribution. The pin end was totally restrained.

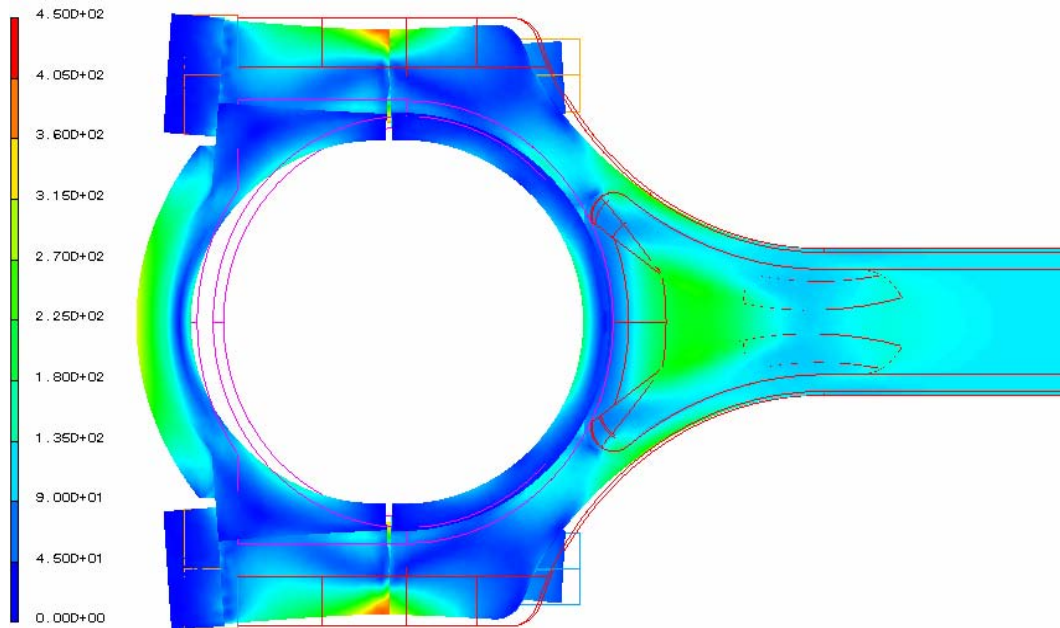


Figure 5.15: von Mises stress variation and displacements of the connecting rod and cap for a FEA model as shown in Figure 5.14 under tensile load described in Section 5.1. The displacement has been magnified 20 times.

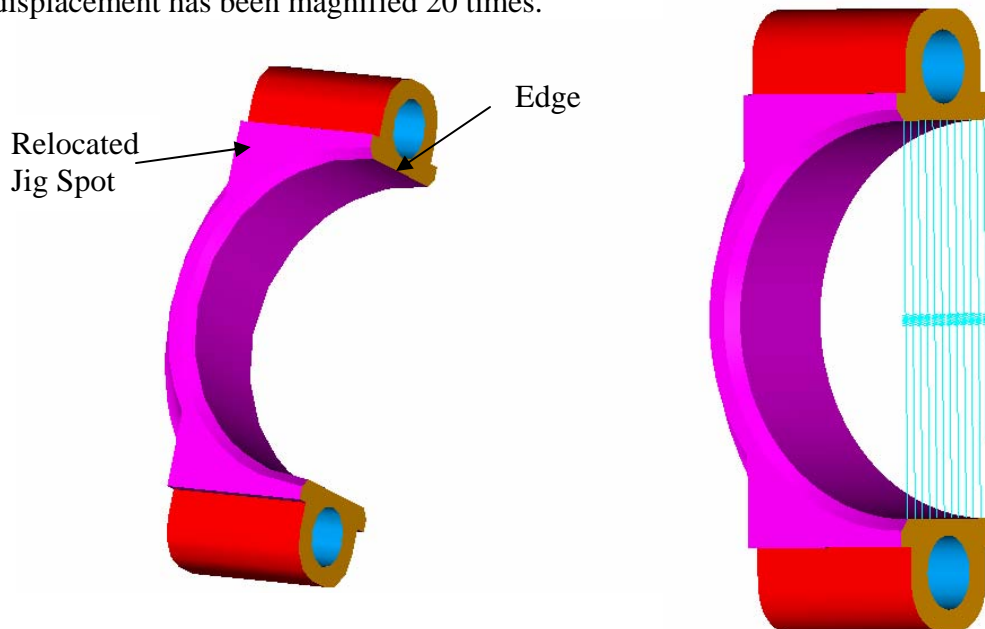


Figure 5.16: Connecting rod cap on the left shows the edge and the relocated jig spot. The figure of the cap on the right shows the springs connected between the opposite edges of the cap.

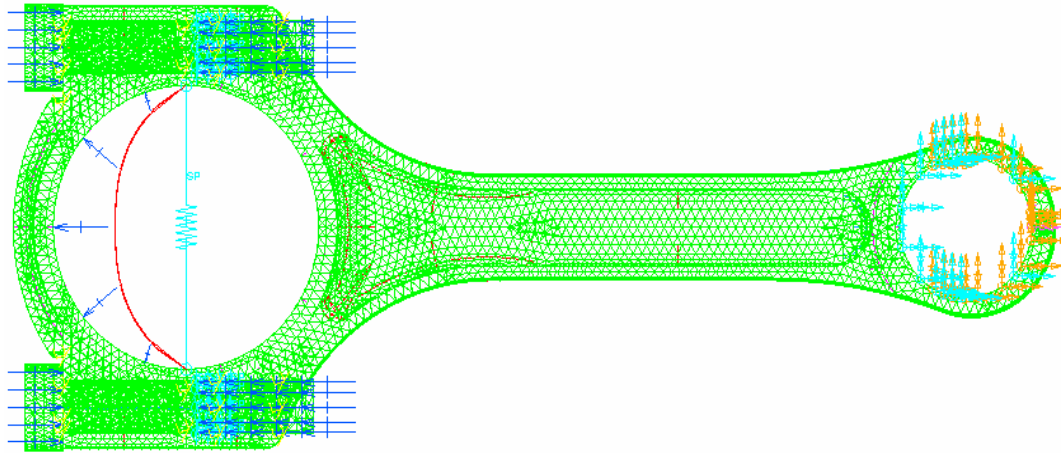


Figure 5.17: FE model of the connecting rod assembly consisting of the cap, rod, bolt and bolt pre-tension. The external load which corresponds to the load at 360° crank angle at 5700 rev/min was applied with cosine distribution. The pin end was totally restrained. Springs were introduced to model stiffness of other components (i.e. crankshaft, bearings, etc.).

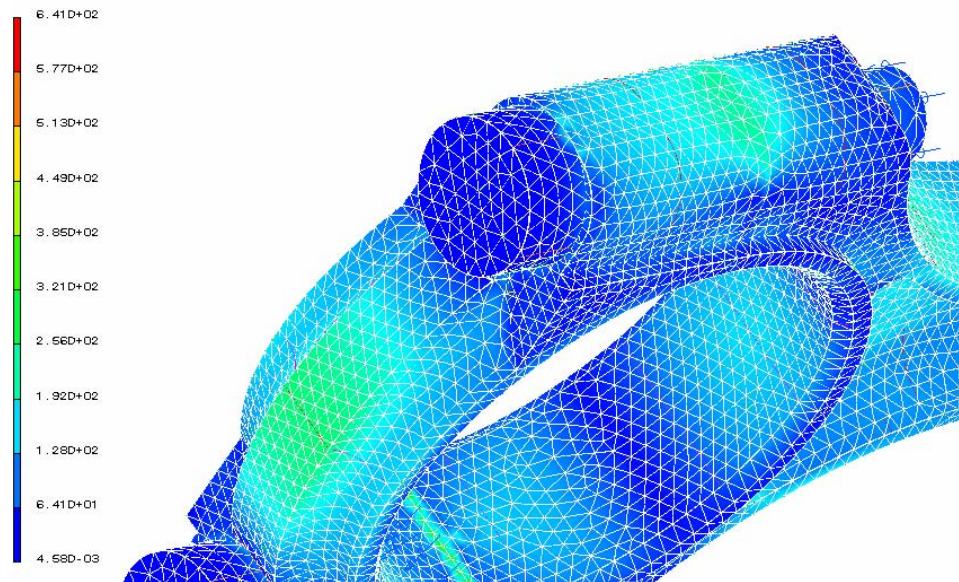


Figure 5.18: von Mises stress variation for FEM shown in Figure 5.17

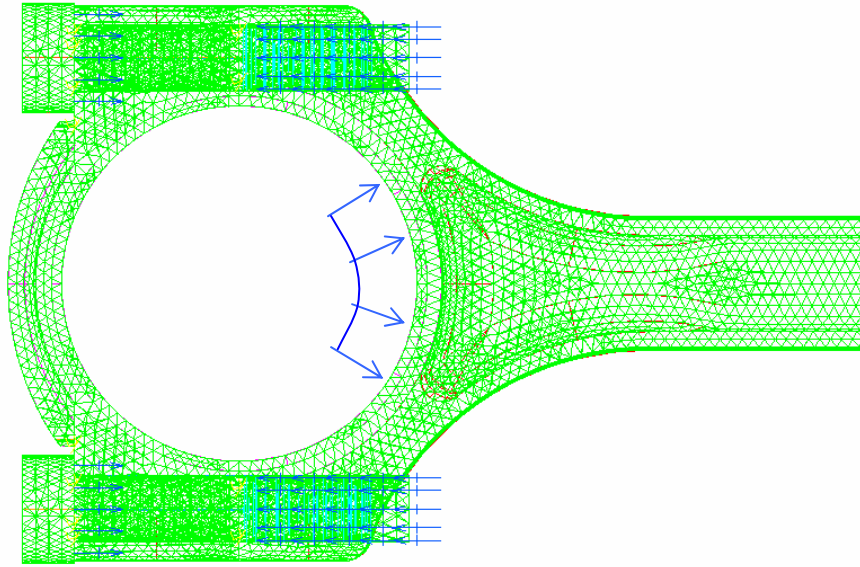


Figure 5.19: FE model of the connecting rod assembly consisting of the cap, rod, bolt and bolt pre-tension. The external load corresponds to the compressive load of 21.8 kN and was applied as a uniform distribution. The pin end was totally restrained.

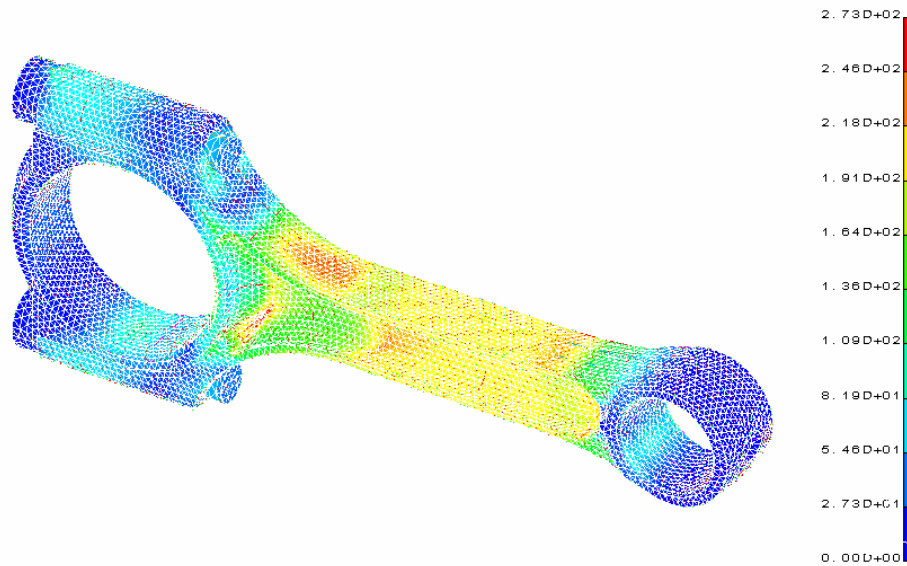


Figure 5.20: von Mises stress distribution under compressive load of 21.8 kN for the FEM shown in Figure 5.19.

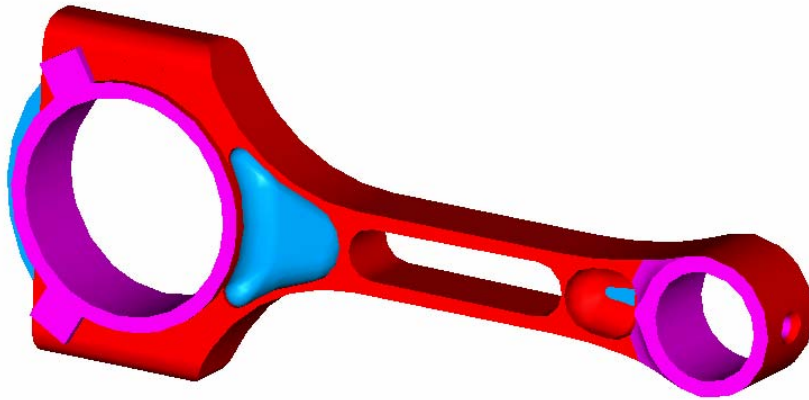


Figure 5.21: A trial connecting rod that was considered for optimization. Not a feasible solution since punching out of the hole in the shank would cause distortion.

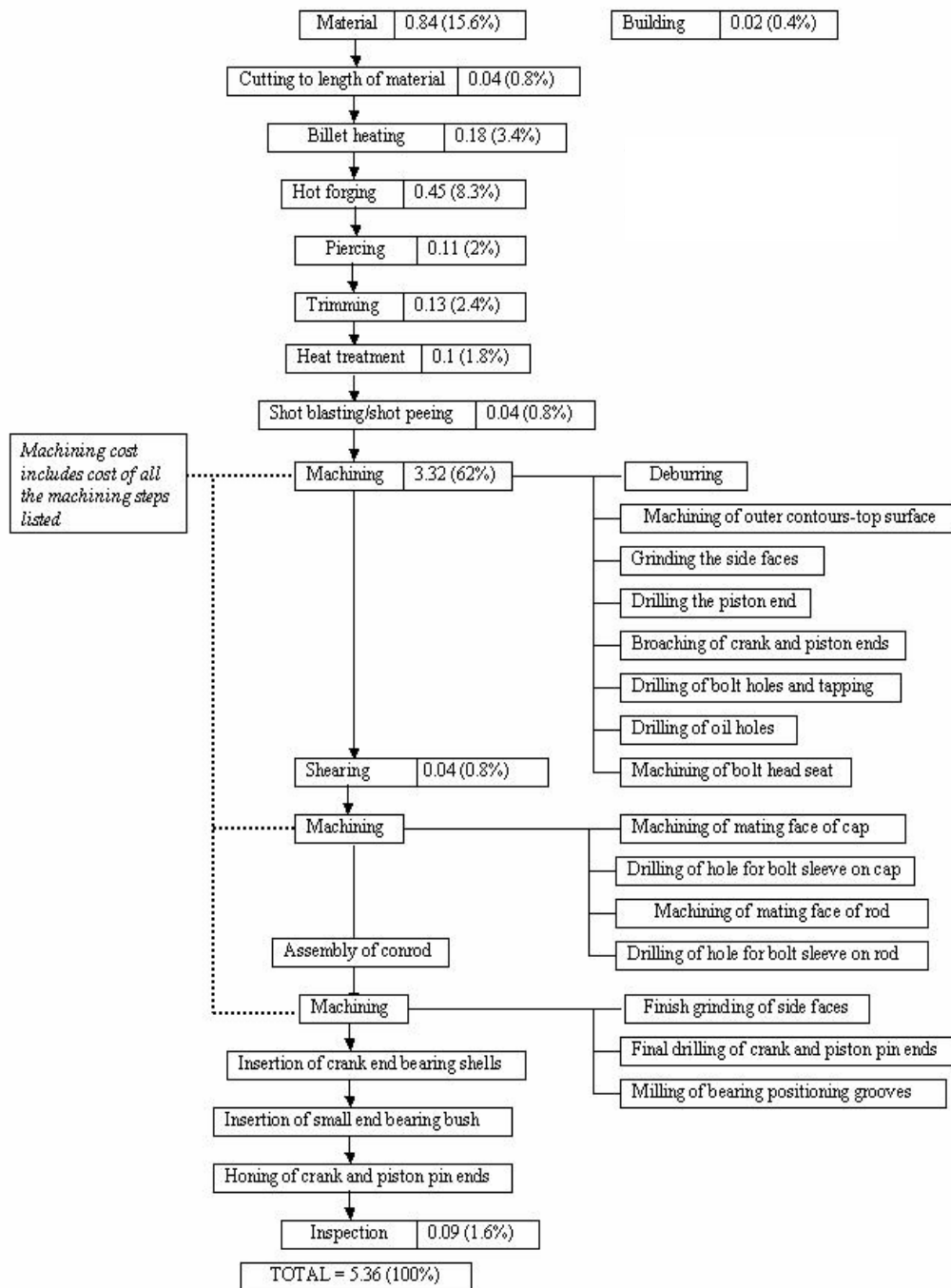


Figure 5.22: Steel forged connecting rod manufacturing process flow chart (correspondence with Mr. Tom Elmer from MAHLE Engine Components, Gananoque, ON, Canada). The number in each box is the cost in \$ and the number in the parentheses is the percent of the total cost.

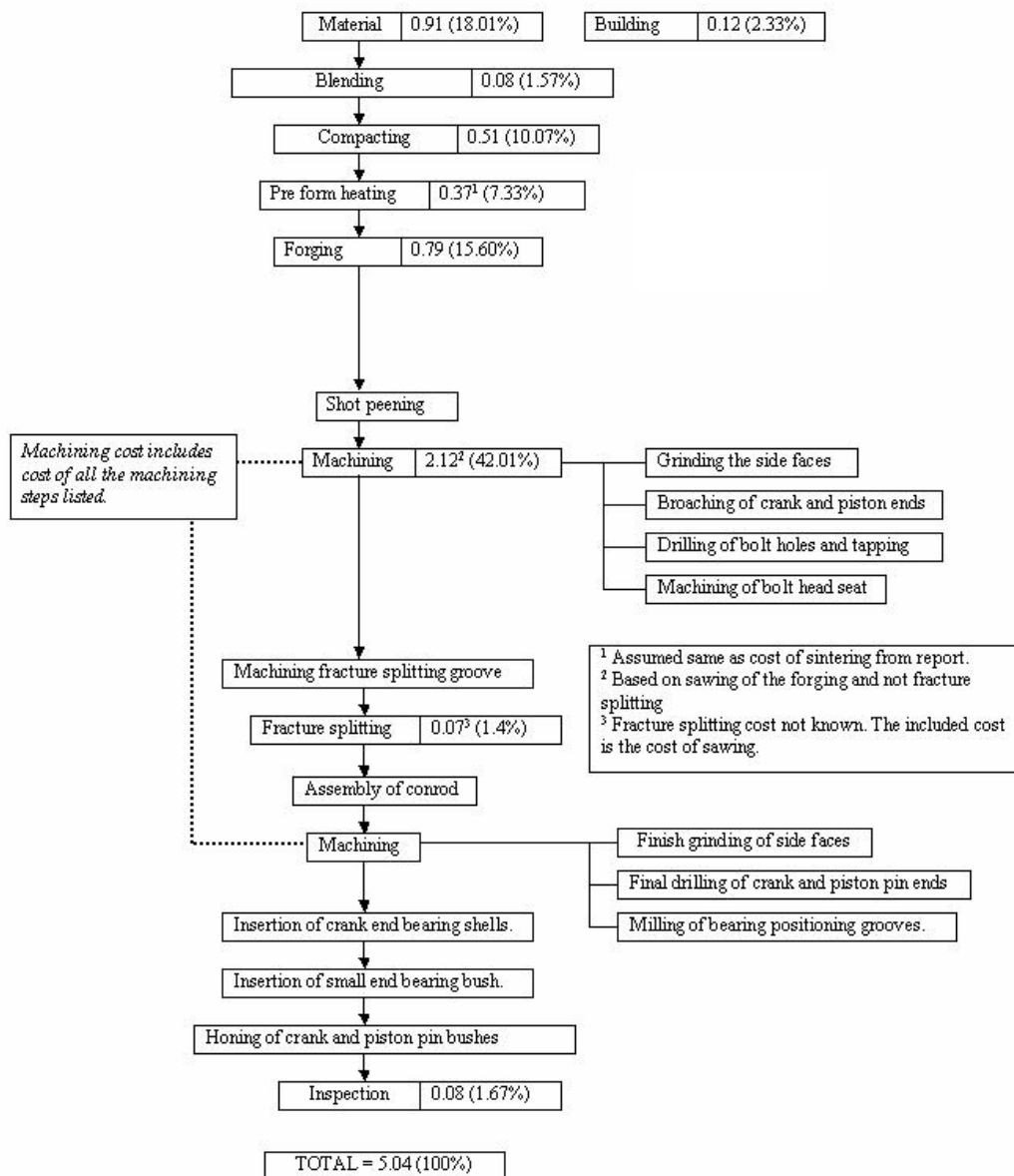


Figure 5.23: Powder forged connecting rod manufacturing process flow chart. The number in each box is the cost in \$ and the number in the parentheses is the percent of the total cost.

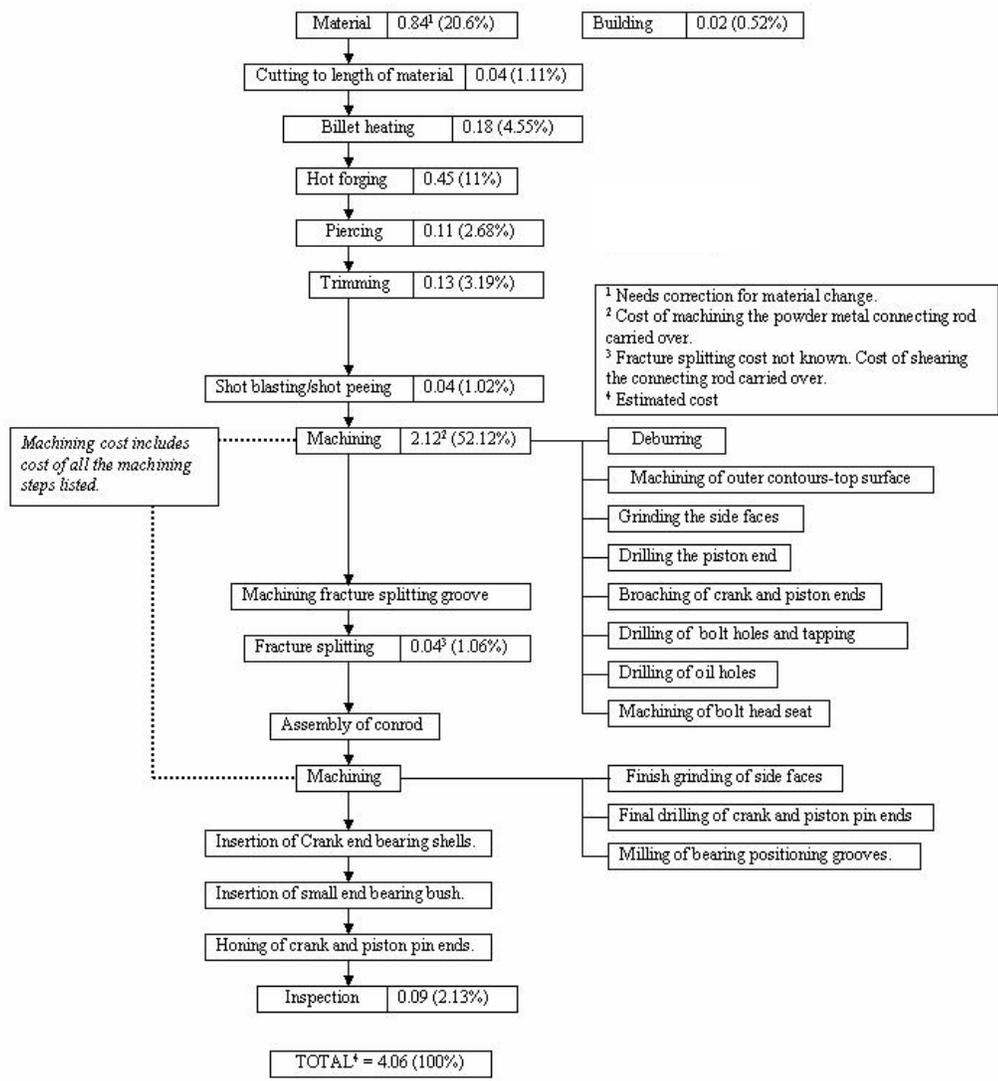


Figure 5.24: C-70 connecting rod manufacturing process flow chart (correspondence with Mr. Tom Elmer from MAHLE Engine Components, Gananoque, ON, Canada). The number in each box is the cost in \$ and the number in the parentheses is the percent of the total cost.

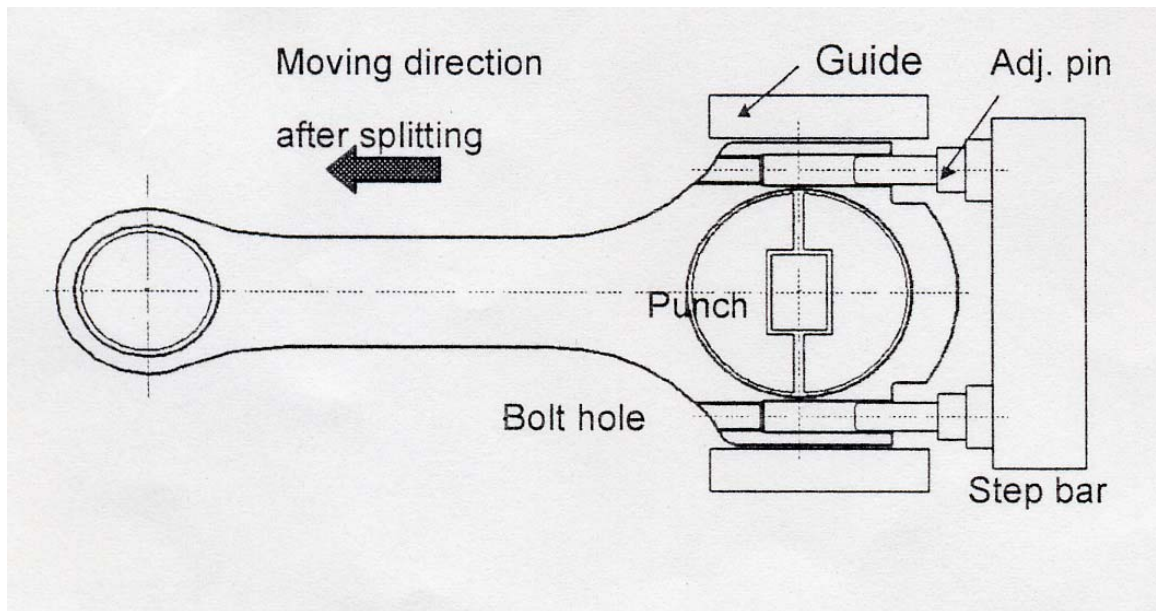


Figure 5.25: The fracture splitting process for steel forged connecting rod (Park *et al.*, 2003).

6. SUMMARY AND CONCLUSIONS

This research project investigated weight and cost reduction opportunities that steel forged connecting rods offer. The connecting rod chosen for this project belonged to a mid size sedan and was supplied by an OEM. First, the connecting rod was digitized. Load analysis was performed based on the input from OEM, which comprised of the crank radius, piston diameter, the piston assembly mass, and the pressure-crank angle diagram, using analytical techniques and computer-based mechanism simulation tools (I-DEAS and ADAMS). Quasi-dynamic FEA was then performed using the results from load analysis to gain insight on the structural behavior of the connecting rod and to determine the design loads for optimization. The following conclusions can be drawn from this study:

- 1) There is considerable difference in the structural behavior of the connecting rod between axial fatigue loading and dynamic loading (service operating condition). There are also differences in the analytical results obtained from fatigue loading simulated by applying loads directly to the connecting rod and from fatigue loading with the pins and interferences modeled.

- 2) Dynamic load should be incorporated directly during design and optimization as the design loads, rather than using static loads. The load range comprising of the peak gas load and the load corresponding to 360° crank angle at 5700 rev/min (maximum

engine speed) can be used for design and optimization (subject to verification for the particular engine), as the design loads.

3) Bending stresses were significant and should be accounted for. Tensile bending stresses were about 16% of the stress amplitude (entire operating range) at the start of crank end transition and about 19% of the stress amplitude (entire operating range) at the shank center. Bending stresses were negligible at the piston pin end. The R ratio (i.e. minimum to maximum stress ratio) varies with location on the connecting rod and with speed of the crankshaft. The stress ratio varies from -0.14 at the extreme end of the connecting rod cap to -1.95 at the crank end transition, under service operating conditions considering the entire load range. In the middle of the shank the R ratio varies from -18.8 at 2000 rev/min to -0.86 at 5700 rev/min.

4) The stress multiaxiality is high (the transverse component is 30% of the axial component), especially at the critical region of the crank end transition. Therefore, multiaxial fatigue analysis is needed to determine fatigue strength. Due to proportional loading, equivalent stress approach based on von Mises criterion can be used to compute the equivalent stress amplitude.

Optimization was performed to reduce weight and manufacturing cost. Cost was reduced by changing the material of the current forged steel connecting rod to crackable forged steel (C-70). While reducing the weight, the static strength, fatigue strength, and the buckling load factor were taken into account. The following conclusions can be drawn from the optimization part of the study:

1) Fatigue strength was the most significant factor (design driving factor) in the optimization of this connecting rod.

2) The connecting rod was optimized under a load range comprising the dynamic load at 360° crank angle at maximum engine speed and the maximum gas load. This connecting rod satisfied all the constraints defined and was found to be satisfactory at other crank angles also.

3) At locations like the cap-rod outer edge, the extreme end of the cap, and the surface of the piston pin end bore, the stresses were observed to be significantly lower under conditions of assembly (with bearings, crankshaft and piston pin and bushing), when compared to stresses predicted by cosine loading (tensile load).

4) The optimized geometry is 10% lighter and cost analysis indicated it would be 25% less expensive than the current connecting rod, in spite of lower strength of C-70 steel compared to the existing forged steel. PM connecting rods can be replaced by fracture splittable steel forged connecting rods with an expected cost reduction of about 15% or higher, with similar or better fatigue behaviour.

5) By using other fracture crackable materials such as micro-alloyed steels having higher yield strength and endurance limit, the weight at the piston pin end and the crank end can be further reduced. Weight reduction in the shank region is, however, limited by manufacturing constraints.

REFERENCES

- Afzal, A., 2004, "Fatigue Behavior and Life prediction of Forged Steel and PM Connecting Rods," Master's Thesis, University of Toledo.
- Athavale, S. and Sajanpawar, P. R., 1991, "Studies on Some Modelling Aspects in the Finite Element Analysis of Small Gasoline Engine Components," *Small Engine Technology Conference Proceedings*, Society of Automotive Engineers of Japan, Tokyo, pp. 379-389.
- Balasubramaniam, B., Svoboda, M., and Bauer, W., 1991, "Structural optimization of I.C. engines subjected to mechanical and thermal loads," *Computer Methods in Applied Mechanics and Engineering*, Vol. 89, pp. 337-360.
- Bhandari, V. B., 1994, "*Design of Machine Elements*," Tata McGraw-Hill.
- Clark, J. P., Field III, F. R., and Nallicheri, N. V., 1989, "Engine state-of-the-art a competitive assessment of steel, cost estimates and performance analysis," *Research Report BR 89-1*, Automotive Applications Committee, American Iron and Steel Institute.
- El-Sayed, M. E. M., and Lund, E. H., 1990, "Structural optimization with fatigue life constraints," *Engineering Fracture Mechanics*, Vol. 37, No. 6, pp. 1149-1156.
- Folgar, F., Wldrig, J. E., and Hunt, J. W., 1987, "Design, Fabrication and Performance of Fiber FP/Metal Matrix Composite Connecting Rods," *SAE Technical Paper Series 1987*, Paper No. 870406.
- Ferguson, C. R., 1986, "*Internal Combustion Engines, Applied Thermosciences*," John Wiley and Sons, Inc.
- Goenka, P. K. and Oh, K. P., 1986, "An Optimum Connecting Rod Design Study – A Lubrication Viewpoint," *Journal of Tribology*, Transactions of ASME, July 1986, Vol. 108.
- Gupta, R. K., 1993, "Recent Developments in Materials and Processes for Automotive Connecting rods," *SAE Technical Paper Series*, Paper No. 930491.
- Hippoliti, R., 1993, "FEM method for design and optimization of connecting rods for small two-stroke engines," *Small Engine Technology Conference*, pp. 217-231.

Ishida, S., Hori, Y., Kinoshita, T., and Iwamoto, T., 1995, "Development of technique to measure stress on connecting rod during firing operation," *SAE 951797*, pp. 1851-1856.

Ludenbach, B., 2002, "Manufacturing Processes and Characteristics of Forged Steel and Forged Powder Metal Connecting Rods," *24th Forging Industry Technical Conference Proceedings*, Forging Industry Association, October 14-16, Cleveland, OH.

Makino, T. and Koga, T., Feb 2002, "Crank Bearing Design Based on 3-D Elasto-hydrodynamic Lubrication Theory," *Mitsubishi Heavy Industries, Ltd., Technical Review*, Vol. 39, No. 1.

Norton R. L., 1996, "*Machine Design-An Integrated Approach*," Prentice-Hall.

Paek, S. Y., Ryou, H. S., Oh, J. S., and Choo, K. M., 1997, "Application of high performance powder metal connecting rod in V6 engine," *SAE Technical Paper Series*, Paper No. 970427.

Pai, C. L., 1996, "The shape optimization of a connecting rod with fatigue life constraint," *Int. J. of Materials and Product Technology*, Vol. 11, No. 5-6, pp. 357-370.

Park, H., Ko, Y. S., Jung, S. C., Song, B. T., Jun, Y. H., Lee, B. C., and Lim, J. D., 2003, "Development of Fracture Split Steel Connecting Rods," *SAE Technical Paper Series*, Paper No. 2003-01-1309.

Rabb, R., 1996, "Fatigue failure of a connecting rod," *Engineering Failure Analysis*, Vol. 3, No. 1, pp. 13-28.

Reppen, B., 1998, "Optimized Connecting Rods to Enable Higher Engine Performance and Cost Reduction," *SAE Technical Paper Series*, Paper No. 980882.

Rice, R. C., ed., "*SAE Fatigue Design Handbook*", 3rd Edition, Society of Automotive Engineers, Warrendale, PA, 1997.

Sarihan, V. and Song, J., 1990, "Optimization of the Wrist Pin End of an Automobile Engine Connecting Rod With an Interference Fit," *Journal of Mechanical Design*, Transactions of the ASME, Vol. 112, pp. 406-412.

Serag, S., Sevien, L., Sheha, G., and El-Beshtawi, I., 1989, "Optimal design of the connecting-rod", *Modelling, Simulation and Control, B, AMSE Press*, Vol. 24, No. 3, pp. 49-63.

Shigley, J. E. and Mischke, C. R., 1989, "*Mechanical Engineering Design*," 5th Edition, McGraw-Hill, Inc.

Socie, D. F. and Marquis, G. B., 2000, "*Multiaxial Fatigue*", Society of Automotive Engineers, Warrendale, PA.

Sonsino, C. M., and Esper, F. J., 1994, “*Fatigue Design for PM Components*,” European Powder Metallurgy Association (EPMA).

Stephens, R. I., Fatemi, A., Stephens, R. R., and Fuchs, H. O., 2000, “*Metal Fatigue in Engineering*,” 2nd Edition, John Wiley and Sons, Inc.

Webster, W. D., Coffell R., and Alfaro D., 1983, “A Three Dimensional Finite Element Analysis of a High Speed Diesel Engine Connecting Rod,” *SAE Technical Paper Series*, Paper No. 831322.

Wilson, C. E. and Sadler, P. J., 1993, “*Kinematics and Dynamics of Machinery*,” 2nd Edition, HarperCollins College Publishers.

Yoo, Y. M., Haug, E. J., and Choi, K. K., 1984, “Shape optimal design of an engine connecting rod,” *Journal of Mechanisms, Transmissions, and Automation in Design*, Transactions of ASME, Vol. 106, pp. 415-419.

APPENDIX I

Analytical Vector Approach To Kinematic And Dynamic Analysis Of The Connecting Rod.

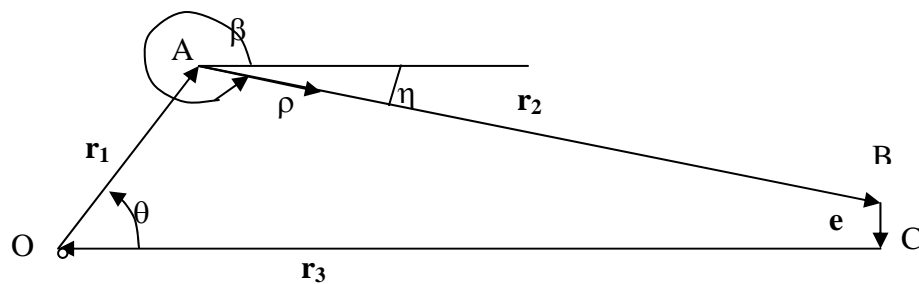


Figure I.1: Vector representation of slider crank mechanism.

The following quantities will be required for performing FEA to simulate dynamic conditions using I-DEAS: angular velocity, angular acceleration, loads at the ends, and linear acceleration of crank end center. Determination of the loads at the ends requires determination of the inertia load at the center of gravity of the connecting rod and the inertia load due to piston assembly.

A) Angular velocity of the connecting rod:

Consider the offset slider crank linkage shown in Figure I.1. The linkage can be described by the following vector equation:

$$\mathbf{e} + \mathbf{r}_1 + \mathbf{r}_2 + \mathbf{r}_3 = 0 \quad (1)$$

where, \mathbf{e} is constant in magnitude and direction. The bold letters represent vector quantities. Differentiating Equation 1 w.r.t. time:

$$\dot{e} + \dot{r}_1 + \dot{r}_2 + \dot{r}_3 = 0 \quad (2)$$

$$\boldsymbol{\omega}_1 \times \mathbf{r}_1 + \boldsymbol{\omega}_2 \times \mathbf{r}_2 - \mathbf{V}_p = \mathbf{0}. \quad (3)$$

where, $dr_3 / dt = -V_p$ and t stands for time.

Slider velocity V_p is in x direction and angular velocity vectors are in the z direction. To eliminate V_p in Equation 3, take the dot product of each term with \mathbf{j} :

$$\boldsymbol{\omega}_1 \times \mathbf{r}_1 \cdot \mathbf{j} + \boldsymbol{\omega}_2 \times \mathbf{r}_2 \cdot \mathbf{j} - \mathbf{V}_p \cdot \mathbf{j} = 0.$$

$$\omega_1 \mathbf{r}_1 \cdot \mathbf{i} + \omega_2 \mathbf{r}_2 \cdot \mathbf{i} = 0$$

$$\omega_2 = -\omega_1 (\mathbf{r}_1 \cdot \mathbf{i}) / (\mathbf{r}_2 \cdot \mathbf{i}) \quad (4)$$

From Figure I.1, the following equations can be written:

$$\mathbf{r}_1 = r_1 \cos\theta \mathbf{i} + r_1 \sin\theta \mathbf{j} \quad (5)$$

$$\mathbf{r}_2 = r_2 \cos\beta \mathbf{i} + r_2 \sin\beta \mathbf{j} \quad (6)$$

Substituting Equations 5 and 6 into Equation 4 gives the magnitude of $\boldsymbol{\omega}_2$, the **angular velocity of the connecting rod**:

$$\omega_2 = -(\omega_1 r_1 \cos\theta) / (r_2 \cos\beta) \quad (7)$$

For the case where the offset $e = 0$, from Figure I.1:

$$r_1 \sin\theta = r_2 \sin\eta = r_2 \sin(2\pi - \beta) = -r_2 \sin\beta$$

$$\sin\beta = -(r_1 \sin\theta) / r_2$$

$$\cos\beta = r_1 / r_2 * [(r_2 / r_1)^2 - \sin^2\theta]^{0.5} \quad (9)$$

Equation 7 becomes:

$$\omega_2 = -\omega_1 \cos\theta / [(r_2 / r_1)^2 - \sin^2\theta]^{0.5} \quad \text{where, } \boldsymbol{\omega}_2 = \omega_2 \mathbf{k} \quad (10)$$

B) Angular acceleration of the connecting rod:

To obtain the angular acceleration, consider Equation 3. Differentiating the equation w.r.t. time, for constant angular velocity of the crank, we get:

$$\boldsymbol{\omega}_1 \times \boldsymbol{\omega}_1 \times \mathbf{r}_1 + \boldsymbol{\omega}_2 \times \boldsymbol{\omega}_2 \times \mathbf{r}_2 + \mathbf{a}_p \times \mathbf{r}_2 - \mathbf{a}_p = \mathbf{0} \quad (11)$$

Since the acceleration of the slider is in the x direction, the last term in the above equation may be eliminated by taking the dot product of each term with the unit vector \mathbf{j} .

The result is:

$$\begin{aligned} \boldsymbol{\omega}_1 \times \boldsymbol{\omega}_1 \times \mathbf{r}_1 \cdot \mathbf{j} + \boldsymbol{\omega}_2 \times \boldsymbol{\omega}_2 \times \mathbf{r}_2 \cdot \mathbf{j} + \mathbf{a}_p \times \mathbf{r}_2 \cdot \mathbf{j} &= \mathbf{0} \\ \mathbf{a}_p &= (-\boldsymbol{\omega}_1 \times \boldsymbol{\omega}_1 \times \mathbf{r}_1 \cdot \mathbf{j} - \boldsymbol{\omega}_2 \times \boldsymbol{\omega}_2 \times \mathbf{r}_2 \cdot \mathbf{j}) / (\mathbf{k} \times \mathbf{r}_2 \cdot \mathbf{j}) \end{aligned} \quad (12)$$

Evaluating each term:

$$\boldsymbol{\omega}_1 \times \mathbf{r}_1 = \omega_1 \mathbf{k} \times [r_1 \cos\theta \mathbf{i} + r_1 \sin\theta \mathbf{j}] = \omega_1 r_1 \cos\theta (\mathbf{k} \times \mathbf{i}) + \omega_1 r_1 \sin\theta (\mathbf{k} \times \mathbf{j})$$

$$= \omega_1 r_1 \cos\theta (\mathbf{j}) + \omega_1 r_1 \sin\theta (-\mathbf{i}) = \omega_1 r_1 \cos\theta \mathbf{j} - \omega_1 r_1 \sin\theta \mathbf{i}$$

$$\boldsymbol{\omega}_1 \times \boldsymbol{\omega}_1 \times \mathbf{r}_1 = \omega_1 \mathbf{k} \times [\omega_1 r_1 \cos\theta \mathbf{j} - \omega_1 r_1 \sin\theta \mathbf{i}] = -\omega_1^2 r_1 \cos\theta \mathbf{i} - \omega_1^2 r_1 \sin\theta \mathbf{j} \quad (13)$$

$$-\boldsymbol{\omega}_1 \times \boldsymbol{\omega}_1 \times \mathbf{r}_1 \cdot \mathbf{j} = \omega_1^2 r_1 \cos\theta \mathbf{i} \cdot \mathbf{j} + \omega_1^2 r_1 \sin\theta \mathbf{j} \cdot \mathbf{j} = \omega_1^2 r_1 \sin\theta \quad (14)$$

$$\boldsymbol{\omega}_2 \times \mathbf{r}_2 = \omega_2 \mathbf{k} \times [r_2 \cos\beta \mathbf{i} + r_2 \sin\beta \mathbf{j}] = \omega_2 r_2 \cos\beta (\mathbf{k} \times \mathbf{i}) + \omega_2 r_2 \sin\beta (\mathbf{k} \times \mathbf{j})$$

$$= \omega_2 r_2 \cos\beta \mathbf{j} - \omega_2 r_2 \sin\beta \mathbf{i}$$

$$\boldsymbol{\omega}_2 \times \boldsymbol{\omega}_2 \times \mathbf{r}_2 = \omega_2 \mathbf{k} \times [\omega_2 r_2 \cos\beta \mathbf{j} - \omega_2 r_2 \sin\beta \mathbf{i}] = \omega_2^2 r_2 \cos\beta (\mathbf{k} \times \mathbf{j}) - \omega_2^2 r_2 \sin\beta (\mathbf{k} \times \mathbf{i})$$

$$= -\omega_2^2 r_2 \cos\beta \mathbf{i} - \omega_2^2 r_2 \sin\beta \mathbf{j} \quad (15)$$

$$-\boldsymbol{\omega}_2 \times \boldsymbol{\omega}_2 \times \mathbf{r}_2 \cdot \mathbf{j} = \omega_2^2 r_2 \cos\beta \mathbf{i} \cdot \mathbf{j} + \omega_2^2 r_2 \sin\beta \mathbf{j} \cdot \mathbf{j} = \omega_2^2 r_2 \sin\beta \quad (16)$$

$$\mathbf{k} \times \mathbf{r}_2 \cdot \mathbf{j} = \mathbf{k} \times (r_2 \cos\beta \mathbf{i} + r_2 \sin\beta \mathbf{j}) \cdot \mathbf{j} = r_2 \cos\beta (\mathbf{k} \times \mathbf{i}) \cdot \mathbf{j} + r_2 \sin\beta (\mathbf{k} \times \mathbf{j}) \cdot \mathbf{j}$$

$$= r_2 \cos\beta \mathbf{j} \cdot \mathbf{j} + r_2 \sin\beta (-\mathbf{i} \cdot \mathbf{j}) = r_2 \cos\beta \quad (17)$$

Substituting Equations 14, 16, and 17 into Equation 12 gives **the angular acceleration of the connecting rod:**

$$\alpha_2 = (1 / r_2 \cos\beta) [\omega_1^2 r_1 \sin\theta - \omega_2^2 r_2 \sin\beta] \quad \text{where, } \alpha_2 = \alpha_2 \mathbf{k} \quad (18)$$

C) Absolute acceleration of the C.G. of the connecting rod:

In order to find the inertia forces at the C.G., we need to find the absolute acceleration of the C.G. This section will deal with the derivation of absolute acceleration of any general point on the connecting rod. Substitution of the center of gravity distance from the crank end center will yield acceleration of the center of gravity.

Absolute acceleration of any point on the connecting rod is given by the following equation:

$$\mathbf{a} = \mathbf{a}_A + \dot{\bar{\omega}}_2 \times \bar{\rho} + \bar{\omega}_2 \times \bar{\omega}_2 \times \rho \quad (19)$$

where, $\dot{\bar{\omega}}_2$ is angular acceleration of the connecting rod, which is equal to α_2 , and ρ is the position vector of any point on the connecting rod (refer to Figure I.1). Evaluating each term in the Equation 19:

$$\mathbf{a}_A = -r_1 \omega_1^2 \cos\theta \mathbf{i} - r_1 \omega_1^2 \sin\theta \mathbf{j} \quad (20)$$

$$\rho = u \cos\beta \mathbf{i} + u \sin\beta \mathbf{j}$$

$$\begin{aligned} \dot{\bar{\omega}}_2 \times \bar{\rho} &= \alpha_2 \mathbf{k} \times [u \cos\beta \mathbf{i} + u \sin\beta \mathbf{j}] = \alpha_2 u \cos\beta (\mathbf{k} \times \mathbf{i}) + \alpha_2 u \sin\beta (\mathbf{k} \times \mathbf{j}) \\ &= \alpha_2 u \cos\beta \mathbf{j} + \alpha_2 u \sin\beta (-\mathbf{i}) = \alpha_2 u \cos\beta \mathbf{j} - \alpha_2 u \sin\beta \mathbf{i} \end{aligned} \quad (21)$$

$$\bar{\omega}_2 \times \bar{\omega}_2 \times \rho = \omega_2 \times \omega_2 \times \rho$$

$$\begin{aligned} \omega_2 \times \rho &= \omega_2 \mathbf{k} \times [u \cos\beta \mathbf{i} + u \sin\beta \mathbf{j}] = \omega_2 u \cos\beta (\mathbf{k} \times \mathbf{i}) + \omega_2 u \sin\beta (\mathbf{k} \times \mathbf{j}) \\ &= \omega_2 u \cos\beta \mathbf{j} - \omega_2 u \sin\beta \mathbf{i} \end{aligned}$$

$$\begin{aligned} \omega_2 \times \omega_2 \times \rho &= \omega_2 \mathbf{k} \times [\omega_2 u \cos\beta \mathbf{j} - \omega_2 u \sin\beta \mathbf{i}] = \omega_2^2 u \cos\beta (\mathbf{k} \times \mathbf{j}) - \omega_2^2 u \sin\beta (\mathbf{k} \times \mathbf{i}) \\ &= \omega_2^2 u \cos\beta (-\mathbf{i}) - \omega_2^2 u \sin\beta (\mathbf{j}) = -\omega_2^2 u \cos\beta \mathbf{i} - \omega_2^2 u \sin\beta \mathbf{j} \end{aligned} \quad (22)$$

Substituting Equations 20, 21, and 22 into Equation 19:

$$\begin{aligned}
\mathbf{a} &= -r_1 \omega_1^2 \cos\theta \mathbf{i} - \omega_2^2 u \cos\beta \mathbf{i} - \alpha_2 u \sin\beta \mathbf{i} - r_1 \omega_1^2 \sin\theta \mathbf{j} - \omega_2^2 u \sin\beta \mathbf{j} + \alpha_2 u \cos\beta \mathbf{j} \\
&= (-r_1 \omega_1^2 \cos\theta - \omega_2^2 u \cos\beta - \alpha_2 u \sin\beta) \mathbf{i} \\
&\quad + (-r_1 \omega_1^2 \sin\theta - \omega_2^2 u \sin\beta + \alpha_2 u \cos\beta) \mathbf{j} \quad (23)
\end{aligned}$$

D) Forces at the connecting rod ends:

Figure 2.2 (b) shows the free body diagram of the piston. By applying dynamic equilibrium conditions to the piston we get:

$$F_X - m_p a_p - \text{Gas Load} = 0$$

The corresponding force in the X direction at the pin end is given by:

$$F_{BX} = -(m_p a_p + \text{Gas Load}) \quad (24)$$

Figure 2.2 (a) shows the free body diagram of the connecting rod. Application of dynamic equilibrium conditions to the connecting rod results in the following equations:

$$F_{AX} + F_{BX} - m_c a_{c.gX} = 0 \text{ (summing forces in the X direction)}$$

$$F_{AY} + F_{BY} - m_c a_{c.gY} = 0 \text{ (summing forces in the Y direction)}$$

Taking moment about point A:

$$F_{BX} r_2 \sin\eta + F_{BY} r_2 \cos\eta + (-m_c a_{c.gX}) u \sin\eta + (-m_c a_{c.gY}) u \cos\eta + (-I_{zz} \alpha_2) = 0$$

Solving the above three equations gives:

$$F_{AX} = m_c a_{c.gX} - F_{BX} \quad (25)$$

$$F_{BY} = [m_c a_{c.gY} u \cos\beta - m_c a_{c.gX} u \sin\beta + I_{zz} \alpha_2 + F_{BX} r_2 \sin\beta] / r_2 \cos\beta \quad (26)$$

$$F_{AY} = m_c a_{c.gY} - F_{BY} \quad (27)$$

From Equation 11 acceleration of the piston is given by:

$$\mathbf{a}_p = \boldsymbol{\omega}_1 \times \boldsymbol{\omega}_1 \times \mathbf{r}_1 + \boldsymbol{\omega}_2 \times \boldsymbol{\omega}_2 \times \mathbf{r}_2 + \boldsymbol{\alpha}_2 \times \mathbf{r}_2 \quad (28)$$

$$\begin{aligned}
\boldsymbol{\alpha}_2 \times \mathbf{r}_2 &= \alpha_2 \mathbf{k} \times (r_2 \cos\beta \mathbf{i} + r_2 \sin\beta \mathbf{j}) = \alpha_2 r_2 \cos\beta (\mathbf{k} \times \mathbf{i}) + \alpha_2 r_2 \sin\beta (\mathbf{k} \times \mathbf{j}) \\
&= \alpha_2 r_2 \cos\beta \mathbf{j} + \alpha_2 r_2 \sin\beta (-\mathbf{i}) = \alpha_2 r_2 \cos\beta \mathbf{j} - \alpha_2 r_2 \sin\beta \mathbf{i} \quad (29)
\end{aligned}$$

$$\text{Equation 13: } \boldsymbol{\omega}_1 \times \boldsymbol{\omega}_1 \times \mathbf{r}_1 = -\omega_1^2 r_1 \cos\theta \mathbf{i} - \omega_1^2 r_1 \sin\theta \mathbf{j}$$

$$\text{Equation 15: } \boldsymbol{\omega}_2 \times \boldsymbol{\omega}_2 \times \mathbf{r}_2 = -\omega_2^2 r_2 \cos\beta \mathbf{i} - \omega_2^2 r_2 \sin\beta \mathbf{j}$$

Substituting Equations 29, 13, and 15 into Equation 28:

$$\begin{aligned} \mathbf{a}_p = & (-\omega_1^2 r_1 \cos\theta - \omega_2^2 r_2 \cos\beta - \alpha_2 r_2 \sin\beta) \mathbf{i} \\ & + (-\omega_1^2 r_1 \sin\theta - \omega_2^2 r_2 \sin\beta + \alpha_2 r_2 \cos\beta) \mathbf{j} \end{aligned} \quad (30)$$

These equations have been used in an EXCEL spreadsheet, referred to in Chapter 2 as DAP (Dynamic Analysis Program), so as to be able to obtain any desired value of angular velocity, angular acceleration, and reaction forces at the crank and the piston pin ends for use in Finite Element Analysis.

APPENDIX II

ReportAppenDyna.xls



**American
Iron and Steel
Institute**



**American Iron and Steel Institute
2000 Town Center, Suite 320
Southfield, Michigan 48075
1-877-STEELINDUSTRY
www.autosteel.org**